Facing the environment: hydrodynamics and confinement modulate molecular motors dynamics

Paolo Malgaretti

Facing the environment: hydrodynamics and confinement modulate molecular motors dynamics

Paolo Malgaretti

Departament de Física Fonamental

Facultat de Física

Universitat de Barcelona

Diagonal 647

08028 Barcelona

Programa de Doctorado en Física

Memoria de tesis presentada en Septiembre 2013 por Paolo Malgaretti
para optar por el titulo de Doctor en Física

Tesis dirigida por
Prof. **Ignacio Pagonabarraga Mora**
Profesor catedratico
Departament de Fisica Fonamental
Universitat de Barcelona

... to Tina, Giampietro e Maura

Contents

CONTENTS

CONTENTS

Contents

CONTENTS

1. Introduction

Life is complicated. In order to survive, living systems need to keep the out of equilibrium condition that allows them to maintain their internal structures and the gradients in concentration, temperature and other intensive quantities necessary to their survival. Therefore, when look from the outside living systems look complicated. Even when looking at monocellular organisms, such as bacteria, several internal structures are involved in many mechano-electro-chemical processes that happen at the same time leading to a quite entangled scenario.

However, "life is complex but not as complicated as we make it[1] ", and a possible route to gain insight into the underlying mechanisms keeping living systems alive is provided by disentangling the overall dynamics into subparts and to look at them separately. For example, one the the most streaking feature performed by living beings is the generation of local mechanical forces. Such an ability allows living beings to perform several tasks such as displacing themselves and to remodel their internal structure by displacing the subunits that compose the cell. The latter process, called intracellular transport, involves the active displacement of molecules, proteins, organelles as well other internal cellular structures. Such an active and directional transport relies on the mechano-chemical energy transduction of molecular motors that actively displace along actin filaments or microtubules involved in the cytoskeleton[2]. The energy supply of such nano-metric motors[3] relies on the hydrolization of ATP that provide $\gtrsim 10k_BT$ of energy for every hydrolyzed ATP.

Even though a single molecular motor can generate mechanical work by itself,

---

[1] Quote from www.soulseeds.com

[2] The cytoskeleton is composed by different filaments in between those actin filaments and microtubules and it contributes in the mechanical properties of the cell, including cell shape

[3] The typical size of the molecular motors active site is of the order of $\sim 10nm$

cellular tasks are generally performed by teams of motors. Thus, much effort has been done to understand the behavior of motors ensembles. Experimental data [32] as well theoretical models [40] have shown that bunches of motors can give rise to dynamical regimes such as clustering [17], bidirectional motion [8] and even jamming [57], [23]. However, up to now few attention has been given to the environment motors move in. Due to motor reduced dimensions, $\simeq nm$, velocity, $\simeq \mu m/sec$ and the high viscosity of the cytoplasm $\simeq 0.1 Pa \cdot sec$ molecular motors move in the low Reynolds regime that allows for the onset of long range interactions between motors provided by the fluid flow they generate by displacing. On the other hand cytoplasm is a quite crowded fluid due to the high concentration of suspended particles. Proteins, molecules, vesicles and organelles are suspended in the cytoplasm and heterogeneities in their concentration locally affects the local properties of the cytoplasm that alter the transport properties of molecular motors as it happens for tracers diffusing in porous media.

1.1 Molecular motors

Due to their ability of generating mechanical forces, molecular motors are quite spread in living systems and they have been found in both animal and plant, Prokaryotic as well Eukariotic cells [46]. Tens of different molecular motors has been identified up to now. In order to distinguish between their main characteristics molecular motors are divided into families according to the filament they move on and to their displacing direction. In fact, molecular motors can actively displace only when they are bound to specific filaments namely, microtubules and actin filaments. While microtubules are characterized by a larger persistence length, $\lambda = 6mm$, and, generally, are involved in the long-range transport, actin filaments are more flexible, $\lambda = 15\mu m$, and are responsible for the local transport [46]. Despite the many differences in their chemical composition microtubules and actin filaments share two properties quite relevant for the dynamics of molecular motors. Both of them are made by smaller building blocks, actin monomers for actin filaments, and tubuline dimers, for microtubules, that provide actin filaments as well microtubules with a periodic structure, see fig 1.1. Moreover, actin monomers as well tubulin dimer have an intrinsic polarity that,
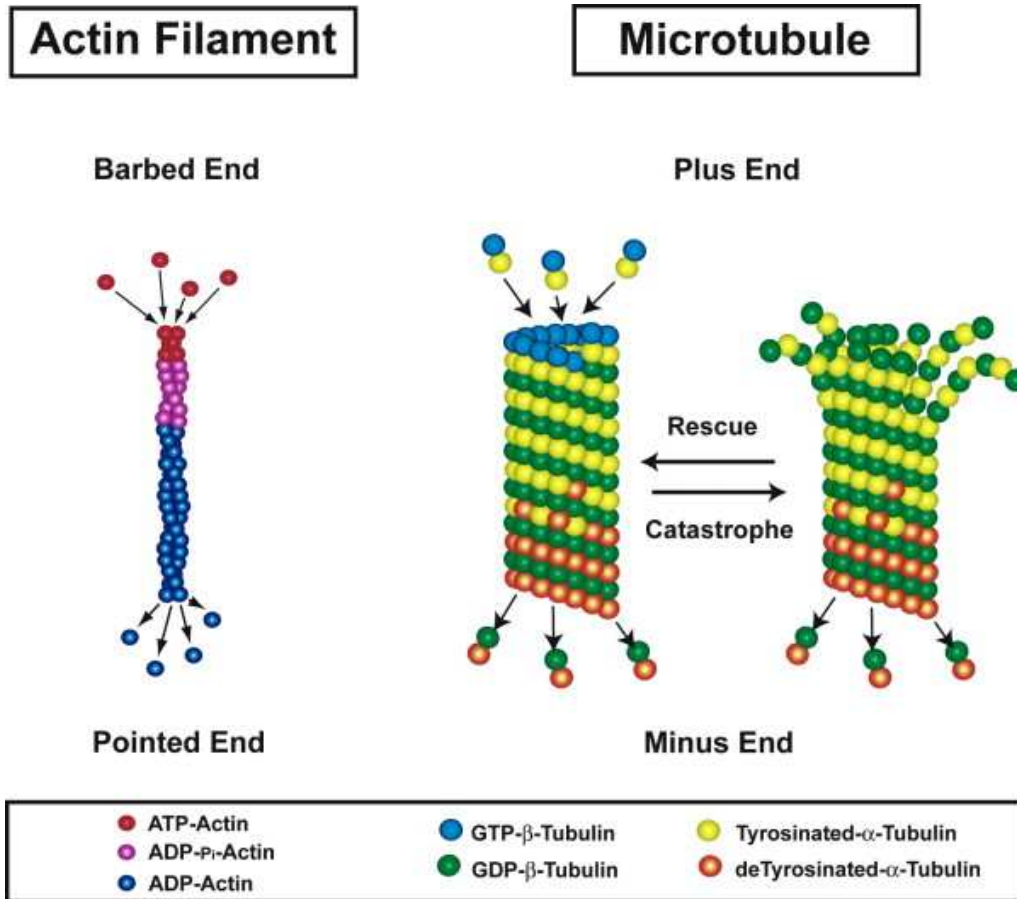
Figure 1.1: actin filaments (left) and microtubules (right) structure and dynamics.

on one hand leads to the onset of an overall polarity of both actin filaments and microtubules, and on the other it guides the binding of molecular motors hence enforcing their motion on a determined direction as compared to the filament intrinsic polarity. Therefore motors are grouped according to the direction the displace along filaments: Kinesins displace towards the microtubule fast-polymerizing (plus) end while Dyneins moves to the slow polymerizing (minus) end. Myosins move preferentially towards the "plus" end of actin filaments [46].

Single motor experiments have shed light on motors trajectories. Optically trapped beds bound to molecular motors have shown a saltatory trajectory where very quick steps, whose length is determined by the spatial periodicity of the filament motor displace on, are performed interspersed between longer pauses, as

1. INTRODUCTION
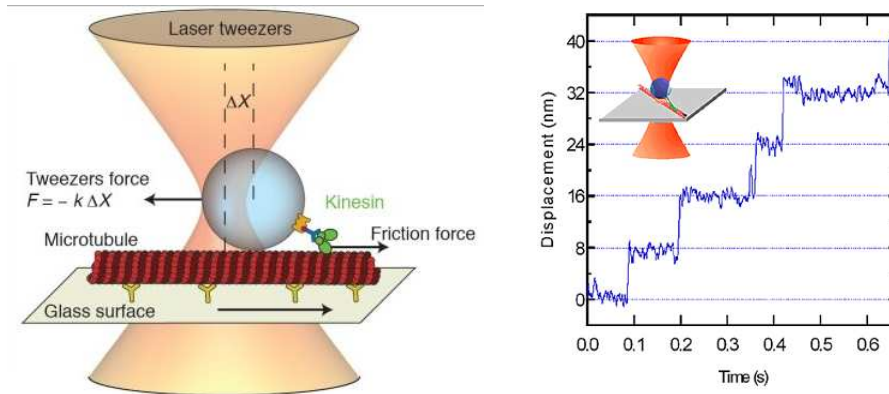
Figure 1.2: schematic view of an optical trapping set up (left) used to track molecular motor. Right: typical trajectory of a molecular motor

shown in fig. 1.2. In particular molecular motors are grouped in two classes according to the number of subsequent steps they can perform subsequently before detaching form the filament: processive motors can perform several steps, $\simeq 10 - 100$, before detaching while non-processive motors can perform just a few steps, ~ 1, before detaching. The processivity of the motors determines which tasks motors are involved in. In general, processive motors are involved in the intracellular transport where smaller teams of motors are responsible for the transport of cargoes over typical distances that can reach the cell size. On the contrary non processive motors are more suited for tasks involving massive number of motors such as muscle contraction. Such distinction of function is not strict and there are several counterexamples such as mitotic spindle where processive motors are massively involved in the onset and displacement of the mitotic spindle [95] or cytoplasmic streaming where nonprocessive motors are responsible for the transport of organelles and vesicles leading to a strong cytoplasmic flux [85].

When molecular motors act in teams the overall dynamics strongly depends on how motors are coupled together. For example, when motors are rigidly bound to a common backbone, the very long range interactions provided by the rigid coupling enhance the overall processivity [58; 82], or to lead to oscillations when an harmonic spring is linking the backbone motors pull on to a static wall [50]. Alternatively, when rigidly coupled motors pull on opposite directions they give

4

rise to an overall bidirectional motion of the cargo [8; 38]. On the other extreme, motor-motor interaction can be very short-ranged as is for steric interactions. Motors pulling on membranes, where only the motors at the tip experience the load provided by the membrane, tend to clusterize at the tip [17] and therefore steric interaction will be relevant in determining the overall dynamics of the motors. Alternatively molecular motors can interact through the fluid flow they generate by displacing. In fact, by moving in the low Reynolds regime molecular motors will experience the fluid flow generated due to displacement of near-by motors. Such an interaction will decay algebraically, $\propto 1/r$, with the distance therefore leading to correlation on longer scale than the steric interaction but shorter than the rigid coupling. Recently the hydrodynamic coupling between motors as been characterized for motors moving according to a lattice gas scheme [44] where a net velocity enhancement has been observed upon increasing the density of motors on the filament.

1.2   Outline

In this thesis we characterize the behavior of molecular motors when the properties of the cytoplasm they displace through are not homogeneous or isotropic. Anisotropies in the cytoplasm can be induced, for example, by net fluxes that can be generated by the displacement of motors themselves [85] as well by other mechanism such as remodeling of the overall cell shape [67]. In the cytoplasm there are many molecules, proteins, vesicles and organelles in suspension. Such a crowded environment develop inhomogeneities in the local properties of the cytoplasm. The different length scales that characterize such inhomogeneities might led to different interplays according to the size of the cargo pulled by motors. For example, suspended particles whose size is much smaller than the cargo size will be experienced by the cargo as an enhancement in the effective viscosity [27; 76]. On the other hand, suspended particles of the same size or bigger than cargoes will develop local structures that affect the space the cargo can explore and will act like a porous medium.

In the first chapter we characterize the hydrodynamic coupling generated by an ensemble of molecular motors displacing along a filament. By numerical

simulations we show how such a coupling develops. The hydrodynamic coupling between motor relies on the fluid flow generated by motors displacement. We discuss how the hydrodynamic coupling between motors depends upon the boundary conditions provided by different geometries.

Motors do not always displace in the same direction, rather cargoes pulled by teams of motors pulling on opposite directions has been observed to undergo a bidirectional motion where the cargo moves back and forth due to the reorganization of the force generated by the motors. In many cases the cargoes motors pull on are vesicles or membrane-embedded organelles. In these cases motors exert force on the cargo by pulling on molecular linkers embedded in the membrane that link the tail of the motors to the membrane. Therefore, the displacement of the linkers in the membrane will lead to a local flow of membrane that can lead to an overall coupling between motors that will sum up to the one generated by the displacement of the motors in the cytoplasm. In the second chapter we develop a coarse grained description of a team of motors pulling on opposite directions that are hydrodynamically coupled. Thanks to our coarse grained model we characterize the overall dynamics of the system and we discuss the peculiar features induced by the hydrodynamic coupling by comparing them against those obtained in the case of rigidly coupled motors.

In the third chapter we characterize the dynamics of a single molecular motor displacing in an inhomogeneous environment modeled as a varying section channel. In the limit in which the channel section is smoothly varying it is possible to reduce the overall dynamics to that of a particle moving in a $1D$ effective potential where the varying confinement enters as an entropic contribution to the overall potential. Using this framework we characterize the dynamics of molecular motors moving according to different schemes. The comparison between the results obtained with the different models allows us to distinguish between general behaviors and model dependent features.

2. Hydrodynamically-coupled molecular motors

2.1 Introduction

When several motors are walking along the same biofilament they will experience their mutual influence. For example, motors ahead and/or motors behind can prevent or enhance forward as well backward stepping hence modulating the overall motor velocity. Several experimental [32] as well theoretical [40] efforts have clarified some of the possible scenarios. For example, it has been shown that increasing the concentration of conventional kinesin motors on microtubules, traffic jams will develop [23; 57]. On the other hand, pairs of conventional kinesin rigidly coupled either via DNA strands, in motility assay[1], or by microtubules, in gliding assay[2], have been observed to increase cargo processivity by reducing the overall unbinding rate of the cargo [58; 82]. In the same experimental setup an increase in the stall force was observed but motors didn't show coordination: no speed up has been observed.

Up to now, much attention has been payed to the case of rigidly coupled motors. However, in many situations motors are weakly coupled. For example, when motors are pulling on vesicles or organelles they are linked to the membrane by binding to membrane-embedded molecules. Therefore, the coupling between

---

[1]Motility assay is an experimental setup where motors are attached to micrometric beads. By an optical trap technique it is possible to track beads trajectory and gain insight into motors dynamics when motors are walking on filaments [46].

[2]Gliding assay is an experimental setup where motors are anchored to a substrate with their heads pointing upwards. Looking at microtubule dynamics on such a carpet of motors it is possible to study motor properties [46].

motors provided by the membrane is not rigid, rather due to the liquid nature of the membrane, it will be a soft-hydrodynamic coupling. Moreover, when motors are moving along filaments they will displace the fluid surrounding them, hence generating local fluxes of cytoplasm that can affect the dynamics of near-by motors. In both situations motor-motor coupling us provided by the fluid they move in.

In order to characterize the role of such interactions, we focus our attention on the characterization of fluid flow generated by molecular motors and the, possible, collective effects provided by the hydrodynamic coupling. The Reynolds number fixes the character of the fluid flow motors will develop and so the coupling provided by the fluid. For smaller Reynolds, $Re \ll 1$, the flow is laminar, hence allowing for the onset of the long-range, $\propto 1/r$, interaction typical of the Stokes regime. For larger Reynolds, $Re \gg 1$, the nonlinear terms dominate, breaking the laminar character of the flow and so the onset of long-range interactions. Due to the small motor size, $\simeq nm$, velocity, $\simeq 1\mu m$ and cytoplasmic high viscosity due to molecular crowding [27], $0.1 Pa \cdot sec$, motors dynamics is characterized by a low Reynolds number, $Re \simeq 10^{-8}$ that allows for long range, $\propto 1/r$, hydrodynamic coupling between motors. In such a scenario, we expect hydrodynamic coupling between motors to be relevant up to distances of the order of several microns[1]. Such a long-range interaction will affect motor-motor interaction as well as the dynamics of suspended particles.

2.2 Physical modeling

In order to characterize the motion of ensembles of molecular motors walking along a common filament we model molecular motors according to the two-state-model [50]. According to this model, motors are regarded as spherical particles,

---

[1]An approximate estimate of the distance up to which the hydrodynamic coupling is relevant can be obtained by studing the case of a couple of identical sphere of radius R kept at distance r when a force f_0 applied on one fo those and the force is measured on the other. When the spheres are far apart, $r \gg R$, the first term (Oseen tensor) of the multipole expansion of the Stokes equation capture the dynamics and the force is given by $f(r) = f_0 R/r$. Comparing the last term with the thermal force acting in a ratchet period $k_B T/L$ we obtain that the two forces equal each other for $r = f_0 L R/k_B T \simeq 2R \cdot 10^3$. For cargoes of the same size as motors, $R = 5nm$ we get $r = 10\mu m$ while larger distances are obtained for larger cargoes.

with radius a, characterized by two internal states. While in the bound state, the motors dynamics is governed by a periodic potential, of period l, mimicking the motor-filament interaction. With rate, $\omega_{1,2}$ motors jump to the weakly bound state where they undergo a free diffusion and with rate $\omega_{2,1}$ motors jump back to the bound state. The dynamics in the weakly bound state determines the processivity of the motor. For processive motors, hence capable to perform several steps before detaching from the filament, the weakly bound state allows for a diffusion "along" the filament, meaning that motors, due to the weak bounding, are not leaving the filament, rather diffusing along its surface. On the contrary, non processive motors lack the weakly bound state and they detach from the filament after each steps they freely diffuse in the cytoplasm. Here, we focus our attention on processive motors and we assume their distance from the center of filament to be independent form the bound/unbound state motors are in. A proper choice of the hopping rates between the two states jointly to a periodic asymmetric potential leads to net currents even for a single motor [50]. The single motor velocity will depend upon many parameters, as shown in fig. 2.1. In our study we fix these parameters to $\delta = 0.2/l$, $\epsilon = 0.1/l$ and the depth of the potential as $\Delta V/k_B T = 200$. For the hopping rates we choose $\omega_{1,2} \to \infty$, i.e. when motors enter in the hopping region, ϵ, they jump with no waiting time and $\omega_{2,1} = \delta^2/D$, being D the diffusion coefficient of the motors. Such a choice of the hooping rate maximizes the single motor velocity [50]. To account for hydrodynamics, the cytoplasmic fluid surrounding filaments and motors is modeled as an ideal dissipative fluid. In this view, the fluid is coarse-grained ad it is modeled by point-like particle that represents "infinitesimal" volumes of the real fluid. Particle-particle interaction is modeled in the following way. When two particles are closer than a cut-off distance r_c then, with probability $P(r)$ they interchange momentum between themselves and with a thermal bath. In particular we use the Lowe-Andersen thermostat 2.1 that conserves linear and angular [1] momentum and, at the same time, ensures a Maxwell-Boltzmann velocity distribution. All these features make the Lowe-Andersen thermostat a good candidate for simulating fluids since, on length scales $l \gg r_c$ we expect to recover the behavior predicted by Navier-Stokes equation. Our tests have shown

[1]momentum is exchanged only along the radial direction
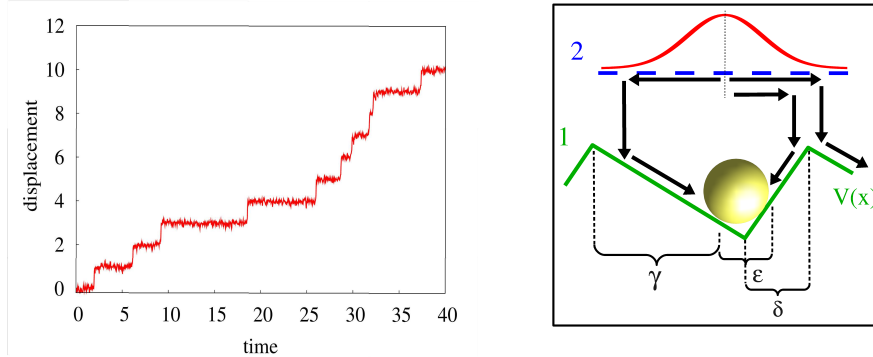
Figure 2.1: Left: typical trajectory generated by a two-state ratchet model [50] for a single molecular motor. Right: free-energy landscape. In the γ region of *state 1* (power stroke phase) motors experience the potential V_1. In region ϵ motors can jump to the *state 2* with a rate p_{12}. In *state 2* (diffusive phase) motors diffuse and can revert to *state 1* with a rate p_{21}. Parameter values used in the simulations: $\gamma = 0.75$, $\varepsilon = 0.01$, $\delta = 0.2$, $\Delta V_1 = 200$ (maximum energy difference) where lengths are in units of the ratchet period l and energy in units of $k_B T$.

that, by forcing the fluid with two opposed volume forces acting on near-by slices of the simulation box, we are able to recover the typical double Poiseuille profile predicted by Navier-Stokes for systems as small as $8\,r_c$. The inetarction rules of the Lowe-andersen thermostat are the following:

$$
\begin{aligned}
\vec{v}'_{i\parallel} &= \frac{1}{2}\left(\vec{v}_{i\parallel} + \vec{v}_{j\parallel}\right) + \vec{\Delta}_{ij\parallel} \\
\vec{v}'_{j\parallel} &= \frac{1}{2}\left(\vec{v}_{i\parallel} + \vec{v}_{j\parallel}\right) - \vec{\Delta}_{ij\parallel} \\
2\vec{\Delta}_{ij\parallel} &= \hat{r}_{ij}(\xi_{ij}\sqrt{2k_B T/m})\vec{r}_{ij} \\
\vec{v}'_{i\perp} &= \vec{v}_{i\perp} \\
\vec{v}'_{j\perp} &= \vec{v}_{j\perp} \\
\langle \xi_{ij} \rangle &= 0 \\
\langle \xi_{ij}^2 \rangle &= 1
\end{aligned}
\tag{2.1}
$$

where $v_{i,j}$ stands for velocity pre-collision, $v'_{i,j}$ for post-collision velocities, m is the the particle mass, k_B the Boltzmann constant, T the absolute temperature and ξ is a white noise.

In order to couple such a coarse-grained fluid to solid rigid objects we have extended eqs. 2.1 in order to take into account fluid-motors interactions. Following the same protocol described for the fluid we have assumed motors and fluid to interchange momentum between themselves when their center-to-center distance is smaller than a cut-off distance, $r_c + a$. Eqs. 2.1 accounts for the thermalization of point-like particles while motors are rigid extended objects with a non vanishing moment of inertia. Then we have ex-

Figure 2.2: Schematic view of the Lowe-Andersen thermostat and of its extension accounting for the interaction between fluid and solid objects in suspension

tended eqs. 2.1 to account for the intrinsic angular momentum carried by the motors, as other rigid objects with different shapes. As for the fluid-fluid interaction linear and angular momenta are locally conserved while the dispersions of the velocities still obey a Maxwell-Boltzmann distribution.

2.3 Characterization of the motor-motor Hydrodynamic interactions

In order to characterize the relevance of motor-motor hydrodynamic coupling we have studied the collective motion of molecular motors that move at a fixed distance r_0 from the surface of a straight, fixed, filament of cross-section πr_0^2. The filament is aligned parallel to one of the edges of our simulation box, of length $L \sim 100\,l$ and square section with edge $L_x = L_y = 24\,l$ and periodic boundary conditions are applied. For simplicity, we assume that motors are infinitely processive (i.e. they never detach from the filament). Starting from a random distribution of motors along the filament, we monitor the average velocity v of the motors, and its dispersion on time scales during which motors can cross the periodic unit box ($t \leq L/v_0$), v_0 being the average velocity of an isolated
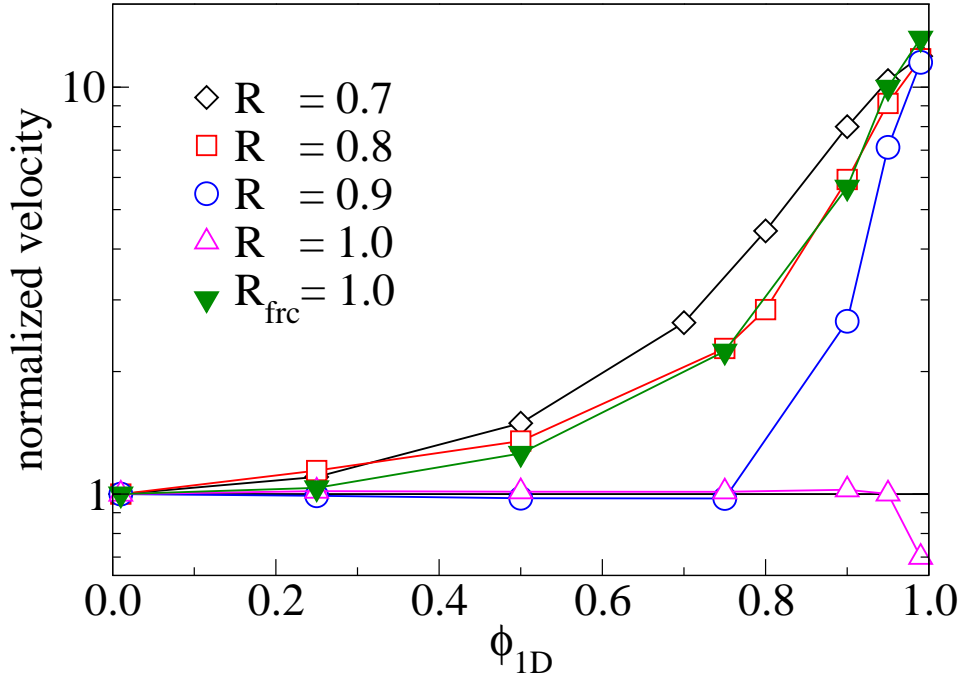
Figure 2.3: Excluded volume interactions. Average velocity of stepping motors as a function of the motor filament coverage, ϕ_{1D} for different ratios $R = a/l$ of the motor radius and ratchet period.

motor. In order to distinguish hydrodynamic (HI) from excluded volume (EV) interactions between motors, we first briefly consider the role of excluded-volume interactions between the motors.

2.3.1 Excluded volume

When motors are interacting only through excluded volume, we can simplify our numerical scheme and solve N coupled Langevin equations each of which describe the dynamics of a single motor. Figure 2.3 shows the variation of v with the filament coverage by molecular motors. The motor velocity is sensitive to the precise value of the ratio R. A monotonic increase of the average velocity with filament coverage ($\phi_{1D} = 2aN/L$) is observed for incommensurate motors,

opposed to what is observed for passive diffusion. This surprising behavior is due to the step-like nature of molecular motors trajectories: when the range of particle-particle repulsion is not commensurate with the ratchet period, a motor in the diffusive state may be pushed toward the ratchet maximum (i.e. to the right into δ in the inset of Fig. 2.1) by a neighbor staying on its left (in region γ). Hence, motors speed up due to the decrease in the time it takes them to move to the next ratchet minimum. When the particle size is commensurate with the ratchet period, $R = 1$, v depends only weakly on filament coverage, except at very high concentrations where many-particle ratchet motion becomes less efficient than isolated motor motion [12; 37]. The relation between the velocity and the occupancy of the filament is typical for continuous models that take into account in more detail nearby motors interactions. On the contrary, for more coarse-grained discrete models, it is well known that the velocity of motors ensemble decreases with filament occupancy [20]. Such a discrepancy underlines the relevance of the microscopic motors dynamic in the development of collective effects.

2.3.2 Hydrodynamic coupling: motors on a $1D$ track

Since we are interested in the effect of HI on collective motor motion, we consider independent, processive motors of size $R = 1$, where EV are unimportant [1]. Fig. 2.4 shows the dependence of v for motors walking along a filament, as a function of the fractional motor coverage of the filament, ϕ_{1D}. For $\bar{\phi}_{1D} \leq 0.1$, the average motor velocity does not depend on concentration but at higher concentrations, we observe a fairly linear dependence of v on ϕ_{1D}. The velocity increase is significantly larger than that observed for hydrodynamically coupled motors that move on a surface under the influence of a *constant* external force that has been chosen such that it reproduces the average velocity of isolated motors (referred to as "sliders" in Fig. 2.4) [44]. The key difference between sliders and ratchet motion is that sliders move smoothly, rather than in bursts.

A simple mean-field argument can be used to estimate the motor density at which hydrodynamic speed-up becomes significant. The average fraction $\rho p_\downarrow$ of

---

[1]An example of such a system is the microtubule-bound KIF1A-kinesin motor [74]
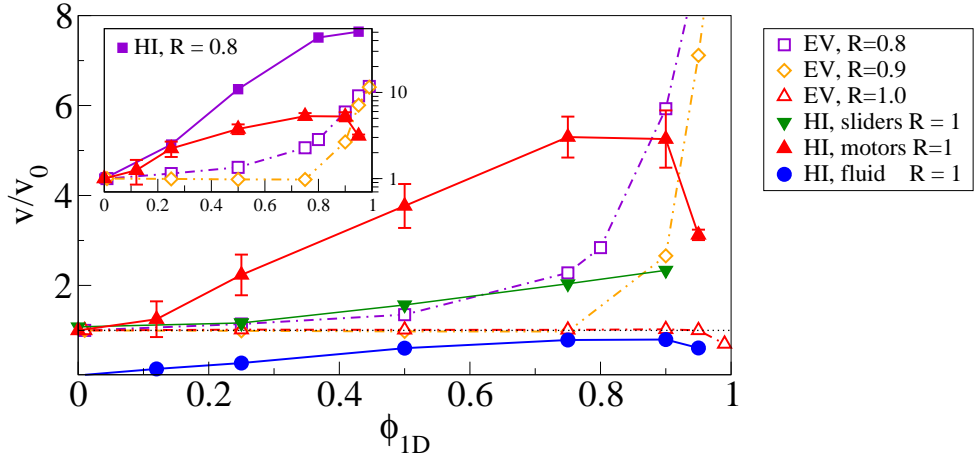
Figure 2.4: Average velocity of stepping motors as a function of the motor filament coverage, ϕ_{1D}. For comparison the corresponding results for "sliders" (see text) are also shown: open and filled down-triangles. Inset: comparison between R=1 (triangles) and R=0.8 (squares) motors including HI.

bound motors which move under the influence of the ratchet force, f, (bound state) induces a mean drift velocity $v \simeq 2\frac{f}{6\pi\eta a}\rho p_{\downarrow}\frac{l-\delta}{l}\int_{2R}^{L/2} dr \frac{3a}{2r}$ on the diffusing motors (weakly bound state) over the characteristic time $\Delta t \simeq \frac{l-\delta}{2}\frac{6\pi\eta a}{f}$ in which bound motor displace along the filament. Hydrodynamic correlated motion plays a role when the mean displacement felt by the diffusing motors due to the forced ones allows them to surmount the characteristic ratchet barrier, i.e. $v\Delta t \geq \delta$. Hence, hydrodynamic speedup becomes significant for $\phi_{1D} \geq \bar{\phi}_{1D} \equiv 2\delta/(l - d)^2 \ln L/4a$, which corresponds to $\bar{\phi}_{1D} \simeq 0.1$ for $\delta = 0.2, R = 1, \tilde{L} = 100$ and $p_{\downarrow} \sim 1$.

When ϕ_{1D} approaches one, EV lead to a substantial decrease of the mean motor velocity. Fig. 2.4 also shows that collective motor motion induces a net average flow of the fluid in which the microtubule and motors are embedded. Hence, active motor motion favors also the transport of suspended, passive particles. This transport scenario is likely to be relevant for cargo motion in elongated
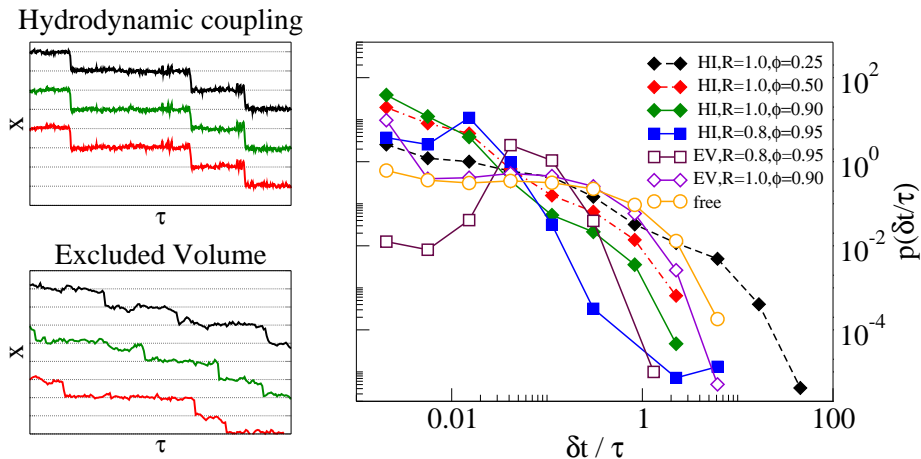
Figure 2.5: Left: Correlated (uncorrelated) motion of adjacent stepping motors with HI (EV). Right: probability distribution of the dwell time, δt, between consecutive stepping of neighbor motors.

geometries such as neurons and in plant cells. If the motor size is not commensurate with the ratchet period, $R < 1$, the average motor velocity is further enhanced, as shown in the inset of Fig. 2.4.

The distribution of dwell times (δt) between subsequent stepping events of nearby motors provides insight into the mechanism of hydrodynamic velocity enhancement. Fig. 2.5 shows the probability distribution function (pdf) of dwell times with and without HI. The curve corresponding to the absence of HI and EV provides the reference behavior for non interacting motors. Next, we consider the case with EV. Commensurate motors, $R = 1$, can arrange in registry with the ratchet period and the distribution of dwell times does not differ significantly from that of non-interacting motors in the ϕ_{1D}-range studied. For smaller R, the short-ranged interactions between motors hinder their relative displacements, which favors shorter dwell times. The situation is qualitatively different when hydrodynamic coupling is taken into account. Fig. 2.5 shows an enhancement of the pdf for small δt, indicating that HI favors the correlated motion of subsequent motors. When a motor steps, it generates a transient flow that pushes (pulls) the motors that are in front (behind) it, thus facilitating their crossing of the ratchet barrier, provided that they diffuse within a distance δ from top of the potential barrier. A similar speedup has been described for colloids moving in a saw-tooth

potential, under the influence of a constant, external force [61]. The properties of the pdf in the presence of HI are robust to changes in filament coverage and motor radius; the pdf always exhibits a maximum at small δt indicating that generically hydrodynamics favors barrier crossing in the neighborhood of a stepping motor. The left panels of Fig. 2.5 display typical trajectories of three nearby motors. In the presence of HI (top), jumps are strongly correlated, while no correlated jumps are observed in the absence of HI (bottom).

2.3.3 Hydrodynamic coupling: motors on a $2D$ filament surface

Motors are not necessarily restricted to move along a single 1D-like track. Microtubules indeed are composed by a number of polarized tracks arranged in a cylindrical filament. To mimic the latter scenario we allowed motors to displace freely on the filament surface while subject to the same filament interaction, $V(x)$. An even stronger increase in v is observed now as a function of the surface motor coverage, $\phi_{2D} = Na^2/(2rL)$, as shown in Fig. 2.6. The more homogeneous filament coverage with respect to single track motion leads to average motor velocities that are one order of magnitude larger and it results in a stronger coupling to the surrounding fluid; the average flow velocity is comparable to that of the motors. This implies that collective active motion of molecular motors can also induce efficient passive intracellular transport. As in the purely 1D case, there is a characteristic threshold coverage, $\bar{\phi}_{2D}$, above which hydrodynamic speed up of v is observed.

The fact that the mean motor velocity depends on the motor concentration leads to "bunching". A group of motors with a higher than average concentration will move faster than the rest, thus leading to the build up of larger clusters. This clustering results in heterogeneous filament coverage. We have analyzed cluster formation of motor aggregates on long time scales, $t \gg L/v_0$. Using a robust distance criterion to identify clusters [1], we find that at intermediate and high filament coverage motors aggregate into a single cluster that survives for the rest

---

[1]Two motors belong to the same cluster if their distance along the filament is smaller that $3R$.
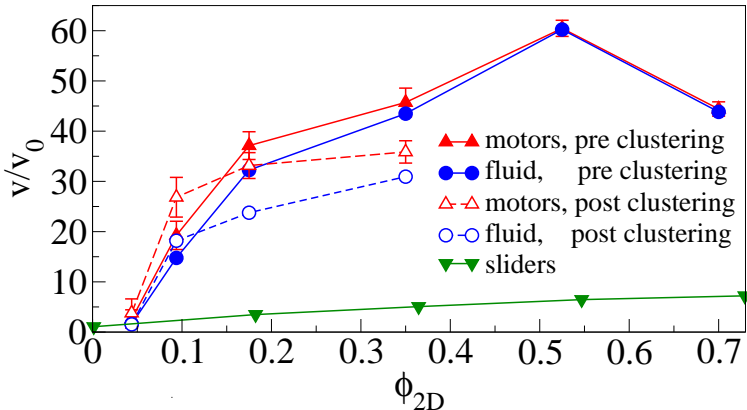
Figure 2.6: HI-induced clustering of motors moving on a filament surface. Filled symbols show the average velocity of motors (triangles) and fluid (circles) before clustering. The corresponding open symbols show the velocity after clustering. "Sliders" (downward triangles) clustering does not affect the mean velocity.

of the simulation up to twice the time needed to form the aggregate (see panel A of Fig. 2.7). At longer times, the average motor speed and the coupling with the embedding fluid decrease slightly, as shown in Fig. 2.6, underlining that the heterogeneous coverage of the filament jointly with an increased effective volume fraction caused by clustering affect the collective motion of motors. As the mean filament coverage increases, the aggregate percolates along the filament. At low filament coverages, $\phi_{2D} < 0.15$, we do not observe large aggregates. Rather, motors organize into small clusters that form and dissolve. However, we cannot rule out that clusters develop at longer times.

The hydrodynamic speed up of groups of motors increases transport efficiency. To estimate this increase, we assume that the transition rate between the two internal states of a motor is independent of filament coverage. It then follows that the energy consumption of non-interacting motors is independent of coverage. A good measure of motor efficiency is then the average number of cycles, N_J, between the two internal energy states of the motor that are required to make a motor move one period in the saw-tooth potential. Panel B of Fig. 2.7 shows that N_J decreases sharply when the motors speed up due to HI. For EV the decrease in N_J is much more gradual and it is essentially absent if the size of the motor is commensurate with the sawtooth period. The sharp decrease of N_J with coverage

17
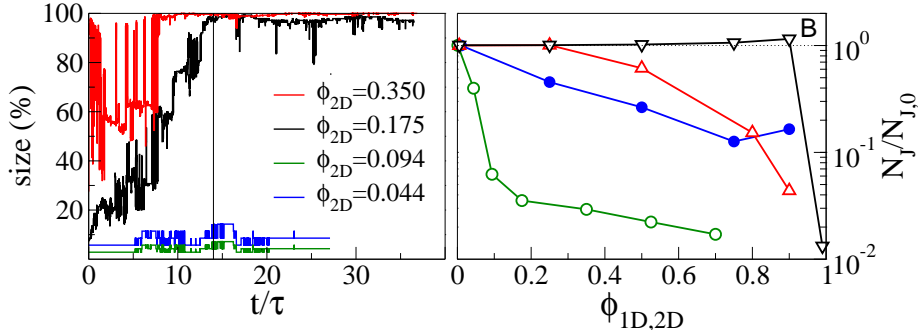
Figure 2.7: Left: fraction of motors belonging to the largest cluster, as a function of time. The time unit $\tau \equiv L/v_0$. Right: Average number of motor power strokes to displace one ratchet period. The energy consumption is proportional to the number of power strokes. Up (Down) triangles stands for motors interacting through EV and R=0.8 (R=1) while filled (open) circles stand for motors interacting through HI for the 1D (2D) case.

shown in Fig. 2.7 illustrates that, as a result of hydrodynamic coupling, many motors "surf along" on the flow field generated by the power stroke of a single motor.

2.3.4 Radial confinement

The hydrodynamic coupling between motors leads to the onset of very strong fluid flows, as shown in fig. 2.6, that will be strongly affected by boundary conditions. The results shown so far are obtained for periodic boundary conditions, i.e. for a crystal of filaments aligned with the same polarity. However, in biological situations such as pollen tubes, cytoplasmic strands and neuronal axons, this is not the case, rather the system has a cylindrical symmetry where the filament motors walk on is in the middle of a pipe-like membrane. The presence of such a radial confinement will strongly affect both motor-motor dynamics as well the onset of the fluid flux. The vanishing condition on the confining surface forces the fluid velocity field to adjust. Then, since the motor-motor hydrodynamic coupling relies on the fluid flow, motors collective dynamics might be affected as well. Moreover, the confinement introduces a new typical length scale, possibly screening the hydrodynamic coupling on larger distances. Fig. 2.8.A shows the
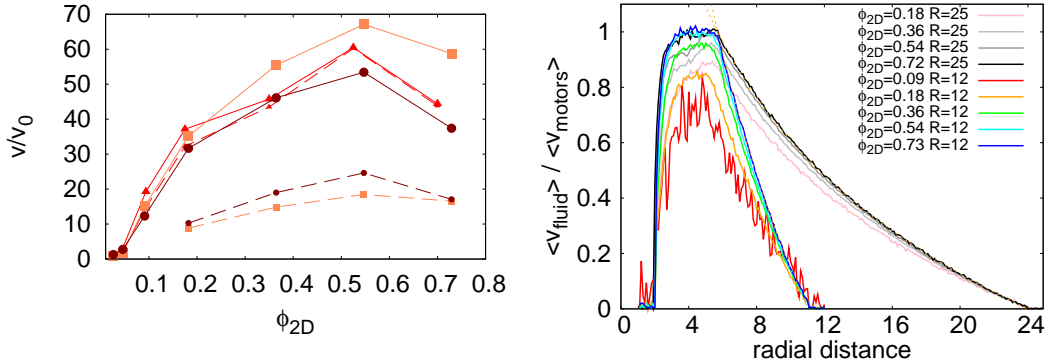
Figure 2.8: Left: Collective motion of molecular motors ensemble (solid lines) and average fluid flow (dashed lines) in radial confined environments characterized by radii $R = 12, 24$ in units of the ratchet period l for (pink) squares and (brown) dots respectively. The case of periodic boundary conditions (red triangles) has been shown as a reference. Right: fluid velocity profile for the two case of confinement and different volume fractions as indicated in the legend.

average motor velocity and the corresponding fluid flow for two different sizes of the radial confinement, as compared to the case of periodic boundary conditions. Interestingly we notice that the radial confinement is not affecting much the overall dynamics and motor speed is quite insensitive to radial confinement. On the contrary the fluid flow is quite reduced, as we expected, due to the no-slip condition imposed on the outer boundary. It is remarkable to notice that, even though the fluid flux is quite reduced on average, in the vicinity of the motors the fluid net flow is still comparable to motor velocity, as shown in fig. 2.8.B. The persistence of such a strong local flux even for more restrictive confinement is responsible for the weak dependence of motors net velocity upon variation of the outer boundary. Finally we remark that the fluid velocity profile shown in fig. 2.8.B adjusts very well to the logarithmic behavior predicted by the Navier-Stokes equation (dashed lines in fig. 2.8.B) typical of a Couette-like flow.

2.4 Convection of suspended particles

Several molecules, proteins, vesicles and organelles are suspended in the cytoplasm. Therefore, the cytoplasmic streaming generated by the collective dis-

placement of molecular motors will affect the transport properties of suspended particles. On the other hand, the presence of suspended particles might change the local effective transport properties of the cytoplasm hence affecting motors displacement, and so the onset of the hydrodynamically driven speed up observed in the previous sections. In order to characterize the effect of suspended particles on the collective motion of hydrodynamically coupled molecular motors we have studied the dependence of motor velocity on the concentration of suspended particles in the case of motors walking along a common filament. Suspended particles are constrained by a radial confinement similar to that studied in the previous section. In this way the free space suspended particles can access is a cylindrical shell whose external radius is $R - a$, being R the radius if the radial confinement and a the radius of suspended particles, and an inner radius, $r + 2a$, characterized by the presence of the inner filament, with radius r, and of the walking motors. As we have discussed in the previous section, the radial confinement acts also as a sink of momentum since, on its boundaries, no-slip condition for fluid velocity apply. We study the motion of motors varying the volume fraction of suspended particles, ϕ_{3D} defined as, $\phi_{3D} = \frac{4a^3 N}{3[(R-a)^2 - (r+2a)^2]L}$ where N is the number of suspended particles, L the length of the simulation box and $\pi[(R-a)^2 - (r+2a)^2]L$ is the free amount of space the center of mass of suspended particles can explore. The dependence of motor velocity upon variation in the suspended particles volume fraction, ϕ_{3D}, as well in motors occupancy, ϕ_{2D}, is shown in fig. 2.9. For smaller values of ϕ_{3D} the overall velocity of walking motors is not much affected by the presence of suspended particles. Interestingly we find that, for intermediate values of ϕ_{2D}, the presence of suspended particles enhances the velocity of walking motors as compared to the case in the absence of suspended particles. This is due to the fact that suspended particles enhances the onset of large clusters that, for $\phi_{2D} \simeq 0.1$, lead to an overall speed up. We do not exclude the formation of those clusters on longer times scales, even in the absence of suspended particles, however such a characterization has not been possible yet due to our reduced computational resources. For increasing values of ϕ_{3D} the overall effect of the presence of suspended particles is to reduce motor velocity. We can gain insight into such a dependence by analyzing the fluid flow. Increasing the density of suspended particles the fluid flow is quite affected, as shown in fig. 2.9,
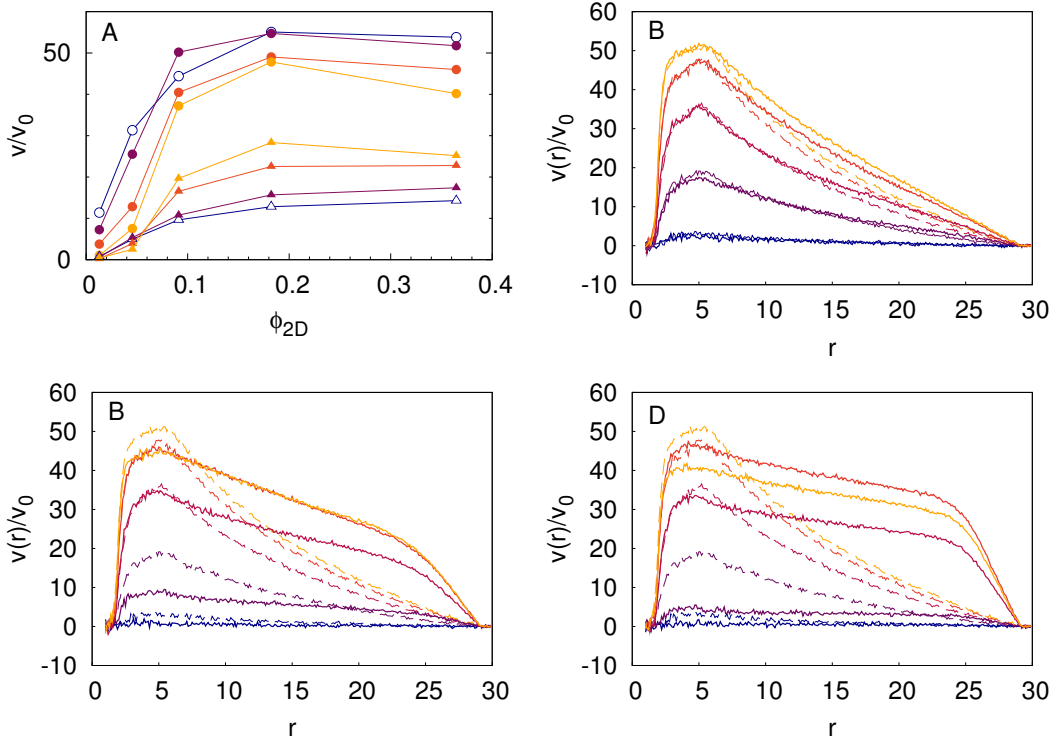
Figure 2.9: Suspended particles. A: Average velocity, normalized by the single motor velocity v_0, of fluid particles (triangles) and of motors (circles) walking on the inner filament as a function of motors occupancy for different densities of suspended particles: $\phi_{3D} = 0.017, 0.051, 0.085$ (color code: lighter colors stands for larger values of ϕ_{3D}). The velocity of motors walking in the absence of suspended particles as been drawn as a reference (open points). B,C,D: average longitudinal fluid velocity (solid lines) as a function of the radial distance for different walking motor occupancies (color scheme: lighter colors stand for larger values of ϕ_{2D}) and for different values of suspended particles volume fraction, $\phi_{3D} = 0.017, 0.051, 0.085$ respectively for panel B,C and D. The fluid velocity profile, in the absence of suspended particles, for the same walking motors occupancies as been reported as a reference (dashed lines).
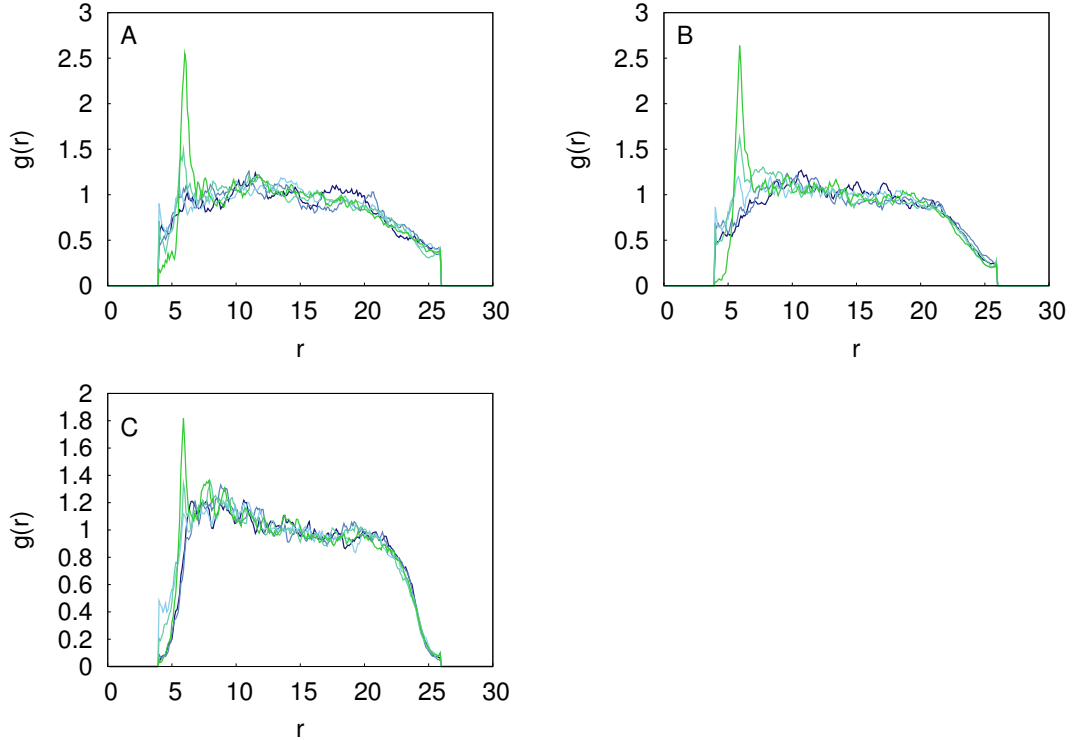
Figure 2.10: Radial distribution of suspended particles for different values of ϕ_{2D} (color scheme: lighter colors stands for larger values of ϕ_{2D}) and for $\phi_{3D} = 0.017, 0.051, 0.085$ respectively for panel A,B and C.

leading to an enhanced fluid velocity and larger gradients of fluid velocity close to the external surface. Interestingly, the presence of suspended particles promotes larger values of fluid flow, Q, as compared to the case of $\phi_{3D} = 0$, as shown in fig. 2.9.A. The increase in Q does not lead to an increase of motorvelocity with ϕ_{3D}, rather motor velocity is hampered with increasing ϕ_{3D}. We gain insight in this behavior by looking at the radial distribution of suspend particles. As shown in fig. 2.10 the density of suspended particles around the walking motors increases while increasing the value of ϕ_{3D}. Such an accumulation of suspended particles in the near of walking motors can affect their motion either by increasing the local effective viscosity either due to excluded volume interactions. For larger values of ϕ_{3D}, for which the velocity reduction is more prominent also a reduction in the peak of the radial distribution function appears, compare panels B,C and D of fig. 2.9, remarking the strong interplay between the radial distribution of
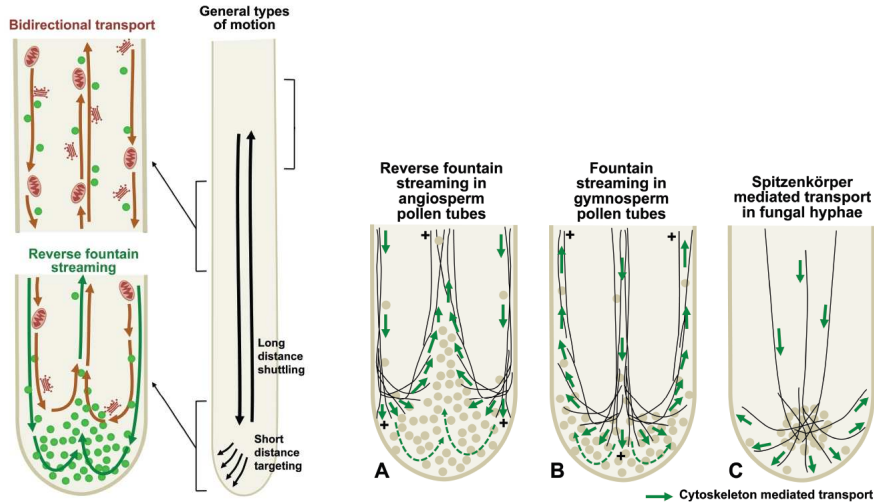
Figure 2.11: Different topologies of filament involved in the cytoplasmic streaming. (Image from reference [19])

suspended particles and walking motors dynamics.

2.5 Cytoplasmic streaming in confined geometries

In the previous section we have characterized the interplay between the dynamics of molecular motors and the presence of suspended particles when molecular motors are walking along a common filament. Here we extend our previous analysis to the case in which molecular motors are walking on opposite directions. In particular we focus on the case in which motors moving in opposite direction are confined to different filaments, namely on the inner filament, as in the previous case, and on the inner surface of the radial confinement. This configuration is quite common in plant cells like pollen tubes [19]. Fig. 2.11 shows the typical bidirectional cytoplasmic flow responsible for pollen tube growth [29; 92; 98].

As a preliminary study we have characterized the dynamics of two teams of motors: one is walking on the inner filament and the other on the outer surface. The two teams of motors displace on opposite directions. Fig. 2.12 shows the average velocity of motors walking on the inner filament ans well motors walk-

23
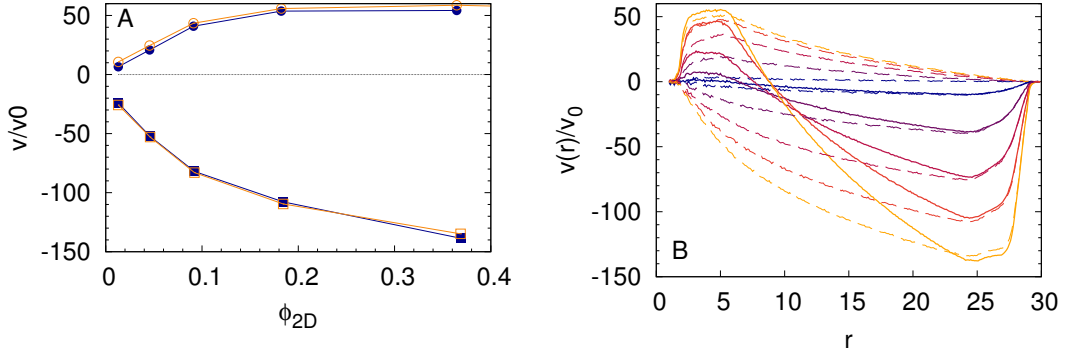
Figure 2.12: A: average velocity of motors ensembles walking on the inner filament (circles) and on inner surface of the radial confinement (squares) as a function of the occupancy, normalized by single motor velocity. The velocity of motors walking solely either on the inner or on the outer filaments are shown as a reference (open points). B: fluid velocity profile for the same values of the parameters as in panel A, where lighter curves stands for larger values of the walking motors occupancy ϕ_{2D}. The fluid velocity profile for motors walking exclusively on one of the two filaments with the same ϕ_{2D} of the cases in panel A, are reported (dashed) lines for comparison.

ing on the inner surface of the radial confinement as a function of the common coverage, ϕ_{2D}. Fig. 2.12 shows that the presence of counter-propagating motors is not affecting much the onset of the collective behavior. If we look at the fluid velocity profile we notice that large gradients develop close to the motors walking on the inner filament due to the presence of the opposite flux generated by motors walking on the inner surface of the radial confinement. Surprisingly, we notice that for intermediate values of ϕ_{2D}, namely $\phi_{2D} = 0.1$, the velocity of motors on the inner filament is significantly reduced. On the contrary, for $\phi_{2D} < 0.1$ and $\phi_{2D} > 0.1$ the velocity of motors on the inner filament is comparable to the case of the absence of counter propagating motors.

When we add suspended particles the behavior of the system is strongly affected. Fig. 2.13.A shows that the velocity of motors walking on the inner surface of the radial confinement are not much affected by the presence of suspended particles and displace at velocities comparable to those obtained for $\phi_{3D} = 0$. On the constrary, the dynamics of motors walking on the inner filament is more involved. As in the previous section, see fig. 2.9.A, for smaller values of ϕ_{3D} the
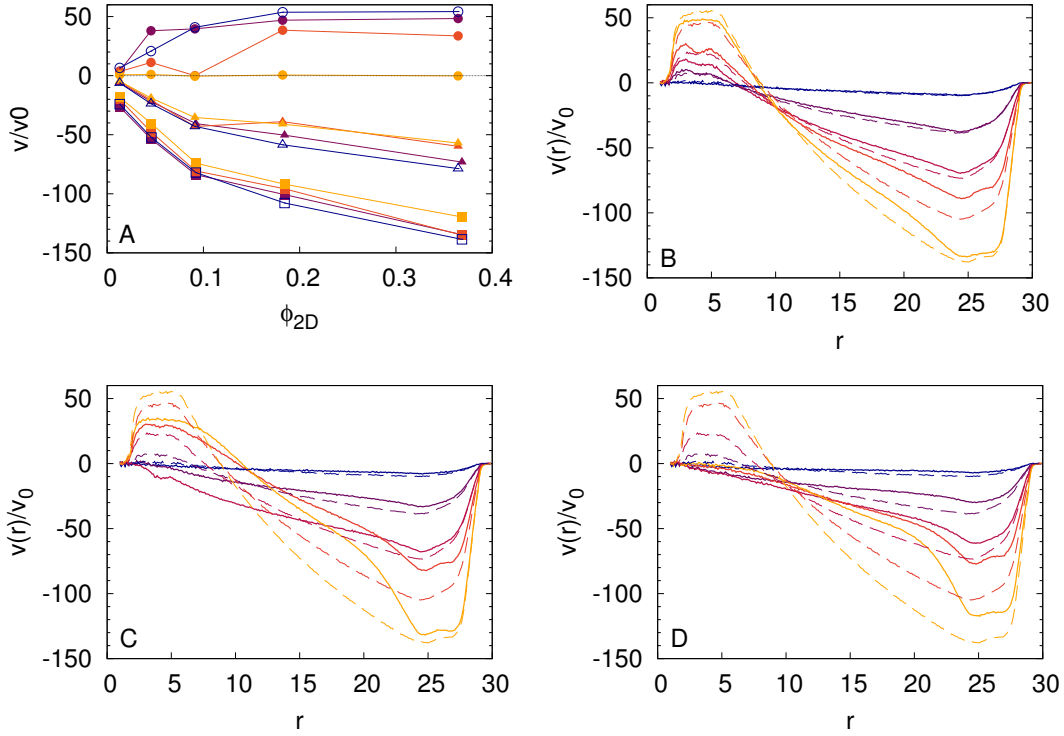
Figure 2.13: Suspended particles convected by a fountain flow. A: average velocity of motors ensembles walking on the inner filament (circles) and on inner surface of the radial confinement (squares) and average fluid velocity (triangles) as a function of ϕ_{2D}, normalized by the single motor velocity, for different density of suspended particles: $\phi_{3D} = 0.025, 0.05, 0.075$ where lighter colors stand for higher suspended particles densities. The velocities in the case of absence of suspended particles are reported (open points) for comparison. B,C,D: average longitudinal fluid velocity (solid lines) as a function of the radial distance for different walking motor occupancies (color scheme: lighter colors stand for larger values of ϕ_{2D}) and for three different values of suspended particles volume fraction, $\phi_{3D} = 0.025, 0.05, 0.075$ respectively for panel B,C and D.
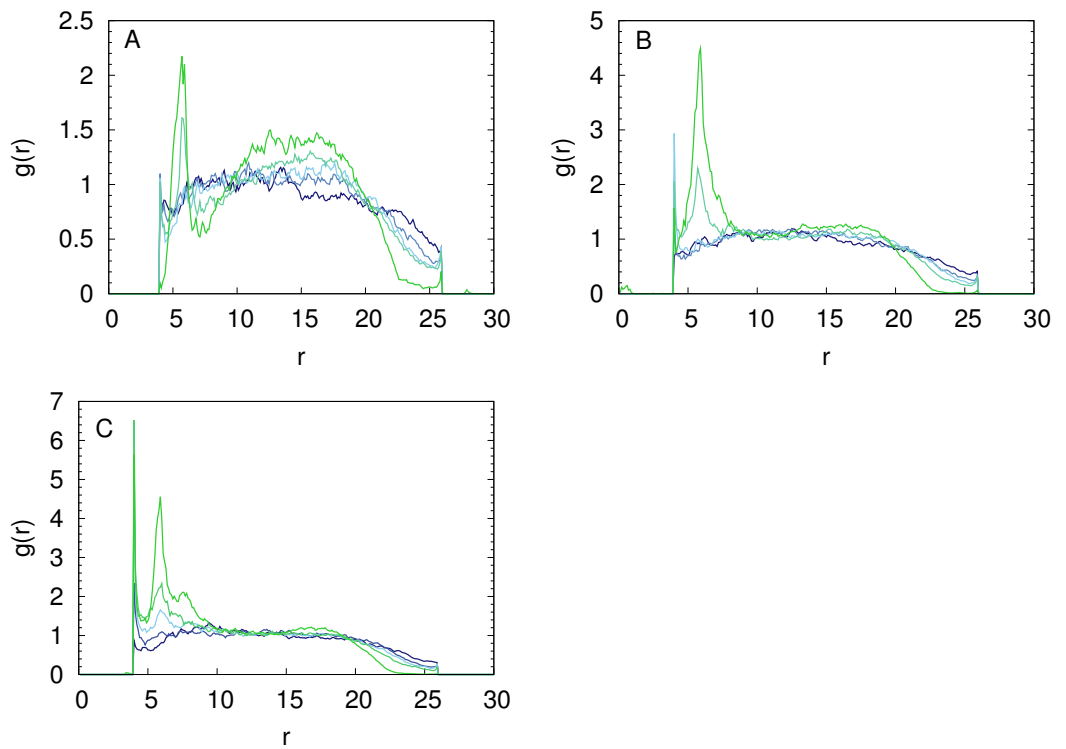
Figure 2.14: Radial distribution function of suspended particles upon variation of the pulling motors occupancy, phi_{2D}, (color code: lighter color stand for higher occupancy) and for different suspended particle density: $\phi_{3D} = 0.025, 0.05, 0.075$ for panel A,B and C respectively.

velocity of motors walking on the inner filament is not much affected by suspended particles, rather it can be enhanced for intermediate values of ϕ_{2D} due to the enhancement of the formation of larger clusters. When increasing the value of ϕ_{3D} the dependence of the velocity of motors on the inner filament on ϕ_{2D} becomes more involved and for $\phi_{2D} = 0.1$ inner motors stops while for larger values of ϕ_{2D} their velocity is non-vanishing again. Interestingly when the motors on the central filament stop we observe a sharp peak in the concentration of suspended particles around the inner filament, as shown in fig. 2.14.B, hence enforcing the correlation between the onset of large accumulation of suspended particles in the near of the inner filament and the reduction of the velocity of motors walking on the inner filament. For larger values of ϕ_{2D} the peak develops a bit further away from the inner filament. When increasing the values of ϕ_{3D}, i.e. $\phi_{3D} \simeq 0.1$ the large accumulation around the central filament prevent the displacement of motors walking on the inner filament irrespectively from the value of ϕ_{2D}. As we discussed in the previous section, the presence of suspended particles affects the fluid velocity profile. While in the previous case we have observed an enhancement of the fluid flow, Q, for the present case we find that the overall fluid flow is reduced by the presence of suspended particles. In particular, for ϕ_{3D}, where the motion on the inner filament is hindered, the fluid profile is still quite affected by suspended particles and the overall fluid flow quite reduced.

2.6 Conclusions

We have shown the the coupling between the motors and the fluid they move through leads to novel dynamical regimes.

The coupling between the step-like motion of the motors with the surrounding fluid leads to a positive feedback that enhances motors ensemble velocity up to two orders of magnitude as compared to the single motor velocity. Interestingly such a large speed-up is absent for particles under a constant force, underlining the relevance of motors stepping trajectory in the onset of collective effects. The steric interactions between motors leads to velocity enhancements, comparable to those obtained by hydrodynamic coupling, when the motors size and the ratchet potential are not in registry. However, the underlying physical mechanism leads

to different dynamical regimes. We have characterized the signature of the hydro-dynamic coupling, as compared to the case of steric interactions, by looking at the distribution of the dwell time between the overcome of the barrier of two nearby motors. The dwell time between near-by motors barrier overcome is, on average, much shorter, for hydrodynamically coupled motors than that for motors under solely steric interactions. Such a difference relies on fact that hydrodynamically coupled motors can both attract and repel each other while for steric interaction provides only repulsion. Therefore, in the case of hydrodynamic coupling the front motor can enhance the barrier crossing of the rear motor, while this feature is absent for the case of solely steric interactions. Finally we have shown that the steric interactions and hydrodynamic coupling can couple positively leading to even larger velocity speeds-up.

The geometry of motors distribution play a relevant role. Comparing the data of the $1D$ case with the $2D$ case we notice that the more uniform coverage of the filament, as is for the $2D$ case, leads to a quite larger velocity enhancement as compared to the $1D$ case where motors are confined along a single lane. Moreover, for motors dispersed on the $2D$ surface of the filament we observe clustering at intermediate volume fractions. The structures we observe are quite robust and they are stable when in contact with a more diluted phase. The onset of large clusters provides a less uniform distribution of motors along the filament. Accordingly, we observe a reduction in the overall motor velocity once clustered as compared to the velocity of the uniform density phase, in agreement with our previous observation on the relation between filament coverage and motors ensemble velocity.

Cells are not unbound systems and the presence of the no-slip condition for fluid velocity on cell membrane might affect the overall dynamics. Our results show that the hydrodynamic coupling between motors is quite robust. Even for quite severe radial confinement characterized by an aspect ratio $d = L/R \simeq 10$, being L the length of the filament and R the radius of the outer confinement, the average speed of motors keeps quite similar to that of weaker confinement, $d = 5$, or periodic boundary conditions.

The displacement of several motors along the same filament will develop local cytoplasmic fluxes that will affect the dynamics of suspended particle. Therefore,

the flux generated by displacing motors provides an alternative means for active transport. Due to convection, not only vesicles or organelles can be actively transported, but also suspended molecule and proteins without the need to collect them into membrane embedded cargoes. Surprisingly, we have observed that the presence of suspended particles affects significantly the overall dynamics. By increasing the overall dissipation, suspended particles enhance the effective viscosity experienced by motors. Hence motors walking on opposite directions, even though quite far apart, will experience an enhanced interaction that can lead to different regimes according to the concentration of motors on both filaments. Since the relation between the overall velocity and motors occupancy is highly non linear then it is not possible to identify the ratio between the occupancies on the two filaments as a dimensionless number governing the overall dynamics. Rather, the steady state will be determined by both values and increasing or reducing both of them at the same time will change the dynamical regime of the system. feedback loop.

The relevance of convection will decrease with the distance from the filament motors are displacing on. Therefore, convection will be particularly relevant for those particles undergoing a $1D$ diffusion along filaments. In fact it has been experimentally observed that microtubule-ends depolymerizing motors MKAC [42], Myosin V [97] and synthetic charged beads [68] as well as many other microtubule binding proteins [24] undergo $1D$ diffusion along microtubules when they are weakly bound to the filament. Hence, the distribution of such particles along the microtubule as well their transport properties will be strongly affected by flux generated by bound motors. In particular the onset of a net flux brakes the left right symmetry along the filament possibly leading to the formation of density gradients.

The motor-motor interaction provided by hydrodynamic coupling relies on the convection of weakly-bound motors by means of the flux generated by pulling motors in bound state. Therefore the relevance of the motor-motor hydrodynamic coupling relies on the time motors spend in the weakly bound state. Such a quantity is captured by the duty ratio [45], i.e. the ratio between the time motors spend in the bound state over the time of a full cycle. We expect motors characterized by higher duty ratios to experience a weaker velocity speed up while

motors with smaller duty ratio to take more advantage by the collective motion. Interestingly, it has been shown that the value of the duty ratio reflects, for the majority of the cases, motor processivity [11; 46]. Processive motors, hence capable to perform many steps before detaching, have a large duty ratio, $\simeq 1/2$, while non processive motors have a very small duty ratio, $\simeq 0.01$ [11; 46]. Therefore, non processive motors such as Myosin XI in Chara algae, are more suited to exploit the flux generated by other motors. In this view, it is not surprising that the fastest cytoplasmic streaming, $\simeq 100\mu m$, observed in Chara algae [35] is generated by non-processive motors.

Non-processive motors are not the only motors that can experience velocity speed-up while collectively displacing. Recently some processive motors,such as KIF1A [74], single-headed Myosin VI [47], microtubule cross-shifting motor Eg5 [52; 95], Kinesin-8 [49], kinesin-1 [60] and cytoplasmic Dynein [5; 88; 94] have been found to switch from $1D$ diffusion along the filament and stepping[1]. These motors are characterized by three states, namely bound to the filament, unbound and weakly bound. When motors are in the weakly bound state, they undergo $1D$ diffusion along the filament. In particular KIF1A has been observed to clusterize [36] and clusters of KIF1A has been observed to undergo net displacements only when the density of KIF1A bound to the cargo has overcome a threshold[53]. Such a feature somehow reminds the behavior shown in figs.2.4,2.6 where the collective effect arise for densities larger than a non vanishing threshold.

---

[1]For a more comprehensive yet not exhaustive review see ref. [24]

3. Bidirectional cargo transport

3.1 Introduction

In this chapter we characterize the bistable motion of cargoes pulled by teams of motors pulling in opposite directions. It has been observed in several experiments that cargoes move back and forth under the action of teams of motors moving on opposite directions [32; 40; 56]. The underlying mechanisms are still unclear, and two different scenarios have been proposed. The chemical mechanism assumes a chemical that regulates the direction of the moving motors [31; 55; 56]. According to the mechanical mechanism, motors act as if they were in a tug of war game [2; 54; 69]. In this scenario the direction of motion is determined by the strongest team. While the first scenario requires a fine chemical tuning of the activity of such regulator, the second scenario relies on the fluctuation in teams population as well motor activity typical for small system and relatively small motor teams, as is for biologically relevant situations. A recent work [38] has investigated the role of the intrinsic motors stepping dynamics in the onset of bistable cargo transport. In particular, it has been shown that a collection of molecular motors pulling on opposite direction can lead to spontaneous symmetry breaking when they are rigidly coupled [38]. However, when motors are pulling on membrane embedded cargoes they are not rigidly coupled. Rather they do interact through both the fluid-like membrane their tails are embedded in and the cytoplasm motors move through. The different coupling mechanism, depending on the nature of the cargo motors are pulling on, can strongly affect the overall dynamics. As we have seen in the previous chapter, hydrodynamically coupled motors exhibit collective dynamics quite different from those obtained by rigidly coupled motors [50; 58; 82].

Here we are going to study how the hydrodynamic coupling between motors pulling in the same cargo affects the overall cargo motion. As compared to the previous chapter we will adopt a more coarse-grained representation that, on one hand, allow us to capture the underlying dynamics, and on the other to explore different regimes without the need of more expensive numerical simulations. In the following sections we are going to perform a systematic study in which we will introduce one by one all the ingredients needed to study the overall behavior of bunches of motors moving in opposite directions pulling on membrane embedded cargoes. Instead of presenting at first the final result including all the ingredients we preferred to discuss few intermediate steps that, on one hand, can be interesting per se, and on the other allow us to characterize the different nature of the hydrodynamic coupling as compared to the rigid coupling.

3.2   Physical modeling

if motors are quite diluted, i.e. for $NR/\Lambda \ll 1$ where R is the motor linear size and Λ the size of the motor ensemble,

In order to study the collective motion of cargoes transported by opposite-pulling motors, as in the previous chapter, we model molecular motors according to a two state model. We assume motors to jump between two states a bound state, in which they strongly interact with the filament and a weakly bind state in which motors can diffuse along the filament, if they are processive, or in the cytoplasm if motors are non processive. In this case, the bound-state potential is assumed to be periodic and symmetric [50]. Such an assumption allows us to characterize the motion of non-polar motors [28] as well as bunches of positive and negative polar motors randomly distributed along the cargo. Displacing motors generate a net flow that will affect the dynamics of other motors. Therefore, in order to characterize the hydrodynamic coupling between motors pulling on a common cargo we need to solve the time evolution of motors dynamics that is described, in the overdamped regime, by N coupled Smoluchowski equations. Such a representation does not provide much insight since no analytical solution of such a system exists and the numerical solution becomes hard as N is larger then a few tens of motors. Alternatively, we can describe the dynamics of the system in

terms of the density of bound, $\tilde{\rho}(x) = 2R/l_R(x)$, and unbound, $\tilde{\sigma}(x) = 2R/l_S(x)$ motors, where R is the motor linear size and $l_R(x)$ and $l_S(x)$, respectively, are the size of the $1D$ Voronoi cell along the filament for bound and weakly bound motors[1].

In order to write down the functional Smoluchowski equation geoverning the time evolution of the probability density, $P_{\{\tilde{\rho}, \tilde{\sigma}\}}$, we discretize the system into M cells, $i = 1, ..., M$, each of which is characterized by a constant length $\Delta x = \Lambda/M$ where Λ is the system size. $\tilde{r}_i = \tilde{\rho}(x_i)\Delta x$ and $\tilde{s}_i = \tilde{\sigma}(x_i)\Delta x$ represent the, constant, value that the descrete densities take on cell i. The dynamics of bound and weakly bound motors differ. When motors are weakly bound they do not generate any force by the interaction with the filament, hence their net displacement will be affected by diffusion and by the collective hydrodynamic coupling generated by pulling motors. Motors in the bound state will experience the force generated by the interaction with the filament as well as the hydrodynamic coupling. In the next section we will discuss the functional shape of those rates. Here we just assume bound motors move to subsequent cell with rate α_i, encoding for the local as well collective forces acting on the motors, and weakly bound motors to move with rate β_i, accounting for the solely collective effect. Accordingly we define the master equation for the joint probability $P_{\{\tilde{r}, \tilde{s}\}}$ of having a distribution of bound motors, $\tilde{r}_i$ and a distribution of weakly bound motors, $\tilde{s}_i$ as:

$$
\begin{aligned}
\dot{P}_{r,s} &= \sum_i \frac{1}{2} \Big\{ \left(\mathbb{W}_{\tilde{r}_i}^{-1} \mathbb{W}_{\tilde{r}_{i-1}} - 1 \right) \alpha_{i-1} \tilde{r}_{i-1} + \left(\mathbb{W}_{\tilde{r}_{i+1}}^{-1} \mathbb{W}_{\tilde{r}_i} - 1 \right) \alpha_i \tilde{r}_i + \\
&\quad + \left(\mathbb{W}_{\tilde{s}_i}^{-1} \mathbb{W}_{\tilde{s}_{i-1}} - 1 \right) \beta_{i-1} \tilde{s}_{i-1} + \left(\mathbb{W}_{\tilde{s}_{i+1}}^{-1} \mathbb{W}_{\tilde{s}_i} - 1 \right) \beta_i \tilde{s}_i + \qquad (3.1) \\
&\quad \left(\mathbb{E}_{\tilde{r}_i} \mathbb{E}_{\tilde{s}_i}^{-1} - 1 \right) \omega_{off,i} \tilde{r}_i + \left(\mathbb{E}_{\tilde{s}_i} \mathbb{E}_{\tilde{r}_i}^{-1} - 1 \right) \omega_{on,i} \tilde{s}_i \Big\} P_{\tilde{r}, \tilde{s}}.
\end{aligned}
$$

The operators $\mathbb{W}_{\tilde{r}_i}, \mathbb{W}_{\tilde{s}_i}$ account for the change in the discrete densities $\tilde{r}_i$ and $\tilde{s}_i$ due to the displacing of the motors. In particular due to the discretization the operators $\mathbb{W}_{\tilde{r}_i}, \mathbb{W}_{\tilde{s}_i}$ are non local. In fact, as shown in fig. 3.1, the displacement of a motor will affect the values of the densities between the motor and its nearest neighborn. Such non locality, that lead to a non-trivial functional shape of the

---

[1]The Voronoi cell is defined as the free space motor at position x can access along the filament before getting in touch with their nearest-neighbor motors
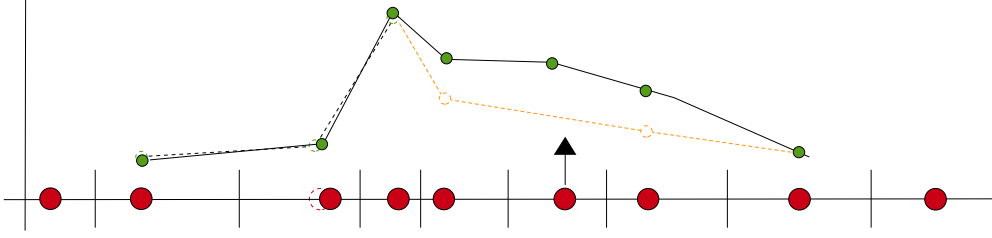
Figure 3.1: Schematic view of the Voronoi tessellation of the filament. The inverse Voronoi size is represented on the vertical axis for a typical configuration of motors. Variation in the density field due to convection (black dashed curve) or to hopping (orange dashed curve) are shown.

operators $\mathbb{W}_{\tilde{r}_i}, \mathbb{W}_{\tilde{s}_i}$, will be lost in the continuum limit. The operators $\mathbb{E}_{\tilde{r}_i}, \mathbb{E}_{\tilde{s}_i}$ are responsible for the hopping between the bound and weakly bound state. As for the operators $\mathbb{W}_{\tilde{r}_i}, \mathbb{W}_{\tilde{s}_i}$, the operators $\mathbb{E}_{\tilde{r}_i}, \mathbb{E}_{\tilde{s}_i}$ are non local. In order to study the average behavior of the eq. 3.1 it is insightful to expand the operators $\mathbb{W}$ and $\mathbb{E}$ assuming that their action will lead to "small" perturbation. The definition of what "small" is require a more detailed analysis of the processes the operators $\mathbb{W}$ and $\mathbb{E}$ represent. While the displacement of the motors along the filament leads to a smooth change in the density field, $\tilde{r}_i$ or $\tilde{s}_i$, as shown by the black dashed curve in fig. 3.1, the hopping between the bound and weakly bound state will generate larger modification in both fields, as shown by the orange dashed curve in fig. 3.1. Due to this intrinsic difference we prefer to treat the two terms separately.

When motors are convected along the filament the change in the density field is smooth if $\alpha_i dt \ll \Delta x$ i.e. if the displacement of the motor, $\alpha_i dt$, is much smaller that typical motor-motor distance captured by Δx. Therefore, for small enough dt, we can assume that the change in the densities will be much smaller that the local value of the densites and so we can represent the operators $\mathbb{W}_{r,s}$ as

$$\mathbb{W}^{\pm}_{\tilde{r}_i, \tilde{s}_i} = 1 \pm \partial_{\tilde{r}_i, \tilde{s}_i} \tag{3.2}$$

where we stop the expansion for the operators $\mathbb{W}$ at the first order since, here we

assume diffusion to be subdominant[1] Collecting the terms involving $\partial_{\tilde{r}_i, \tilde{s}_i}$ we get:

$$\dot{P}_{\{r,s\}} = \sum_i \left\{ \partial_{\tilde{r}_i} \left(\alpha_{i-1}\tilde{r}_{i-1} - \alpha_i \tilde{r}_i \right) + \partial_{\tilde{s}_i} \left(\beta_{i-1}\tilde{s}_{i-1} - \beta_i \tilde{s}_i \right) \right\} P_{r,s} \quad (3.3)$$

In order to perform the continuum limit [39] we remind that $\tilde{\rho}(x_i)\Delta x = \tilde{r}_i$ and $\tilde{\sigma}(x_i)\Delta x = \tilde{s}_i$ and we assume $\tilde{\rho}$ and $\tilde{\sigma}$ to be independent variable, that leads to $\partial_{\tilde{r}_i}\tilde{s}_j = \partial_{\tilde{s}_i}\tilde{r}_j = 0, \forall_{i,j}$. In this way the continuum limit of eq. 3.7 reads:

$$\dot{P} = \int dx \frac{\delta}{\delta\tilde{\rho}(x)} \partial_x \left(\tilde{\rho}(x)\alpha(x) \right) P + \int dx \frac{\delta}{\delta\tilde{\sigma}(x)} \partial_x \left(\tilde{\sigma}(x)\beta(x) \right) P \quad (3.4)$$

The case of the hopping is quiet different. As shown in fig. 3.1 when motors jump between the two states leads to an abrupt change in the fields r_i and s_i. Therefore it is not possible to expand the operators $\mathbb{E}_{\tilde{r}_i}, \mathbb{E}_{\tilde{s}_i}$ as we did for the operators $\mathbb{W}_{\tilde{r}_i}, \mathbb{W}_{\tilde{s}_i}$. In order to perform the continuum limit, we exploit the periodicity of the hopping rates $\omega_{on,off}$. In fact, defining

$$r_j = \sum_{i=1}^{M} \tilde{r}_i \delta(i|L - j), \quad s_j = \sum_{i=1}^{M} \tilde{s}_i \delta(i|L - j) \quad (3.5)$$

we have that
$$\sum_{i=1}^{M} \omega_i \tilde{r}_i = \sum_{i=1}^{ML/\Lambda} \omega_i r_i, \quad \sum_{i=1}^{M} \omega_i \tilde{s}_i = \sum_{i=1}^{ML/\Lambda} \omega_i s_i$$

where with $i|L$ we mean the module function. Exploiting the linearity of the operators $\mathbb{E}_i$ we can rewrite the hopping contribution to the master equation as:

$$\sum_{i=1}^{M} \left\{ \left(\mathbb{E}_{\tilde{r}_i}\mathbb{E}_{\tilde{s}_i}^{-1} - 1 \right) \omega_{off,i}\tilde{r}_i + \left(\mathbb{E}_{\tilde{s}_i}\mathbb{E}_{\tilde{r}_i}^{-1} - 1 \right) \omega_{on,i}\tilde{s}_i \right\} P_{\tilde{r},\tilde{s}} =$$

$$= \left\{ \left(\mathbb{E}_{r_i}\mathbb{E}_{s_i}^{-1} - 1 \right) \sum_{i=1}^{ML/\Lambda} \omega_{off,i}r_i + \left(\mathbb{E}_{s_i}\mathbb{E}_{r_i}^{-1} - 1 \right) \sum_{i=1}^{ML/\Lambda} \omega_{on,i}\tilde{s}_i \right\} P_{r,s}.$$

---

[1] Here, we regard diffusion of motors as subdominant in the motor current for both the bound, as well weakly bound state, since we assume that both the local, $\sim 5pN$ ($5pN$ is the typical force for Kinesins), as well the collective hydrodynamic force overwhelms the thermal contribution $k_B T/R \sim 0.4pN$, being $R \sim 10nm$ the typical motor linear size as well the periodicity of the microtubule potential

For small enough dt, the probability of having two, or more, hopping events in the same time interval dt is vanishing small. Therefore, since both R_i and S_i grow linearly with system size, their relative variations, $\delta R_i/R_i$ and $\delta S_i/S_i$ caused by the action of the operators $\mathbb{E}_i$ will be vanishing small for increasing system sizes. Hence, we can expand the operators $\mathbb{E}_i$ getting:

$$\mathbb{E}^{\pm}_{\tilde{r}_i,\tilde{s}_i} = 1 \pm \partial_{\tilde{r}_i,\tilde{s}_i} + \frac{1}{2}\partial^2_{\tilde{r}_i,\tilde{s}_i} \tag{3.6}$$

As we did for the convection term we collect the terms involving ∂_{r_i,s_i} getting:

$$\dot{P}_{\{r,s\}} = \sum_i \left\{ \omega_{off,i} \left(\partial_{\tilde{r}_i} - \partial_{\tilde{s}_i} \right) \tilde{r}_i + \omega_{on,i} \left(\partial_{\tilde{s}_i} - \partial_{\tilde{r}_i} \right) \tilde{s}_i \right\} P_{r,s} \tag{3.7}$$

and the continuum limit reads:

$$\begin{aligned}
\dot{P} = & \int dx \frac{\delta}{\delta\tilde{\rho}(x)} \left[\omega_{off}(x)\tilde{\rho}(x) - \omega_{on}(x)\tilde{\sigma}(x) \right] P + \\
& \int dx \frac{\delta}{\delta\sigma(x)} \left[-\omega_{off}(x)\rho(x) + \omega_{on}(x)\sigma(x) \right] P + \\
+ \frac{1}{2N} \int dy & \int dx \delta(x-y) \left\{ \frac{\delta^2 \omega_{off}(x)\rho(x)}{\delta\rho(x)\delta\rho(y)} + \frac{\delta^2 \omega_{on}(x)\sigma(x)}{\delta\sigma(x)\delta\sigma(y)} \right\} P
\end{aligned} \tag{3.8}$$

Finally, comparing eq. 3.8 with eq. 3.4 we notice that the different dynamics involved in the hopping and in the transport along the filament have led to functional equations for different variables. While the locally smooth displacement of motors along the filament lead to an expansion of the operators for the local fields $\tilde{\rho}(x)$ and $\tilde{\sigma}(x)$ the more abrupt hopping dynamics becomes smooth only when the densities are integrated over system size and expreesed in term of the position relative to the hopping rates:

$$\begin{aligned}
\rho(x) &= \frac{1}{\Lambda} \int_\Lambda dz \tilde{\rho}(z)\delta(z|L-x) \\
\sigma(x) &= \frac{1}{\Lambda} \int_\Lambda dz \tilde{\sigma}(z)\delta(z|L-x)
\end{aligned} \tag{3.9}$$

In order to build up a consistent continuum limit we need to express the two contributions as a function of the same fields. Accordingly, in the following we

will develop a set of systematic approximations that will allow us to recast eq. 3.4 as a function of $\rho(x)$ and $\sigma(x)$.

3.3   Approximate hydrodynamic coupling

In order to rewrite eq. 3.4 as a function of $\rho(x)$ and $\sigma(x)$ we need to clarify the role and the functional shape of the velocities $\alpha(x)$ and $\beta(x)$. In fact, $\alpha(x)$ and $\beta(x)$ respectively encode the physical forces acting on bound and weakly bound motors. Motors in the bound state move due to the force $f(x)$ provided by their strong interaction with the filament and due to the collective contribution coming from the motor-motor coupling. Due to their weaker interaction with the filament, motors in the weakly bound states are not affected by the local force term $f(x)$ and their displacement relies only on the collective coupling. The functional shape of collective coupling involved in the displacement of both bound and weakly bound motors depends on the physical forces involved. In general the collective coupling has the shape:

$$\beta(x) = \frac{1}{\gamma}\frac{1}{\Lambda}\int_{\Lambda}dz\, f(z)\tilde{\rho}(z)G(x,z) \tag{3.10}$$

where Λ is the system size, γ is the single motor friction coefficient and $G(x,z)$ is the Green function encoding the force responsible of the motor-motor interactions. For example, in the case of rigid coupling we have $G(x,z) = 1$ and for non-interacting motors $G(x,z) = 0$. In the case of hydrodynamically coupled motors we perform a multipole expansion of the Green function of the Navier-Stokes equation in the limit of vanishing Reynolds number. In the asimptotic limit of large motror-motor distances the first order of the expansion captures the dynamics[1]. In the asimptotic regime, the Green function (Oseen tensor) evaluated at distance $|z - x|$ along the direction of application of a force applied at x reads:

$$G(x,z) = \frac{1}{4\eta}\frac{1}{|z - x|} \tag{3.11}$$

---

[1]Contribution coming form higher order will affect quantitatively the results and might lead to substantial variation for larger values of bound motors density.

where η is the dynamic viscosity of the fluid. For vanishing Reynolds the Stokes equation is linear, hence contributions in the velocity field coming from different motors will sum up. In the case of hydrodynamic coupling the collective coupling has the physical nature of a drag force generated by the field $\tilde{\rho}$ of bound motors:

$$\beta(x) = \frac{1}{\gamma}\frac{3}{2}\pi\frac{R}{\Lambda}\left[\int_{-\Lambda/2}^{x-2R}\frac{f(y)\tilde{\rho}(y)}{|y-x|}dy + \int_{x+2R}^{\Lambda/2}\frac{f(y)\tilde{\rho}(y)}{|y-x|}dy\right] \qquad (3.12)$$

where we have assumed motors to be spherical ($\gamma = 6\pi\eta R$). Using eq. 3.12 we can write the velocity of bound motors as

$$\alpha(x) = \frac{1}{\gamma}\left\{f(x) + \frac{3}{2}\pi\frac{R}{\Lambda}\left[\int_{-\Lambda/2}^{x-2R}\frac{f(y)\tilde{\rho}(y)}{|y-x|}dy + \int_{x+2R}^{\Lambda/2}\frac{f(y)\tilde{\rho}(y)}{|y-x|}dy\right]\right\} \qquad (3.13)$$

Looking at eq. 3.13 we see that it involves two terms: the local term, $f(x)$ due to the interaction between bound motors and the filament, and the collective term provided by the hydrodynamic coupling. The presence of two distinct contributions, namely the local term $f(x)$ and the collective coupling is typical of soft interactions such as hydrodynamic coupling. In fact, for stronger interactions, like rigid coupling, the local term is absent and all motors undergo the same, collective force. For weakly bound motors, lacking the local forcing $f(x)$, the displacement is governed by $\beta(x) = \alpha(x) - \frac{1}{\gamma}f(x)$.

Once we have clarified how the coupling affects the velocities $\alpha(x)$ and $\beta(x)$ we will develop some systematic approximation that will allow us to recast eq. 3.13, expressed in terms of $\tilde{\rho}(x)$ and $\tilde{\sigma}(x)$, in terms of the "projected" densities $\rho(x)$, $\sigma(x)$ as given by eq. 3.9.

3.3.1 Mean field approximation

Looking at eqs. 3.12 3.13 we notice that they encode different length scales. On one hand eq. 3.13 depends on the force $f(x)$ that is periodic with period L. On the other it depends on the Oseen tensor characterized by algebraic decay, $\propto 1/r$ that leads to a Logarithmic divergence of α for increasing system size Λ. Therefore, even motors several periods apart will affect each other. However, for

large distances we can assume the Green function almost constant over the period of the force, L. Accordingly we propose the following mean field approximation:

$$\frac{3}{2}\pi R \int \frac{f(y)\tilde{\rho}(y)}{|y-x|}dy \simeq \left(\frac{1}{\Lambda}\int f(y)\tilde{\rho}(y)dy\right)\left(\frac{3}{2}\pi R\int \frac{dy}{y}\right). \qquad (3.14)$$

Eq. 3.14, that is correct if $f(x) = f_0$ and $\rho(x) = \rho_0$, exploits the $\propto 1/r$ decay typical of hydrodynamic coupling. In order to discuss the validity regime of eq. 3.14 and the order of magnitude of the error it introduces it is insightful to express both $f(x)$ and $\tilde{\rho}(x)$ in Fourier series. For the sake of simplicity, we assume that the length of the system, Λ, is a finite integer multiple of the period of the potential L. The Fourier representation is given by:

$$\begin{aligned}
f(x) &= f_0 + \delta_f(x) \\
\delta_f(x) &= \sum_{n=1}^{\infty}\left\{f_n\cos\left(\frac{\pi n x}{\Lambda}\right) + \bar{f}_n\sin\left(\frac{\pi n x}{\Lambda}\right)\right\} \\
\tilde{\rho}(x) &= \rho_0 + \delta\tilde{\rho}(x) \\
\delta_\rho(x) &= \sum_{n=1}^{\infty}\left\{\rho_n\cos\left(\frac{\pi n x}{\Lambda}\right) + \bar{\rho}_n\sin\left(\frac{\pi n x}{\Lambda}\right)\right\}
\end{aligned}$$

and the integral in eq.3.14, becomes:

$$\int \frac{f(y)\tilde{\rho}(y)}{|y-x|}dy = f_0\rho_0\int\frac{1}{|y-x|}dy + f_0\int\frac{\delta_{\tilde{\rho}}(y)}{|y-x|}dy + \rho_0\int\frac{\delta_f(y)}{|y-x|}dy + \int\frac{\delta_{\tilde{\rho}}(y)\delta_f(y)}{|y-x|}dy. \qquad (3.15)$$

Remembering that the limits of integration, as given by eq. 3.13, are $[-\Lambda/2, x-2R]$ and $[x+2R, \Lambda/2]$, the first term yields:

$$f_0\rho_0\int\frac{1}{|y-x|}dy = f_0\rho_0\ln\left(\frac{\Lambda-2x}{4R}\right) \qquad (3.16)$$

while the second two terms in eq.3.15 are composed by terms like:

$$\int_R^{\Lambda/2}\frac{\cos\left(\frac{\pi n x}{\Lambda}\right)}{|y-x|}dy,\ \int_R^{\Lambda/2}\frac{\sin\left(\frac{\pi n x}{\Lambda}\right)}{|y-x|}dy. \qquad (3.17)$$

While terms involving $\sin\left(\frac{\pi n x}{\Lambda}\right)$ are of order $O(1)$, terms involving $\cos\left(\frac{\pi n x}{\Lambda}\right)$ have a logarithmic divergence for vanishing small motors linear size, $R \to 0$. However, fixing the motor size the latter terms lead to $O(1)$ contribution for growing system size N. The last term in eq. 3.15 reads:

$$\int \frac{\delta_\rho(y)\delta_f(y)}{|y-x|}dy = \tag{3.18}$$

$$= \sum_{i,j} \int f_i\rho_j \frac{\cos^2\left(\frac{\pi n x}{\Lambda}\right)}{|y-x|} + \bar{f}_i\bar{\rho}_j\frac{\sin^2\left(\frac{\pi n x}{\Lambda}\right)}{|y-x|} + \left(f_i\bar{\rho}_j + \bar{f}_i\rho_j\right)\frac{\cos\left(\frac{\pi n x}{\Lambda}\right)\sin\left(\frac{\pi n x}{\Lambda}\right)}{|y-x|}dy \tag{3.19}$$

where, for smoothly varying $\tilde{\rho}(x)$, finite R and $N \to \infty$ the leading order is:

$$\int \frac{\delta_{\tilde{\rho}}(y)\delta_f(y)}{|y-x|}dy = k\sum_{i,j=1}^{\infty}\delta_{i,j}\left(f_i\rho_j + \bar{f}_i\bar{\rho}_j\right)k + O(1) \tag{3.20}$$

with

$$k(x) \lesssim \begin{cases} \frac{3R}{2}\ln\left(\frac{\Lambda^2-4x^2}{16R^2}\right) & 2R < x < \Lambda - 2R \\ \frac{3R}{2}\ln\left(\frac{\Lambda-2x}{4R}\right) & x < -\frac{\Lambda}{2} + 2R \\ \frac{3R}{2}\ln\left(\frac{\Lambda+2x}{4R}\right) & x > \frac{\Lambda}{2} - 2R \end{cases} \tag{3.21}$$

Collecting all terms we get the expression for the total velocity field:

$$\alpha(x) = \frac{1}{\gamma}\left[f(x) + \left\{f_0\rho_0 + k\sum_{i,j=1}^{\infty}\delta_{i,j}\left(f_i\rho_j + \bar{f}_i\bar{\rho}_j\right)\right\}k + O(1)\right] \tag{3.22}$$

Looking at eq. 3.22 we notice that, execpt for of term of order $O(1)$, the integral of the Green function and that of the density factorize. Therefore, the information regarding the physical nature of the coupling, encoded in the Green function, is constant during the evolution of motor density and affect the evolution of $\tilde{\rho}$ only as multiplicative, mean, factor. This factorization relies on the diverging nature of the hydrodynamic coupling that overweights the contribution coming from motors at larger distances, for which eq. 3.14 is a good approximation, as compared to contributions coming from nearby motors. This feature is quite remarkable since it means that systems characterized by different microscopic

interactions but sharing the same value of k will undergo similar dynamics when they are driven by the same force $f(x)$. Therefore, with a single solution we will able to discuss the dynamics of motors ensemble whose motor-motor coupling have different physical nature. Finally, we notice that, in the absence of constant forces $f_0 = 0$, the velocity field, $\alpha(x)$, does not depend on the average density, ρ_0, rather only on its dispersion captured by higher Fourier modes. Accordingly, the velocity field results to be proportional to the total force acting on the system, $k \sum_{i,j=1}^{\infty} \delta_{i,j} \left(f_i \rho_j + \bar{f}_i \bar{\rho}_j \right)$.

3.3.2 Periodic boundary conditions

In order to recast eq. 3.4 in terms of the projected densities ρ and σ we need an approximated expression of α and β as a function of ρ and σ. The key idea is that for larger system sizes the density of motor in the bulk can be assumed to depend very mildly upon its relative position with respect to the boundaries of motor ensemble. Then, the local dependence of motor density on length scales smaller than the period of the potential will be mainly governed by the hopping between bound and unbound states rather than on the boundary conditions. Following this idea, we approximate eq. 3.22 by considering only Fourier modes of motor density with wavelength smaller or equal to the period of the potential. In this way we can map our system made by $N = \Lambda/L$ potential wells into a system made by a single well by projecting the density of all the wells on a single one. As already shown in eqs. 3.9 we get:

$$\rho(x) = \frac{1}{\Lambda} \int_\Lambda dz \tilde{\rho}(z) \delta(z|L - x)$$
$$\sigma(x) = \frac{1}{\Lambda} \int_\Lambda dz \tilde{\sigma}(z) \delta(z|L - x)$$

then the densities $\rho(x)$ and $\sigma(x)$ represent respectively the density of bound and weakly bound motors at position x, relative to the period L of the force and the hopping rates, averaged over all the wells. Substituting $\rho(x)$ in eq. 3.22 and

remembering that in the case we are studying $f(x) = f_1 \cos(2\pi x/L)$ we get:

$$\alpha(x) \simeq \frac{1}{\gamma} \left[\Gamma f_1 \cos\left(\frac{2\pi n x}{L}\right) + k \left\langle f(x)\rho(x) \right\rangle_x \right] \tag{3.23}$$

with

$$\left\langle f(x)\rho(x) \right\rangle_x = \rho_1 f_1 = \frac{1}{NL} \int_{-\Lambda/2}^{\Lambda/2} f_1 \cos\left(\frac{2\pi n x}{L}\right) \rho(x) dx \tag{3.24}$$

Looking at eq. 3.23, 3.24 we notice that ρ_1 is responsible for the contribution to the force coming from the hydrodynamic coupling. If $\rho_1 = 0$ no coupling develops. Then, due to the symmetry of the ratchet potential, no current sets. On the contrary, for $\rho_1 \neq 0$, collective effects develop and we might observe the onset of a net current that breaks the symmetry. All in all the condition $\rho_1 \neq 0$ is a necessary condition for symmetry breaking.

3.4 Definition of the evolution equations

Collecting the contribution coming from eq. 3.4 and that provided by the hopping rate, eq. 3.8 we can write the functional Smoluchowski equation encoding both contributions as:

$$
\begin{aligned}
\dot{P} = \int dx \frac{\delta}{\delta\rho(x)} \left[\partial_x \left(\rho(x)\alpha(x) \right) + \omega_{off}(x)\tilde{\rho}(x) - \omega_{on}(x)\sigma(x) \right] P + \\
\int dx \frac{\delta}{\delta\sigma(x)} \left[\partial_x \left(\sigma(x)\beta(x) \right) - \omega_{off}(x)\rho(x) + \omega_{on}(x)\sigma(x) \right] P + \\
+ \frac{1}{2N} \int dy \int dx \delta(x-y) \left\{ \frac{\delta^2 \omega_{off}(x)\rho(x)}{\delta\rho(x)\delta\rho(y)} + \frac{\delta^2 \omega_{on}(x)\sigma(x)}{\delta\sigma(x)\delta\sigma(y)} \right\} P
\end{aligned}
\tag{3.25}
$$

Eq. 3.25 governs the time evolution of the probability distribution of the density fields. Then we can integrate it in order to calculate the behavior of the expectation values of the fields $\rho(x)$ and $\sigma(x)$. Under the assumption that the two fields $\rho(x)$ and $\sigma(x)$ are independent, i.e. $\frac{\delta}{\delta\rho}\sigma\frac{\delta}{\delta\sigma}\rho = 0$ and using eqs. 3.23, 3.24 we get:

$$
\begin{aligned}
\left\langle \dot{\rho}(x) \right\rangle_{\rho,\sigma} &= -\partial_x \lambda \left\langle \rho(x) \left(\Gamma f(x) + k \left\langle f(x)\rho(x) \right\rangle_x \right) \right\rangle_{\rho,\sigma} - \left\langle \omega_{off}(x)\rho(x) - \omega_{on}(x)\sigma(x) \right\rangle_{\rho,\sigma} \\
\left\langle \dot{\sigma}(x) \right\rangle_{\rho,\sigma} &= -\partial_x \lambda \left\langle \sigma(x) k \left\langle f(x)\rho(x) \right\rangle_x \right\rangle_{\rho,\sigma} + \left\langle \omega_{off}(x)\rho(x) - \omega_{on}(x)\sigma(x) \right\rangle_{\rho,\sigma}
\end{aligned}
\tag{3.26}
$$

where with $\langle...\rangle_\rho$ we mean the average over all possible density distribution $\rho(x)$ each of which weighted with probability P_ρ and with $\langle...\rangle_x$ the average over all positions x, $x \in [0, L]$ weighted with constant probability $p(x) = dx/L$. In eq. 3.26 we have introduced the auxiliary parameter $\Gamma = 0, 1$. Such a parameter has no physical meaning and it has been introduced to identify those terms that appear for soft interactions, as hydrodynamic coupling, but that are absent in the case of rigid coupling. Accordingly we will assume $\Gamma = 1$ when considering soft-hydrodynamic coupling and $\Gamma = 0$ in the case of rigid coupling.

Eqs. 3.26 are expressed in term of dimensionless variables that, for the sake of simplicity in the notation, have the same symbols of their dimensional counterparts. Eqs. 3.26 identify two main parameters, namely the dimensionless forcing $\lambda = \frac{f_1}{L\omega\gamma}$, defined via the average hopping rate

$$\omega = \langle\omega_{off} + \omega_{on}\rangle/2 \tag{3.27}$$

and the coupling parameter k.

Eq. 3.25 allows us to study the system in different regimes. Here we focus our attention on two main situations. As a first case, we assume the total local density, i.e. the density of bound plus weakly bound motors, to be constant. This constraint will lead to a simplified dynamics in which we will be able to disregard weakly bound motors dynamics. Such a strong assumption allows for a more analytical insight and so it sheds light on the underlying dynamics. On the other hand, the latter assumption leads to dynamics equivalent to those of a collection of non-processive motors in contact with a reservoir of suspended motors. This analogy relies on the fact that when motors unbind from the filament they diffuse in the $3D$ cytoplasm that act as a reservoir of motors. Motors rebind with a probability that depends on the free space available on the filament. Therefore, looking at a single system, we gain insight into two different physical situations: the dynamics of oppositely pulling motors on a common cargo and that of an ensemble of, oppositely moving, non-processive motors. We remark that due, to the presence of a reservoir of suspended motors, such an assumption reminds the *Gran Canonical* ensemble for equilibrium systems.

As an alternative scenario we relax the constraint on the local density. This

scenario accounts for the typical biological scenarios as well micro- nano- synthetic systems, where the reduced size of the system leads to intrinsic fluctuations in the density of motors that can affect the overall dynamics. By comparing this case with the previous one we will be able to discuss the role played by the local reorganization of motors density. Due to the conservation of total number of motors such a regime reminds the *Canonical* ensemble in the case of equilibrium systems.

Finally, in order to characterize the role played by the soft-hydrodynamic coupling we will compare the case of hydrodynamically coupled motors against the case of rigidly-coupled motors. This comparison has a twofold outcome: on one hand it allows us to identify the peculiar properties of hydrodynamic coupled motors, as compared to the rigid case, on the other hand we will complete prior studies on rigidly coupled motors [38] extending them to regimes that have not yet been explored.

3.5 Homogeneous total motor density

Here we study the behavior of a collection of motors pulling on opposite directions under the assumption of that the total motor density is constant. The constraint $\rho(x) + \sigma(x) == \bar{\rho}$ decouples eqs. 3.26 therefore we can study a single equation for the bound motor density:

$$\langle \dot{\rho}(x) \rangle_\rho = -\partial_x \lambda \left\langle \rho(x) \left(\Gamma f(x) + k \left\langle f(x)\rho(x) \right\rangle_x \right) \right\rangle_\rho - \left\langle \omega_{off}(x)\rho(x) - \omega_{on}(x)(\bar{\rho} - \rho(x)) \right\rangle_\rho$$

$$(3.28)$$

Looking at eq. 3.28 we can see that, as we discussed before, the shape of eq. 3.28 is the same as that of the equation governing the dynamics of non-processive motors that, by detaching from the filament after every step, will rebind according to the bulk density $\bar{\rho}$ and to the filament occupancy $\rho(x)$. In order to get an insight in the underlying dynamics governing eq. 3.28 we perform a Fourier analysis expanding both the density field $\rho(x)$ as well the hopping rates $\omega_{on,off}$. In order to simplify the notation from now on we will omit the brackets $\langle ... \rangle$. In this way

we get:

$$
\begin{aligned}
\rho(x) &= \rho_0 + \sum_{n=1}^{\infty} \left\{ \rho_n \cos\left(\frac{2\pi n}{L}x\right) + \bar{\rho}_n \sin\left(\frac{2\pi n}{L}x\right) \right\} \\
\omega_{off}(x) &= \sum_{n=0}^{\infty} \phi_n \left(1 + \cos\left(\frac{2\pi n}{L}x\right)\right) + \bar{\phi}_n \left(1 + \sin\left(\frac{2\pi n}{L}x\right)\right) \\
\omega_{on}(x) &= \sum_{n=0}^{\infty} \psi_n \left(1 + \cos\left(\frac{2\pi n}{L}x\right)\right) + \bar{\psi}_n \left(1 + \sin\left(\frac{2\pi n}{L}x\right)\right)
\end{aligned}
$$

while for the force we assume:

$$
f(x) = f_1 \cos(2\pi x/L)
$$

Then we obtain:

$$
\begin{aligned}
\dot{\rho}_0 &= \tilde{\rho} \sum_{m=0}^{\infty} \left(\psi_m + \bar{\psi}_m\right) - \rho_0 \sum_{m=0}^{\infty} \left(\phi_m + \bar{\phi}_m + \psi_m + \bar{\psi}_m\right) + \\
&\quad -\frac{1}{2} \sum_{m=0}^{\infty} \sum_{r=1}^{\infty} \delta_{m,r} \left(\phi_m \rho_r + \bar{\phi}_m \bar{\rho}_r + \psi_m \rho_r + \bar{\psi}_m \bar{\rho}_r\right) \\
\dot{\rho}_n &= -\frac{1}{2} n\pi\lambda k \bar{\rho}_n \rho_1 - \frac{1}{2} n\Gamma\pi\lambda \bar{\rho}_{n+1} - \frac{1}{2} n\Gamma\pi\lambda \bar{\rho}_{n-1} + \frac{1}{2}\tilde{\rho} \sum_{m=0}^{\infty} \delta_{m,n} \psi_m + \\
&\quad -\frac{1}{2} \sum_{r=1}^{\infty} \delta_{n,r} \rho_r \sum_{m=0}^{\infty} \left(\phi_m + \bar{\phi}_m + \psi_m + \bar{\psi}_m\right) \\
&\quad -\frac{1}{4} \sum_{m=0}^{\infty} \sum_{r=1}^{\infty} \left(\delta_{m+r,n} + \delta_{|m-r|,n}\right) \left(\phi_m \rho_r + \bar{\phi}_m \bar{\rho}_r + \psi_m \rho_r + \bar{\psi}_m \bar{\rho}_r\right) \\
\dot{\bar{\rho}}_n &= \frac{1}{2} n\pi\lambda k \rho_n \rho_1 + \frac{1}{2} n\Gamma\pi\lambda \rho_{n+2} + \frac{1}{2} n\Gamma\pi\lambda \rho_{n-2} + \frac{1}{2}\tilde{\rho} \sum_{m=0}^{\infty} \delta_{m,n} \bar{\psi}_m + \\
&\quad -\frac{1}{2} \sum_{r} \delta_{n,r} \bar{\rho}_r \sum_{m=0}^{\infty} \left(\phi_m + \bar{\phi}_m + \psi_m + \bar{\psi}_m\right) \\
&\quad -\frac{1}{4} \sum_{m=0}^{\infty} \sum_{r=1}^{\infty} \left(\delta_{m+r,n} + \delta_{m-r,n} - \delta_{r-m,n}\right) \left(\phi_m \bar{\rho}_r + \bar{\phi}_m \rho_r + \psi_m \bar{\rho}_r + \bar{\psi}_m \rho_r\right)
\end{aligned}
$$

(3.29)

3. BIDIRECTIONAL CARGO TRANSPORT

The shape of eqs. 3.29 shows the coupling cascade between different Fourier modes. In particular we notice that all modes are coupled to ρ_1 that is the mode coupled to the interaction for bound motors. On the other hand the hopping rates play the role of enhancing the coupling between modes leading to a quite involved coupling between different modes.

3.5.1 Approximate bifurcation analysis

The set of eqs. 3.29 allows to study the steady states of the system and, possibly their stability. However, since the entanglement between modes is intricate, deriving the corresponding steady states is rather involed. Since the hopping rates are the responsible of the majority of the coupling between modes, a more restrictive condition on the hopping rates might lead to a weaker coupled system of equation that possibly allows for deeper insight. Then, we assume the hopping rate to be described by a single Fourier mode, i.e. the same mode characterizing the force. In this way, both the energy injection due to the hopping between states and the mechanical forcing are accounted for by the largest wavelength mode. In particular, we assume $\phi_n = \psi_n = 0 \, \forall n$, $\bar{\phi}_n = \bar{\psi}_n = 0 \, \forall n > 1$, $\bar{\phi}_0 = \bar{\omega}_{off}$, $\bar{\phi}_1 = -\frac{1}{2}\bar{\omega}_{off}$, $\bar{\psi}_0 = \bar{\omega}_{on}$, $\bar{\psi}_1 = \frac{1}{2}\bar{\omega}_{on}$ getting

$$\omega_{off}(x) = 1 - \frac{1}{2}\sin\left(\frac{2\pi x}{L}\right) \tag{3.30}$$

$$\omega_{on}(x) = 1 + \frac{1}{2}\sin\left(\frac{2\pi x}{L}\right) \tag{3.31}$$

Such assumptions leads to the following mode cascade:

$$
\begin{aligned}
\rho_0 &= \frac{1}{2}\tilde{\rho} \\
\dot{\rho}_1 &= -\frac{1}{2}\pi\lambda k \bar{\rho}_1 \rho_1 - \frac{1}{2}\Gamma\pi\lambda \bar{\rho}_2 - \rho_1 \\
\dot{\bar{\rho}}_1 &= \Gamma\pi\lambda\rho_0 + \frac{1}{2}\pi\lambda k \rho_1^2 + \frac{1}{2}\Gamma\pi\lambda\rho_2 - \bar{\rho}_1 - \frac{1}{4}\tilde{\rho} \\
\dot{\rho}_n &= -\frac{1}{2}n\pi\lambda k \bar{\rho}_n \rho_1 - \frac{1}{2}n\Gamma\pi\lambda \bar{\rho}_{n+1} - \frac{1}{2}n\Gamma\pi\lambda\bar{\rho}_{n-1} - \rho_n \\
\dot{\bar{\rho}}_n &= \frac{1}{2}n\pi\lambda k \rho_n \rho_1 + \frac{1}{2}n\Gamma\pi\lambda\rho_{n+1} + \frac{1}{2}n\Gamma\pi\lambda\rho_{n-1} - \bar{\rho}_n
\end{aligned}
\tag{3.32}
$$

Looking at eqs.3.32, we notice that all modes are coupled to the largest wavelength mode, ρ_1 that is also responsible for the coupling with the force. Moreover, ρ_1 is also responsible for the onset of a non vanishing collective term. As shown by eq. 3.23, when $\rho_1 = 0$ the collective term is vanishing small while, for $\rho_1 \neq 0$ the collective term is non zero hence possibly leading to the development of a net motor current. Even if the proposed hopping rates lead to a simpler couupling between modes, still we obtain an infinite hierarchy. However, since the coupling between motors is forced through ρ_1, it is reasonable to assume that the longest wavelength modes will evolve more slowly and the rest of the modes will follow them adiabatically. In order to keep finite the amount of equation we are going to solve we introduce a cut-off mode that we assume to adiabatically adapt to the variations induced by longer wavelength modes. Then for the cut-off mode we have:

$$\dot{\rho}_{n_{max}} = -\frac{1}{2}\bar{n}\pi\lambda k\bar{\rho}_{n_{max}}\rho_1 - \frac{1}{2}\bar{n}\Gamma\pi\lambda\bar{\rho}_{n_{max}-1} - \rho_{n_{max}} \tag{3.33}$$

$$\dot{\bar{\rho}}_{n_{max}} = \frac{1}{2}\bar{n}\pi\lambda k\rho_{n_{max}}\rho_1 + \frac{1}{2}\bar{n}\Gamma\pi\lambda\rho_{n_{max}-1} - \bar{\rho}_{n_{max}} \tag{3.34}$$

Since eqs.3.33 are a second-order recurrence we can express all the terms as a function of two of them. The choice of the cut-off mode, $\bar{n}$, is arbitrary and will affect the linear stability analysis. Then, instead of performing a stability analysis, we look for the necessary (and possibly sufficient) condition in order to have three real roots out of eqs. 3.32. In fact, the existence of three real solution of eqs. 3.32 is the necessary conditions for the bifurcation to occur. Again we will focus on the larger wavelength mode amplitudes, namely $\rho_1, \bar{\rho}_1$, and we assume $\rho_2, \bar{\rho}_2$ to be parameters that we will determine through the numerical solutions of eq. 3.28. In this way we get a closed system for $\rho_1, \bar{\rho}_1$ that has a zero-velocity solution:

$$\rho_1 = 0, \bar{\rho}_2 = 0 \tag{3.35}$$

$$\bar{\rho}_1 = \frac{1}{\omega_0}\left(\Gamma\pi\lambda\rho_0 + \frac{1}{2}\Gamma\pi\lambda\rho_2 - \frac{1}{4}\tilde{\rho}\right) \tag{3.36}$$

and, for $\rho_1 \neq 0$ a, possibly, moving solution characterized by

$$\bar{\rho}_1 = \frac{-2}{\pi\lambda k \rho_1} \left(\frac{1}{2}\Gamma\pi\lambda\bar{\rho}_2 + \rho_1 \right) \tag{3.37}$$

where ρ_1 is obtained by solving:

$$2\left(\pi\lambda k\right)^2 \rho_1^3 + \left(4k\Gamma\left(\pi\lambda\right)^2 \left(\rho_0 + \frac{1}{2}\rho_2 \right) + 8 - \pi\lambda k\tilde{\rho} \right)\rho_1 + 4\Gamma\pi\lambda\bar{\rho}_2 = 0 \tag{3.38}$$

The necessary condition in order to have three real solutions is given by:

$$4\pi^2 k\Gamma\lambda^2 \left(\rho_0 + \frac{1}{2}\rho_2 \right) + 8 - k\pi\lambda\tilde{\rho} < 0. \tag{3.39}$$

For rigidly coupled motors, characterized by $\Gamma = 0$, eq. 3.39 is also a sufficient condition [38] for the onset of a moving solution. In this case, by rearranging eq. 3.39, the necessary and sufficient condition for symmetry breaking is:

$$k\lambda \geq \frac{8}{\pi\tilde{\rho}} \tag{3.40}$$

Then by increasing the dimensionless forcing λ we can decrease the minimum value of the coupling above which symmetry breaking occurs, as shown in fig. 3.2. For soft-hydrodynamic coupled motors, for which the local term in the force cannot be disregarded ($\Gamma = 1$), the necessary, but not sufficient, condition for symmetry breaking is

$$k \geq \frac{8}{\pi\lambda \left(\tilde{\rho} - 2\pi\lambda(2\rho_0 + \rho2) \right)}. \tag{3.41}$$

Since k is positive then λ is constrained to:

$$0 \leq \lambda \leq \frac{1}{2\pi}. \tag{3.42}$$

This behavior is rather different from the one obtained for rigidly coupled motors, as shown in fig. 3.2. For rigidly-coupled motors we found an inverse proportionality relation between the coupling k and the dimensionless forcing λ, as given
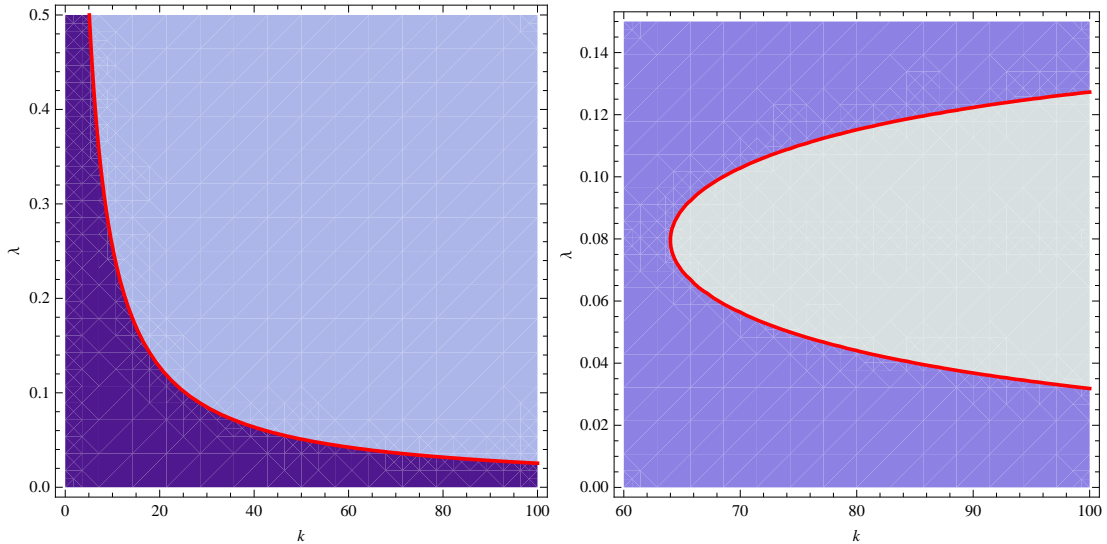
Figure 3.2: Necessary (and sufficient for $\Gamma = 0$) condition for the existence of the three real solutions of Eq. 3.39 for rigidly-coupled motors, characterized by $\Gamma = 0$, (left) and for soft-hydrodynamic coupled motors, characterized by $\Gamma = 1$, (right). Three real solutions exists when the parameters λ and k (shown on the y-axis and x-axis respectively) are inside the lighter region.

by eq. 3.40. For soft-hydrodynamic coupled motors the situation is rather different and symmetry breaking can occur only for a smaller set of values of λ, as shown by eq. 3.42. Moreover eq. 3.41 identify a critical value of the dimensionless coupling

$$\lambda_c = \frac{\tilde{\rho}}{2\pi(2\rho_0 + \rho_2) - \tilde{\rho}} \tag{3.43}$$

for which the value of coupling parameter k leading to symmetry breaking is minimum. Such a difference between rigid and soft-hydrodynamic coupled motors is rather relevant and should be detected in experiments. In fact for rigid coupled motor we expect a reduction of the minimum value of k above which symmetry breaking occurs by enlarging λ for example by increasing motor force, or decreasing the hopping rates ω. On the contrary, for soft-hydrodynamic couped motors the dependence of k on λ strongly depends on λ_c. If $\lambda < \lambda_c$ an increase of λ leads to a decrease in k as for rigidly coupled motors. However, for $\lambda > \lambda_c$ the situation is reversed and enlarging λ requires larger values of k in order to break the symmetry.

3.5.2   Numerical solution

The previous theoretical analysis, although approximate, has showed the scenarios that lead to the destabilization of a homogenoeus motor state and how a transition leading to a net motor current develops. However, in order to have a more quantitative insight on the typical velocity the system can reach and, moreover, on the typical system sizes, encoded in the coupling constant k, required for symmetry breaking, we need to solve numerically eq. 3.28. Looking at the functional shape of eq. 3.28 it is clear that an exact (i.e. up to numerical precision) solution is not trivial since it requires to calculate the average non-linear flux:

$$\langle \rho(x) \left(\Gamma f(x) + k \left\langle f(x)\rho(x) \right\rangle_x \right) \rangle_\rho \tag{3.44}$$

mediated over all possible density distribution $\rho(x)$, each of which weighted with probability P_ρ. Then, we are forced to perform an additional mean field approximation assuming:

$$\langle \rho(x) \left(\Gamma f(x) + k \left\langle f(x)\rho(x) \right\rangle_x \right) \rangle_\rho = \langle \rho(x) \Gamma f(x) \rangle_\rho + \langle \rho(x) \rangle_\rho k \langle f(x)\rho(x) \rangle_{x,\rho} \tag{3.45}$$

Tacking advantage of a second order Lax-Wendroff [77] scheme, we solve eq. 3.28 for different values of the dimensionless parameters λ and k. In particular we will study different hopping scenarios. Defining the hopping rates as:

$$\omega_{off}(x) = \max\left(\Delta\omega_{on} - \delta\omega_{on} \sin\left(\frac{2\pi x}{L} \right), 0 \right) \tag{3.46}$$

$$\omega_{on}(x) = \max\left(\Delta\omega_{off} + \delta\omega_{off} \sin\left(\frac{2\pi x}{L} \right), 0 \right) \tag{3.47}$$

we can define three main regimes. In the first one we assume $\delta\omega_{on,off} \leq \Delta\omega_{on,off}$, where the hopping rates are always non vanishing and are smoothly varying along the period of the potential. Alternatively we can consider $\delta\omega_{on} = 0$ and $\delta\omega_{off} > \Delta\omega_{off} \gg 1$ that leads to a constant binding rate and an unbinding rate localized at the bottom of the potential. This choice of the hopping rates makes our linear stability analysis about the rest state more complex since now the hopping rates are leadong to a more intricate coupling beteen the Fourier modes
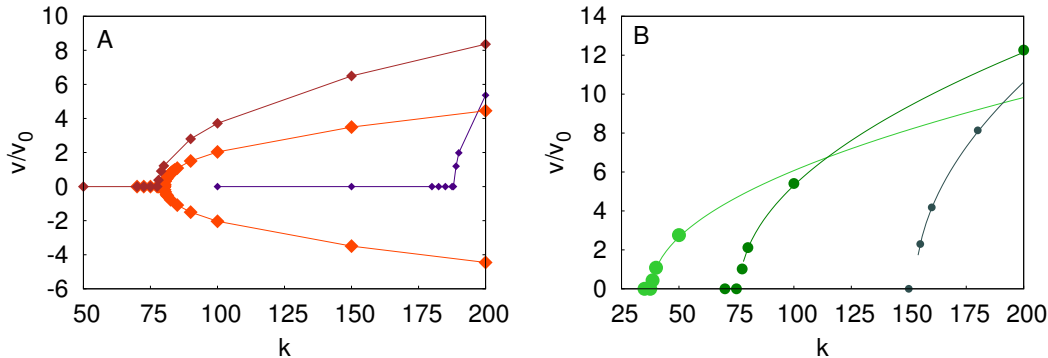
Figure 3.3: Smoothly-varying hopping rates for homogeneous local density. Velocity, normalized by the single motor velocity while sliding along the steepest part of the potential, $v_0 = f_1/\gamma$, as a function of the dimensionless coupling k as obtained from Eq. 3.28. Panel A, B refers to the case of hydrodynamic (Panel A) and rigid (Panel B) coupling, both characterized by $\Delta\omega_{on} = \Delta\omega_{off} = 1$ and $\delta\omega_{on} = \delta\omega_{off} = 1/2$ while $\lambda = 0.015, 0.05, 0.1$, $\lambda = 0.017, 0.033, 0.066$ for panel A, B respectively. Bigger points stands for larger values of λ.

as shown, for the general case, in eq. 3.32, for which the adiabatic assumtpion, even valid in principle, might require to solve more modes in order to capture the symmetry breaking. Finally we will consider the case, $\delta\omega_{off,on} > \Delta\omega_{off,on} \gg 1$, in which both binding and unbinding rates are localized at the top and at the bottom of the potential respectively.

3.5.2.1 Smoothly-varying hopping rates

The numerical solutions of eq. 3.28 for $\delta\omega_{on,off} \leq \Delta\omega_{on,off}$, are shown in fig. 3.3 for both soft hydrodynamically coupled as well as rigidly coupled motors. In the former case, shown in fig. 3.3.A the rest solution, stable for for $k < k_1$, becomes unstable for $k > k_1$ and a net motors current, breaking the left-right symmetry, sets for $k > k_1$. Such a symmetry breaking reminds the one observed [38] for rigidly coupled motors. Despite the apparent similarity, there are significantly differences between the behavior of soft and rigidly coupled motors. Fig. 3.3.B displays the spontaneous symmetry breaking for rigidly coupled motors (disregarding the dependence of k on system size). While Fig. 3.3.A shows a non monotonous dependence of k on λ, the opposite holds in Fig. 3.3.B. This differ-

ent behavior confirms what we have already found in our approximate bifurcation analysis. For rigidly coupled motors the dynamics is governed by a single dimensionless force $k\lambda$. In order to break the symmetry $k\lambda$ should overcome a threshold, $k\lambda \geq 8/(\pi\tilde{\rho})$ (as given by eq. 3.40), leading to an inverse proportionality relation between k and λ. For soft-hydrodynamic coupled motors this is not the case since, as given by eq. 3.41, two competing forces are governing the dynamics, namely the dimensionless force provided by the ratchet, λ, and the collective force coming from the hydrodynamic coupling k. The interplay between these two forces give rise to the non monotonic behavior as captured by eq. 3.41, and by fig. 3.3.A. Interestingly our approximated bifurcation analysis captures quite well the value of k for which we observe symmetry breaking and the onset of net currents. In fact for the parameters used in Fig. 3.3.A the stability analysis predicts $\lambda_c \sim 8 \cdot 10^{-2}$ and $k_c \lesssim 70$ in good agreement with numerical results. The different behavior we observe for rigid and soft-hydrodynamic coupling has significant implication for experimental situations. For example, while a reduction of λ will decrease the net flux or even prevent the onset of net currents for rigidly coupled motors, for the soft hydrodynamic case the situation is more involved. If $\lambda > \lambda_c$ a reduction in λ will favor the onset of net fluxes while for $\lambda < \lambda_c$ we recover the same behavior obtained for rigidly coupled motors.

3.5.2.2 Localized hopping rates

In the previous section we have assumed the hopping rates to have a singular Fourier representation, i.e. being concentrated on a single mode. This has lead to a simplified bifurcation analysis, eq. 3.32, that has allowed us to have an insight in the mechanism responsible for symmetry breaking. Now we want to relax that approximation and to study the dynamics of the system in the case in which the unbinding rate is localized about the minimum of the potential and the binding rate is either constant or localized at the top of the potential. The choice of the shape of the hopping rates has a twofold aim. On one hand, it allows us to characterize how the different coupling cascades between modes affect the overall dynamics, on the other it sheds light on how the symmetry breaking is affected by motors actuating in different regimes. In fact, the localization of the hoping

rates deals with the intrinsic "efficiency" of motors, as has been shown in ref. [50]. Then this study will allow us to clarify the relevance of such "efficiency" in the symmetry breaking.

Localized unbinding rate and constant binding rate In this case, we assume the unbinding rate to be localized at the bottom of the ratchet potential and a constant binding rate, namely $\delta\omega_{on} = 0$ and $\delta\omega_{off} > \Delta\omega_{off} \gg 1$. For both soft-hydrodynamic and rigid coupling, we observe a dramatic change in the nature of the symmetry breaking. In fact, while for smoothly varying hopping rates, we observe a supercritical pitchfork bifurcation, as shown in fig. 3.3, in this case we observe a subcritical pitchfork bifurcation, as shown in fig. 3.4. Such difference is remarkable since in the case of a supercritical bifurcation the order parameter (ensemble velocity) changes smoothly with the control parameter (the coupling parameter k) while for a subcritical bifurcation the order parameter changes abruptly as the control parameter overcome the bifurcation point. On the other hand, for a supercritical bifurcation the number of stable states jumps from one (the rest state) to the two moving states (one per direction). Then, for $k > k_1$ if the system is affected by random fluctuation in the hopping rates it will, randomly, jump between the two moving states leading to a bistable behavior as has been previously reported [38]. In the case of a subcritical bifurcation, the situation is rather different since for $k_1 < k < k_2$ there are three stable states, namely the two moving states and the rest state. Then, in the presence of noise, the overall system dynamics will differ from the one previously described since now the system can, randomly, set in the rest state than alternating the bistable behavior with long pauses. Such a behavior has been observed experimentally in the transport of Golgi apparatus [70], Acto-Myosin systems [2] and Kinesin-Dynein ensembles [56].

When the hopping rates are not represented by a single Fourier mode, the coupling between modes become more involved. Then, in principle, we need more than 2 parameters, namely λ and k, to describe the system. However, if we vary only the amplitude of the the ratchet force, f_1, then we observe, for soft-hydrodynamic coupling, a non-monotonous behavior identifying an optimal value of the dimensionless forcing λ for which we can break the symmetry similarly to

Figure 3.4: Localized unbinding rate and delocalized binding rate for homogeneous local density. A,B: velocity, normalized by the single motor velocity while sliding along the steepest part of the potential, $v_0 = f_0/\gamma$, as a function of the dimensionless coupling k as obtained from Eq. 3.28. A: hydrodynamic coupling characterized by $\lambda = 1 \cdot 10^{-2}, 2 \cdot 10^{-2}, 4 \cdot 10^{-2}$ with bigger points standing for larger values of λ and with $\Delta\omega_{off} = -4$ and $\delta\omega_{on} = 5$. B: rigidly coupled motors, characterized by the parameter values given in table 3.1, a bigger bright points, b intermediate points, c smaller dark points. C,D: average density of motors as a function of the coupling parameter k for the same values of the parameters as in panel A,B respectively for C,D.

	$\Delta\omega_{off}$	$\delta\omega_{off}$	$\Delta\omega_{on}$	$\delta\omega_{on}$	ω	f/γ	λ
a	-400	500	1	0	10^{-2}	10^{-2}	10^{-1}
b	-40	50	1	0	10^{-1}	10^{-2}	$1/2 \cdot 10^{-1}$
c	-4	5	1	0	10^{-1}	10^{-2}	10^{-1}

Table 3.1: Sets of parameters used for the data about localized unbinding rate and delocalized binding rate shown in fig. 3.4.B.

what observed for smoothly-varying hopping rates. On the other hand, if we vary both the force and the amplitude of the hopping ω (defined in eq. 3.27) the situation is rather different, as shown in fig. 3.4.B and table 3.1, and the relation between k and λ becomes not trivial even for rigidly-coupled motors ($\Gamma = 0$).

Another feature linked with the higher number of modes involved in the Fourier representation of the hopping rates deals with the average motor density. For smoothly varying hopping rates the average density is conserved during the dynamics, independently of the value of k, as given by the first equation of eqs. 3.32. However, for more involved hopping rates, we should look at the more general expansion as given by eqs. 3.29. Fig. 3.4.C,D show a counterintuitive scenario for which while decreasing the coupling (hence the velocity) the density increases until it reaches the maximum for the state characterized by zero net velocity. Hence, the velocity enhancement shown in fig. 3.4.A,B is not due to an increase of the pushing motors, rather to a better reorganization of a more dilute ensemble of motors.

As shown in the panels in fig. 3.4, both rigid and hydrodynamic coupling lead more diluted clusters to move at higher velocities. Then, in this scenario a reduction in the number of pulling motors, and therefore of the energy consumption, leads to an improvement of cluster performances. Interestingly such a behavior is typical for this choice of the hpping rates. For smoothly varying hopping rates the density is fixed by the initial condition ans it does not depend neither on time neither on the coupling parameter k. An increase in the motors performance upon reduction of the enrgy consumption reminds what we have already discussed in the previous chapter where the energy cost per unit step was strongly reduced by the hydrodynamic coupling between motors. As in the previous case, motors are not pulling against a load so it is not possible to define a thermodynamic efficiency since all the energy injected in the system is dissipated in the fluid.

Localized unbinding and binding rate   In this case, we assume that both binding and unbinding rates are localized at the top and the bottom of the ratchet potential respectively. In this case, we find that the supercritical pitchfork bifurcation happens for vanishing small values of the coupling parameter k for both rigid and soft-hydrodynamic coupling, as shown in both panels of fig. 3.5. The
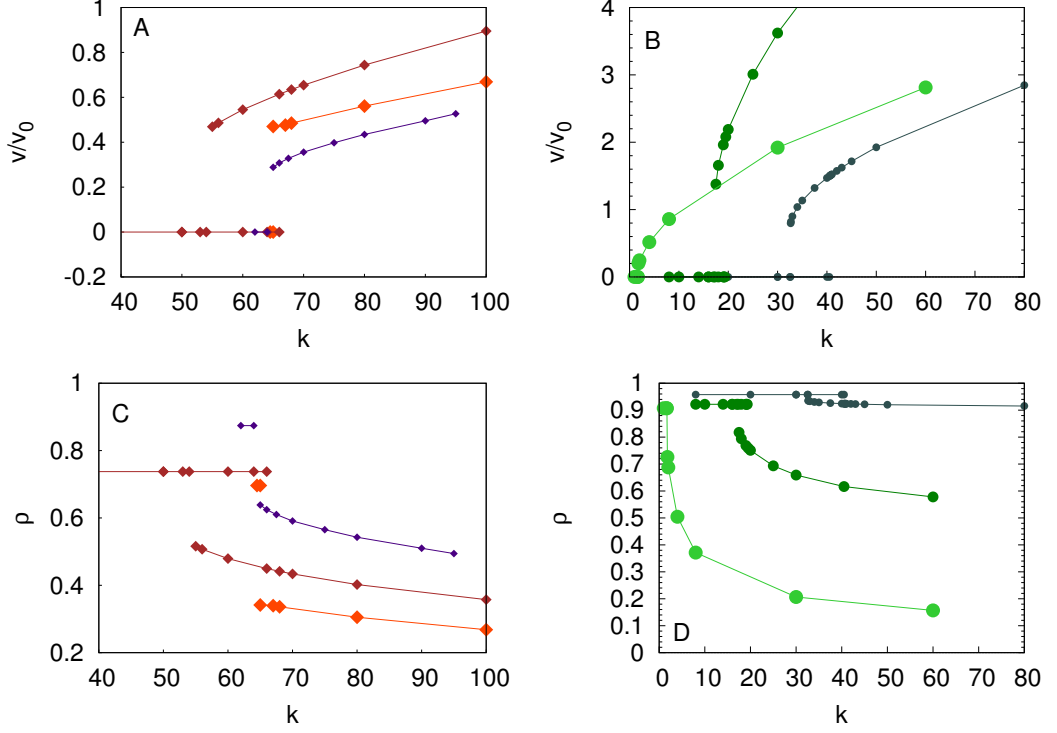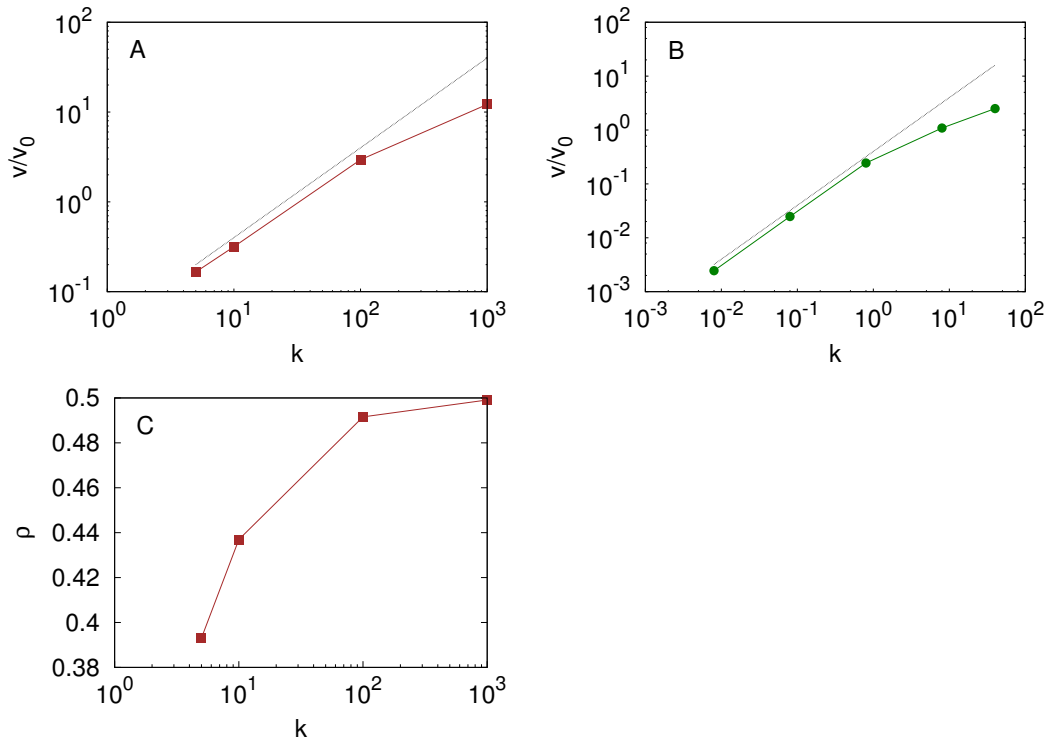
Figure 3.5: Both localized unbinding and binding rate for homogeneous local density. Velocity, normalized by the single motor velocity while sliding along the steepest part of the potential, $v_0 = f_0/\gamma$, as a function of the dimensionless coupling k as obtained from Eq. 3.28. A: hydrodynamic coupling characterized by $\lambda = 10^{-2}$ with bigger points standing for larger values of λ and with $\Delta\omega_{off,on} = -4$ and $\delta\omega_{off,on} = 5$. B: rigidly coupled motors, characterized by $\lambda = 1/2$ and $\Delta\omega_{off,on} = -0.4$, $\delta\omega_{off,on} = 0.5$. C: average density as a function of the coupling parameter k for the same values of the parameters as in panel A.

scenario we have just described has not been found in experiments and it predicts the lack of stable rest state. In order to understand weather this regime is experimentally achievable or not we should discuss the role played by the noise in the dynamics. In fact, in the absence of noise, our study predicts that the rest state is always unstable. However, for real systems, noise (possibly due to thermal fluctuations) will be present and possibly play a relevant role. In fact, the system size decrease with the coupling parameter k. Therefore for vanishing k the system size will decrease and fluctuations in the dynamics will be relevant. In this regime, the system will hop continuously between the two moving steady states therefore leading to an overall vanishing velocity. An high frequency sampling of such trajectories should show an enhanced dispersion in the center of mass position, reminder of the quick jumps the system does between the two moving stable steady states. Interestingly, we find that while for the soft-hydrodynamic case the density decreases upon increase of the coupling and lead to a density-velocity relation similar to that obtained in the previous case, for rigid coupled motors the density does not show an evolutions and sticks to its initial value.

3.6 Inhomogeneous total motors density

In previous sections, we have characterized the dynamics of ensembles of opposite-displacing motors pulling on a common cargo under the constraint of homogeneous total motor density. However, such a constraint is quite restrictive since real systems, characterized by finite number of motors, will be characterized by inhomogeneities in the local density. In particular, for rigidly bound motors such inhomogeneity can be regarded as a quenched disorder since, due to the common force acting an all motors, the density inhomogeneities in the initial conditions will never relax. On the contrary, for soft-hydrodynamic motors inhomogeneities in the density might lead to novel dynamics prevented in the case of homogeneous distributions. When we relax the local density constraint and we allow the local total density $\rho(x) + \sigma(x)$ as well the single densities $\rho(x)$ and $\sigma(x)$ to vary, eqs. 3.26 do not decouple and we have to solve both of them at the same time.

3.6.1 Approximate bifurcation analysis

In order to gain insight in the underlying dynamics we expand both densities, ρ and σ in their Fourier series:

$$\rho(x) = \rho_0 + \sum_{n=1}^{\infty} \rho_n \cos\left(\frac{2\pi nx}{L}\right) + \bar{\rho}_n \sin\left(\frac{2\pi nx}{L}\right) \tag{3.48}$$

$$\sigma(x) = \sigma_0 + \sum_{n=1}^{\infty} \sigma_n \cos\left(\frac{2\pi nx}{L}\right) + \bar{\sigma}_n \sin\left(\frac{2\pi nx}{L}\right) \tag{3.49}$$

In the case of homogeneous total motors density we have gained insight by assuming that both the hopping rates and the force are represented by a single Fourier mode. Therefore, here we make the same assumption:

$$
\begin{aligned}
f(x) &= f_1 \cos\left(2\pi x\right) \\
\omega_{off}(x) &= 1 + \omega_1 \sin\left(2\pi x\right) \\
\omega_{on}(x) &= 1 - \omega_1 \sin\left(2\pi x\right)
\end{aligned}
$$

getting:

$$
\begin{aligned}
\dot{\rho}_0 &= -2\left(\rho_0 - \sigma_0\right) - \omega_1\left(\bar{\rho}_1 - \bar{\sigma}_1\right) \\
\dot{\rho}_1 &= -\pi\lambda k\bar{\rho}_1\rho_1 - \pi\lambda\Gamma\bar{\rho}_2 - \left(\rho_1 - \sigma_1\right) + \frac{1}{2}\omega_1\left(\bar{\rho}_2 + \bar{\sigma}_2\right) \\
\dot{\bar{\rho}}_1 &= 2\Gamma\pi\lambda\rho_0 + \pi\lambda k\rho_1^2 + \pi\lambda\Gamma\rho_2 - \left(\bar{\rho}_1 - \bar{\sigma}_1\right) + \frac{1}{2}\omega_1\left(\rho_2 - 2\rho_0 + \sigma_2 - 2\sigma_0\right) \\
\dot{\sigma}_0 &= 2\left(\rho_0 - \sigma_0\right) + \omega_1\left(\bar{\rho}_1 - \bar{\sigma}_1\right) \\
\dot{\sigma}_1 &= -\pi\lambda k\bar{\sigma}_1\rho_1 + \left(\rho_1 - \sigma_1\right) - \frac{1}{2}\omega_1\left(\bar{\rho}_2 + \bar{\sigma}_2\right) \\
\dot{\bar{\sigma}}_1 &= \pi\lambda k\sigma_1\rho_1 + \left(\bar{\rho}_1 - \bar{\sigma}_1\right) - \frac{1}{2}\omega_1\left(\rho_2 - 2\rho_0 + \sigma_2 - 2\sigma_0\right)
\end{aligned}
\tag{3.50}
$$

where we have truncated our expansion at the longest wavelength mode i.e. the period of the potential L. In the case of rigidly coupled motors, $\Gamma = 0$, we can solve the system of eqs. 3.50 considering $\rho_2, \bar{\rho}_2$ and $\sigma_2, \bar{\sigma}_2$ as parameters.

Substituting:

$$
\begin{aligned}
a_i &= \rho_i + \sigma_i \\
\bar{a}_i &= \bar{\rho}_i + \bar{\sigma}_i \\
b_i &= \rho_i - \sigma_i \\
\bar{b}_i &= \bar{\rho}_i - \bar{\sigma}_i
\end{aligned}
$$

and doing some algebra we have been able to solve the system and, after linearizing it about the rest steady state, to calculate the eigenvalues and eigenvectors. The conservation of the total mass, $\rho_0 + \sigma_0 = \bar{\rho}$, already provide an eigenvalue $\xi_0 = 0$. For the other eigenvalues we find:

$$
\begin{aligned}
\xi_1 &= 0 \\
\xi_2 &= -2 \\
\xi_3 &= -4 \\
\xi_4 &= -\frac{1}{8}\left(2\bar{a}_1\lambda k\pi + \psi + \sqrt{-64\bar{a}_1\lambda k\pi + (2\bar{a}_1\lambda k\pi + \psi)^2}\right) \\
\xi_5 &= -\frac{1}{8}\left(2\bar{a}_1\lambda k\pi + \psi - \sqrt{-64\bar{a}_1\lambda k\pi + (2\bar{a}_1\lambda k\pi + \psi)^2}\right)
\end{aligned}
\tag{3.51}
$$

with

$$
\psi = 8 + \lambda k\pi\omega_1(a_2 - 2a_0) \tag{3.52}
$$

The first eigenvalue vanishes, identifying an additional conserved quantity, on the top of total mass, leading to $\bar{a}_1(t) = \frac{\omega_1}{\omega_0}b_0(t)$. Looking at the shape of the eigenvalues ξ_4, ξ_5, we expect a first bifurcation when $2\bar{a}_0\lambda k\pi + \psi \geq 0$ that, substituting eq. 3.52 in the expression for ξ_4 and ξ_5, leads to:

$$
k\lambda > \frac{8}{\pi(2\bar{a}_1 + \omega_1(a_2 - 2a_1))} \tag{3.53}
$$

and a second bifurcation might[1] arise depending on the sign of the argument of the square root. Eq. 3.53 is the condition for the onset of a net current.

---

[1] Strinctly pseaking our approximate bifurcation analysis is valid only close to the first bifurcation point since we have linearized the sisyem bout the rest steady state

Comparing eq. 3.53 with the equivalent expression obtained for homogeneous motor total density, eq. 3.40, we notice that the two conditions share the same structure. However, while for eq. 3.40 the relation between k and λ is an explicit expression of the parameters, for eq. 3.53 this is not the case since the system of eqs. 3.50 is underdetermined due to the linear dependence between the equation for $\dot{\rho}_0$ and $\dot{\sigma}_0$. Then the amplitudes of the modes involved in eq.3.53 need to be calculated from the numerical solution of eqs. 3.26. For the case of soft-hydrodynamic coupling, $\Gamma = 1$, the situation is more involved and we have not been able to solve analytically the system of equations 3.50 and so to perform the linear stability analysis.

3.6.2 Numerical solution

As for the constant local density case we are not able to directly numerically solve eqs. 3.26 since they involve an integration in the functional space of ρ and σ. Hence we need to do an additional mean field approximation, as we did in the case of homogeneous density, according to which we will consider:

$$
\begin{aligned}
\langle \rho(x)\left(\Gamma f(x) + k \langle f(x)\rho(x)\rangle_x\right)\rangle_{\rho,\sigma} &= \langle \rho(x)\Gamma f(x)\rangle_{\rho,\sigma} + k \langle \rho(x)\rangle_{\rho,\sigma} \langle\langle f(x)\rho(x)\rangle_x\rangle_{\rho,\sigma} \\
\langle \sigma(x)k \langle f(x)\rho(x)\rangle_x\rangle_{\rho,\sigma} &= k \langle \sigma(x)\rangle_{\rho,\sigma} \langle\langle f(x)\rho(x)\rangle_x\rangle_{\rho,\sigma}
\end{aligned}
\tag{3.54}
$$

The numerical solution[1] of eqs. 3.26, under the approximation provided by eqs. 3.54, has led to very different behavior for rigidly coupled, $\Gamma = 0$, or soft-hydrodynamic coupled, $\Gamma = 1$, motors. Due to the relevant differences, even in the qualitative behavior between the rigid and the hydrodynamic coupling, we prefer to discuss the two cases separately.

3.6.2.1 Rigid coupling

For rigidly coupled motors, $\Gamma = 0$, we observe two subsequent bifurcations, as shown in fig. 3.6. Above the first bifurcation point, k_1 the system undergoes sustained oscillations with vanishing average velocity, while above the second bifurcation point, k_2 the system breaks the longitudinal symmetry and it acquires

---

[1] we have used a second order Lax-Wendroff [77] scheme extended to the case of two fields
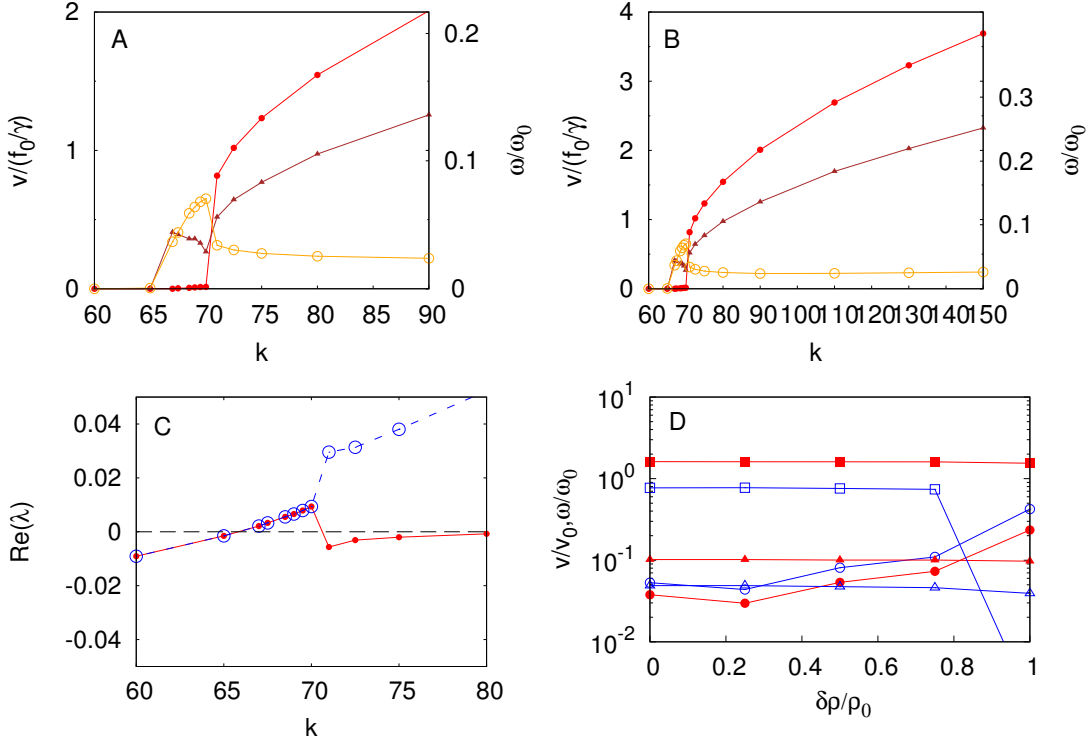
Figure 3.6: Smoothly-varying hopping rates for rigidly coupled motors and in-homogeneous motors total density. A: bifurcation and onset of net current as a function of the coupling parameter k; solid (red) dots represent the average velocity, empty (orange) circles represent the second moment of the velocity while triangles (brown) the frequency of the velocity oscillations. B: bifurcation scenario for larger range of coupling parameter k, all other parameters take the same values as in panel A. C: real part of the eigenvalues ξ_4 and ξ_5, as given by eqs. 3.51, as a function of k. The values of the higher modes amplitude are token from the numerical solutions of eqs. 3.26 under the mean field approximation given by 3.54. D: average velocity (squares), variance of the velocity (circles) and frequency of velocity oscillations (triangles) as a function of the amplitude of the quench disorder $\delta\rho/\rho_0$ for $k = 65.7$ (empty points) and $k = 80$ (solid points).

a net motion characterized by a non vanishing average velocity modulated by small amplitude oscillations. Such a behavior is consistent with the approximate linear stability analysis we performed, see eqs. 3.51. Fig. 3.6.B shows the behavior of the relevant eigenvalues upon variation of the coupling k, where the value of a_0, $\bar{a}_1$ and a_2 are token from the numerical solution of eqs.3.26. For $k < k_1$ the relevant eigenvalues are negative, ensuring the stability of the rest state. When $k_1 < k < k_2$ the eigenvalues have an imaginary part, see eqs. 3.51, hence leading to oscillations. At $k = k_2$ a second bifurcation occurs and the system acquires a net velocity modulated by small oscillations. For $k > k_2$, the linear stability analysis predicts the absence of oscillations in disagreement with our numerical results that show a net average velocity modulated by small amplitude oscillations. Therefore, in this regime, our approximate linear stability analysis fail to capture the oscillating behavior, possibly induced by higher modes that we have disregard in our approximated analysis.

The conservation of total mass, togheter with the rigid coupling lead to a quenching of the disorder provided by initial conditions. In fact, since the same collective force is acting on all motors their mutual position are frozen, therefore density heterogeneities in the initial condition will be frozen along the time evolution of the the system dynamics. We have studied how the overall dynamics is affected by the amplitude of the quench disorder, $\delta\rho/\rho_0$, quantified by the ratio between the amplitude of the noise in the initial conditions, $\delta\rho = \int(\rho(x)-\rho_0)^2 dx$, and the average density, ρ_0. For $k > k_2$ the effect of the amplitude of the quench disorder is neglegible and a net velocity modulated by small amplitude oscillation is obtained for all the cases we have analyzed. On the contrary, for $k_1 < k < k_2$, the system is quite sensitive to the amplitude of the quench disorder. Fig. 3.6.C shows that reducing the value of the quench disorder the system acquires a net motion with nonvanishing average velocity modulated by small amplitude oscillations. Fig. 3.6.C shows as well that by reducing the amplitude of the quench disorder leads to a reduction of the amplitude of the oscillations modulation the average velocity, while the frequency of such oscillations is quite insensitive to variations in $\delta\rho/\rho_0$.

3.6.2.2   Soft-hydrodynamic coupling

In the numerical analysis of eqs. 3.26, we observe, in some regimes, the development of large densities that correspond to a tendency of motors to accumulate. As we have discussed in the previous chapter, motors ensembles can develop clusters [62], or shock waves [1], when the total number of motors is conserved. In these situations the motion of motors is controlled by short range interactions and excluded volume, absent in eqs. 3.26. Interestingly when weakly bound motors are in contact with a reservoir and eqs. 3.26 reduces to eqs. 3.28, no accumulation is observed, showing that, in this scenario, short range interaction play a minor role as compared to the long range hydrodynamic interactions governing the behavior shown in Fig. 3.6. On the contrary, when the total number of motors is conserved and motors keep track of the position where they jump to the weakly bound state, we observe the onset of large accumulation of motors.

However, we have seen that motor accumulation remains finite if both binding and unbinding rates are sharply peaked ($\Delta\omega_{on,off} < \delta\omega_{on,off}$) at the maximum or minimum of the potential respectively, see Fig. 3.7.A. Numerical solution of eqs. 3.26 is shown in Fig. 3.7.A. For smaller values of the coupling k the rest state is the only stable solution. When $k \gtrsim 60$ a saddle-node bifurcation of cycles [87] occurs and new stable solution characterized by a net velocity whose value oscillates, with frequency ω_v, about a non vanishing average. The amplitude of the oscillations is smaller than the average value, see Fig. 3.7.A, hence the system always moves in the same direction with speed modulated by small amplitude oscillations. The time evolution of the densities $\tilde{\rho}(x)$ and $\tilde{\sigma}(x)$ is characterized by traveling waves for both motor densities.

The traveling wave regime can be understood as follows. When moving under the action of the driving potential, motors in the bound state push through hydrodynamic interactions, motors in the diffusive state. As motors reach the bottom of the potential they jump, with rate ω_{off}, to the diffusive state. Now the remaining motors in the bound state push, the majority of the motors in the unbound state untill they reach the hopping region and they rebind, with rate ω_{on}, to the filament and a new cycle starts.

Increasing the value of k, at fixed λ, or reducing the value of λ at fixed k,
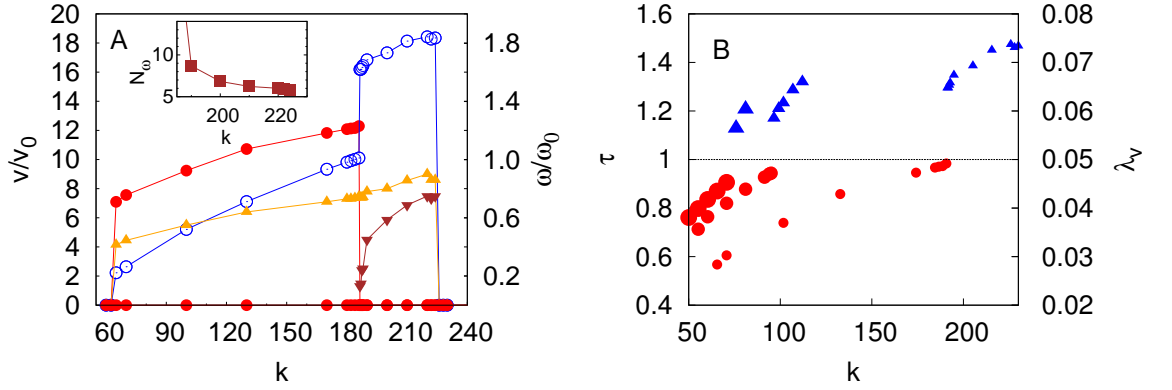
Figure 3.7: Soft-hydrodynamic coupling and inhomogeneous motors total density. A: average velocity (red solid dots), velocity variance (open blue dots), normalized by the single motor velocity while sliding along the steepest part of the potential, $v0 = f_0/\gamma$, sustained oscillations frequency, ω_v (yellow upside triangles) and frequency of inversion in the bistable regime Ω_v (brown downside triangles), normalized the hopping rate ω_0 as obtained by the solution of eqs. 3.26 as function of k. Ω_v has been magnified by a factor of 10 for sake of clearness. Hopping rates are characterized by $\Delta\omega_{on,off} = -1$, $\delta\omega_{on,off} = 2$. Inset: number of oscillation between subsequent velocity switch, $N_\omega = 2\omega_v/\Omega_v$, in the bistable regime B: dimensionless time $\tau = 2v_\rho/\omega_0\delta$ governing the stability of the sustained oscillation (see text), and effective dimensionless forcing, $\lambda_v = v/\omega_0 L$, as a function of the dimensionless coupling k. Bigger points stands for larger values of $\lambda = f_0/\omega_0 L\gamma = 4\cdot10^{-3}, 6.7\cdot10^{-3}, 10^{-2}$ while point type emphasizes the sustained oscillation (circles) or bistable (triangles) regime.

we observe the onset of larger accumulations of motors about the region of non-vanishing hopping rates breaking the dilute motor regime assumed in eqs. 3.26. To have an insight in this regime we have introduced a, local, regularization that allows to redistribute locally the excess of motors[1]. Exploiting this regularization we can explore a wider range of values of k and λ. Interestingly we observe a second bifurcation at $k \simeq 180$ above which the system becomes bistable. In the bistable phase we observe that the velocity still oscillates with frequency ω_v about a non vanishing average value, v, and the sign of v switches with frequency Ω_v. Hence, for time scales larger than Ω_v^{-1} the average velocity of the system vanishes and the bistable behavior, similar to the one experimentally observed [40], develops. The parameter governing this transition is the dimensionless time, $\tau = 2v_\rho/\omega_0\delta$, defined as the ratio between the, average, hopping time $\frac{1}{2}\omega_0^{-1}$ where the factor $\frac{1}{2}$ accounts for the non-constant shape of the hopping rate, and the time a particle spends in the region in which the hopping rate is non vanishing, δ, being pushed at a speed v_ρ [2] by the other motors. As shown in Fig. 3.7.B, when $\tau \ll 1$ the time needed to jump between the two states ω_0^{-1} is much smaller than the time particle spends in crossing the hopping region, hence the majority of the motors rebind and the system undergoes sustained oscillations. On the contrary, when $\tau \gtrsim 1$ the two time scales are comparable and part of the motors in the unbound state cannot jump back to the bound state and will not contribute to the next cycle. Such loss of active motors affects subsequent oscillations. These effects sum up until the system switches the sign of the average velocity on time scales of the order of Ω_v. The number of oscillations between two subsequent switching events, $N_\omega = 2\omega_v/\Omega_v$, decreases for increasing k, as shown in the inset of Fog. 3.7.A. For increasing k the two time scales approach, $N_\omega \to 1$, and the bistability disappears leaving the rest state as the only steady state.[3]

This bistable regime just described is typical of soft hydrodynamically coupled motors. In this scenario motors oscillations develop due to fluctuation in the local

---

[1]When the density exceeds the maximum value, $\tilde{\rho}_{max}$, the excess of motors are redistributed in the first-neighbor sites along the lattice used for the numerical solution of eqs. 3.26.

[2]v_ρ is the average velocity provided that the majority of the motors are in the bound state. For values of k close to the second bifurcation, $k \simeq k_2$, we have $v_\rho \sim 3 \cdot v$

[3]This bifurcation scenario, that includes subcritical Hopf-like bifurcation, is typical of scenarios where the bifurcation is not governed by the neighborhood of the steady fix point rather by larger regions of the phase space [87].
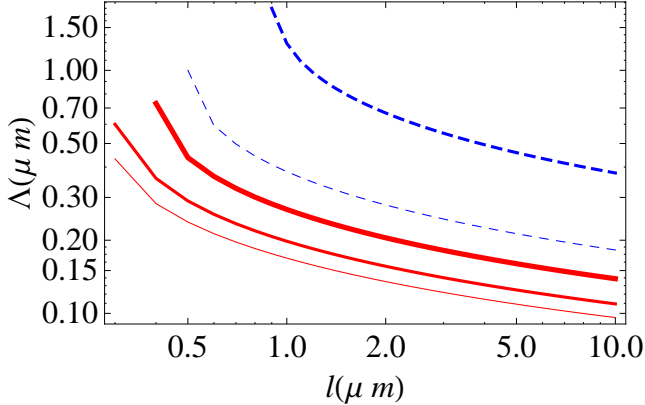
Figure 3.8: *2D hydrodynamic coupling.* Minimum system size, calculated from Eq. 3.56 for symmetry breaking (solid lines) and for bistable onset (dashed lines) as a function of l for motor pulling on membranes. R is of the order of the membrane thickness $\sim 4nm$ leading to $R \sim 1/2L$. Thicker lines stands for larger values of k. $k = 75, 60, 50$ and $k = 60, 50$ for the solid (dashed) lines respectively.

density that allows for, local, reorganization of motor densities. Such feature is absent when we disregard unbound motor dynamics, as is when weakly bound motors are in contact with a reservoir, see fig. 3.6, or when density fluctuation are suppressed by rigidly coupled motors, as in [38]. Bistability can be recovered in the latter regime [38], as well in the former (data not shown), when the hopping dynamics is affected by a weak noise. Hence, in these regimes, bistability sets for intermediate motors ensemble sizes and it vanishes for increasing system sizes, for which the noise becomes negligible. On the contrary, for hydrodynamic coupling the bistability arises by increasing the system size, encoded in k, and persists for a finite range of values of k before the rest state becomes the only stable steady state.

3.7   Hydrodynamic coupling and biological scenarios

The hydrodynamic coupling has an intrisic diverging nature that leads the overall coupling betwee particles in a system to grow with system size. therefore, for

hydordynamic coupling, the coupling parameter k and the system size Λ show a monotonous relation. In particular, for the case of hydrodynamically-induced bidirectional cargo transport, in principle, it is possible to identify two means responsible for the onset hydrodynamic coupling. On one hand motors pulling on the same cargo are hydrodynamically coupled through the local fluxes of cytoplasm they generate as they displace. On the other hand, when motors are pulling on membrane-covered cargoes, such as organelles or vesicles, the liquid nature of the membrane on which motors pull can lead to an additional hydrodynamic coupling. In particular the latter will develop in the lipid bilayer that act as a thin sheet of fluid [1] for which the green function of the Navier-Stokes equation will be the $2D$ Oseen tensor. In this view motors are coupled by two means at the same time and, we should take both of them into account when calculating $\alpha(x)$ and $\beta(x)$. The ratio, $l = \eta_{2D,mem}/\eta_{3D,cyt}$, between the membrane $2D$ viscosity, $\eta_{2D,mem}$ and the cytoplasmic $3D$ viscosity, $\eta_{3D,cyt}$ defines the typical length, l, above which the $3D$ contribution will be the dominant, while vice-versa stands for distances shorter than l. In the following we assume that motors and the membrane-embedded molecules bridging them to the membrane are rigidly coupled. In this view eqs. 3.25 are describe the overall motion of motors and molecules provided we take into account both $2D$ and $3D$ contributions in the velocity fields $\alpha(x)$ and $\beta(x) = \alpha(x) - \mu f(x)$. For $r < l$ the relevant contribution is the $2D$ and the $2D$ Oseen tensor reads [26]:

$$G(r) = \ln \frac{l}{r} \tag{3.55}$$

where $l = \eta_{2D,mem}/\eta_{3D,cyt}$. Such an interaction leads to the coupling parameter

$$k_{2D} = 2\left[M + \ln \frac{l}{M} - R - \ln \frac{l}{R}\right] \tag{3.56}$$

For the $3D$ contribution coming from the coupling provided by the cytoplasm, the hydrodynamic coupling is accounted for, at first order, by the $3D$ Oseen's tensor:

$$G(r) = \frac{3}{2} R \frac{1}{r} \tag{3.57}$$

---

[1]The bilipidic membrane thickness is typically $\simeq 4nm$

that leads to the coupling parameter

$$k_{3D} = 3R \ln \frac{\Lambda}{2R} \tag{3.58}$$

where Λ is the system size.

Once we know the relation between the system size, Λ, and the coupling parameter, k, we can recast the dependence of the motors ensemble state of motion in terms of the size of the ensemble. The interactoin between motors strongly depedns on the ratio, l, between the cytoplasm and the membrane density. Assuming the cytoplasm viscosity to be $\eta_{3D,cyt} \in [10^{-1}; 10^{-2}] \, Pa \cdot sec$ [65] and membrane viscosity to be $\eta_{2D,mem} \in [5 \cdot 10^{-7}, 10^{-8}] \, Pa \cdot sec \cdot m$ [21] we obtain $l \in [10^{-1}, 10] \, \mu m$ that is the typical range in biological situations for which the typical velocity is $v \sim 0.1 \, \mu m$ [17]. The hopping rate can be assumed $\omega_0 \simeq \alpha 10^2 \, sec^{-1}$, being α the inverse of the efficiency [1]. We can define an effective dimensionless forcing $\lambda_v = \frac{v}{\omega_0 L} = 5 \cdot 10^{-2}$ for $\alpha = 2$ i.e. 50% efficiency. The same parameter calculated for the curve in Fig. 3.7.A gives $\lambda_v = 2.8 \cdot 10^-2$ underling the biological relevance of the regime shown. Fig. 3.8 shows that for $l \sim 1 \mu m$, systems as small as $\Lambda \sim 0.2 \, \mu m$ will undergo hydrodynamically-induced symmetry breaking, while slightly larger systems $\Lambda \sim 0.5 \, \mu m$ will develop bistability. Eq. 3.58 gives a non monotonous dependence of Λ on R, $\Lambda = 4R e^{\frac{2kL}{3R}}$ whose minimum value grows as $\Lambda_{min} = 4eR$. In the latter case, motors pulling cargoes of $\sim 0.1 - 1 \, \mu m$ size will undergo symmetry breaking for systems of the order of $10 - 100 \, \mu m$ underling the relevance of the $3D$ hydrodynamic coupling for larger systems such as neurons, or in technological applications as in microfluidic devices.

3.8 Conclusions

We have shown that the hydrodynamic coupling between molecular motors can be responsible for the experimentally observed bidirectional transport of cargoes.

---

[1] ω_0 has been calculated assuming that the hopping is instantaneous and that the velocity of the motor is $v = 1\mu m/sec$ the time spent to move one period $L = 10 \, nm$ is $\tau = 10^{-2} \, sec$ for 100% efficiency and the typical length is $L \sim 10 \, nm$. For smaller efficiencies, $1/\alpha$, we get $\tau = 1/\alpha 10^{-2} \, sec$

Due to the hydrodynamic nature of the coupling the system size plays a relevant role in the onset of motion. Moreover the presence of local forcing term in addition to the collective coupling leads to unexpected dynamics such as oscillations and bistability absent in the case of rigid coupling. In order to characterize the peculiarity of the hydrodynamic coupling, we have compared the dynamics of hydrodynamically coupled motors against those arising for rigidly coupled motors in different scenarios.

In the case of constant density, where the overall mobility is governed by bound motor dynamics, allows for a more analytical insight. In this scenario, we have identified the dimensionless motor-filament forcing term λ, as the parameter controlling the difference between hydrodynamically and rigidly coupled motors. In fact, while the dynamics of hydrodynamically coupled motors is affected by both the hydrodynamic coupling, captured by k, and the local forcing, captured by λ, for rigidly coupled motors the local forcing is absent since all motors move according to the collective force k. The competition between two contribution, namely Λ and k, to the local force leads hydrodynamically coupled motors to undergo quite different dynamical regimes as rigidly coupled motors whose overall dynamics is governed by the collective force, k. In particular, while for rigidly coupled motors increasing the dimensionless local forcing λ decreases the value of k at which bifurcation occurs, for hydrodynamically coupled motors it appears a critical value of λ for which the value of k is minimum. Such a difference can lead to different routes to regulate the onset of net currents and should be detectable experimentally.

When relaxing the constraint on the local density, we have observed novel dynamical regimes for both, rigidly as well hydrodynamically coupled motors. For rigidly coupled motors density inhomogeneities are quenched since, due to the rigid coupling, the inhomogeneity in the density provided by the initial condition cannot be relaxed. Hence, the amplitude of the intial inhomogeneties in the density is a relevant parameter and it controls the onset of sustained oscillations about a vanishing velocity. For larger values of the quenched disorder we observe oscillations of motors velocity about a vanishing average, while reducing the amplitude of the quenched disorder leads to the onset of sustained oscillations about a non vanishing average velocity. In the case of hydrodynamic coupling density

inhomogeneities are not quenched, rather we have observed several regimes including large accumulations, that reminds those reported in ref. [1] or the clusters we have observed in the previous chapter, traveling waves and bistability.

Interestingly we found that not only the physical nature of the interaction (hydrodynamic or rigid bound) but also the details of motor intrinsic dynamics, encoded in the functional shape of the hopping rates, leads to different, unexpected, dynamical regimes. In fact, different shapes of the hopping rates leads to quite diverse bifurcation scenarios for both, rigid and soft-hydrodynamical coupling. In the case of constant local density, for unbinding rates localized at the bottom of the potential and unlocalized bounding rate the bifurcation becomes subcritical as compared to the supercritical observed for smoother hopping rates. The change in the nature of the bifurcation remarks a dramatic variation in the underlying dynamics. For example we have observed that for intermediate values of the coupling parameter k an extended region of bistability develops. In such a scenario the presence of fluctuation will induce the system to switch between two moving states (one per direction along the filament) and a rest state. Interestingly similar dynamics has been reported in recent experiments where Golgi apparatus [70], Acto-Myosin systems [2] and Kinesin-Dynein ensembles [56] have been observed to alternate bidirectional motion interspersed with long pauses. For rigidly coupled motors the dependence of the nature of the bifurcation on the functional shape of the hopping rates is not sensitive to the constraint on the homogeneity of the density. Similar functional shape of the hopping rates has given similar bifurcation scenarios for both homogeneous as well quenched inhomogeneous density profiles. On the contrary, hydrodynamically coupled motors are strongly affected by the homogeneity of the density. While for homogeneous density we have observed the onset of net currents for different functional shape of the hopping rates, relaxing such a constraint leads to large accumulation of motors whenever the hopping rates are not sharply localized at the extrema of the potential.

The difference between rigid and soft-hydrodynamic coupling is encoded in the role played by the local forcing term λ. Thanks to our coarse-grained appriach we have been able to capture the essential parameters, namely λ and k governing the dynamics. Therefore different soft-potentials leading to the same value of k and λ

will undergo the same dynamics. For motors pulling on cargo the hydrodynamic coupling can have two origins. In fact, motor-motor hydrodynamic coupling can be provided by both the $3D$ cytoplasm and by the $2D$ membrane motors are pulling on. Interestingly when accounting for the $2D$ contribution we observed symmetry breaking or even bistability for typical system sizes of the order of tens of motors, $\simeq 10^{-1} \mu m$, hence underlying that hydrodynamic coupling can open a new, biologically feasible, route for bidirectional transport.

4. Confinement-induced rectification

4.1 Introduction

In this chapter we study the dynamics of a single molecular motor displacing in the presence of geometrical constraints that will enter in the overall dynamics as an additional contribution to the overall potential whose physical origin relies on the modulation of the free space available for the motor, and that can be introduced as an effective entropic barrier. In this view such contribution has been addressed as an entropic barrier [48; 99]. The relevance of entropic barriers to promote transport [13; 79] in confined environments has been recognized in a variety of situations that include molecular transport in zeolites [9], ionic channels [16], or in microfluidic devices [3; 25], where their shape explains, for example, the magnitude of the rectifying electric signal observed experimentally [66]. In fact, spatially varying geometric constraints provide themselves an alternative means to rectify thermal fluctuations [83]. Modulations in the available explored region lead to gradients in the system effective free energy, by inducing a local bias in its diffusion that can promote a macroscopic net velocity for aperiodic channel profiles [83] or due to applied alternating fields [93].

The out of equilibrium condition characterizing molecular motors affect their dynamics, when geometrically confined, in a different way as compared to passive particles. In fact, it has been shown that breaking detailed balance due to the presence of unbalanced forces acting on a system causes rectification of thermal fluctuations and leads to new dynamical behaviors, very different from those

observed in equilibrium situations [6; 41].

We will study the dynamics of single molecular motors embedded in a varying section channel. We will exploit the two state model to characterize the dynamics of the motor. However, the coupling between the energy injected in the system by the motor and the geometrical confinement is not peculiar of molecular motors, rather it can apply also to synthetic particles that are brought out of equilibrium by other means. Therefore, in order to extend our study to more general situations we will analyze different ratcheting schemes leading to rectification. All these schemes deal with Brownian particles in a periodic potential in an overall out of equilibrium state. Such systems are generally called Brownian Ratchet referring to the thought experiment introduced by Smoluchowski [86] and later reproposed by Feynman [30]. In this more general view, we will analyze the interplay between rectification and confinement, and will characterize the new features associated with confined Brownian ratchets (CBR). We show that the presence of strong cooperative rectification [63; 64] between the ratchet and the confinement may lead to rectification even when none of them can rectify the particle current on their own. Such an interplay strongly affects particle motion. To understand the mutual influence between both rectifying sources, we will analyze three different ratchet models, namely the flashing ratchet, the two-level ratchet and a thermal ratchet. In the first two cases, the equilibrium is broken by the energy injected in the system through the intrinsic ratchet mechanism as it happens in the case of molecular motors. In the third one, the driving force is a thermal gradient that couples to the probability current, hence inducing a, local, Soret effect.

4.2 Physical modeling

A Brownian ratchet, with diffusion constant D, under the action of a potential, $V(\mathbf{r}, t)$, moving in a confined environment characterized by a varying cross-section channel of width, $h(x, z)$, such as the one depicted in Fig. 4.1, can be characterized in terms of the probability distribution function (pdf), $P(\mathbf{r}, t)$, which obeys the Smoluchowski equation

$$\frac{\partial}{\partial t} P(\mathbf{r}, t) = \nabla \cdot [\beta D \nabla W(\mathbf{r}) P(\mathbf{r}, t) + D \nabla P(\mathbf{r}, t)] \tag{4.1}$$

where $\beta^{-1} = k_B T$ is the inverse of the temperature, T, at which the particle diffuses, while k_B stands for Boltzmann constant. Instead of being regarded as an explicit boundary condition, the geometrical constraint can be included, alongside any additional potential the diffusing particle may be subject to, as an effective potential

$$W(\mathbf{r}) = \begin{cases} V(x), & |y| \leq h(x), \& |z| \leq L_z \\ \infty, & |y| > h(x) \text{ or } |z| > L_z \end{cases} \tag{4.2}$$

where we have considered, without lack of generality, that the long axis of the channel coincides with the axis x, that particles cannot penetrate the confining channel walls, and that the channel is periodic, $W(\mathbf{r}) = W(\mathbf{r} + L\mathbf{e}_x)$, of length L, as shown in Fig. 4.1, and has a finite section. If the channel width varies slowly, $\partial_x h \ll 1$, one can assume that the particle equilibrates in the transverse section on time scales smaller than the ones when the particle experiences the variations in channel section. It is then possible to factorize the pdf

$$P(\mathbf{r}, t) = p(x, t) \frac{e^{-\beta W(\mathbf{r})}}{e^{-\beta A(x)}} \tag{4.3}$$

$$e^{-\beta A(x)} = \int_{-L_z}^{L_z} \int_{-h(x)}^{h(x)} e^{-\beta W(\mathbf{r})} dy dz. \tag{4.4}$$

By integration over the channel section one arrives at

$$\frac{\partial}{\partial t} p(x, t) = \partial_x \left\{ D \left[\beta p(x, t) \partial_x A(x) + \partial_x p(x, t) \right] \right\}, \tag{4.5}$$

the Fick-Jacobs equation [48; 78; 99], an effective one-dimensional Smoluchowski equation that determines the particle diffusion along the channel. Such motion is characterized by the local effective free energy

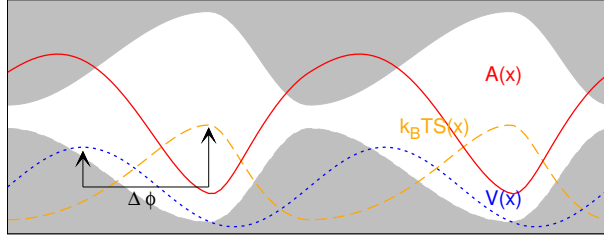$$A(x) = V(x) - k_B T \ln[2h(x)] \tag{4.6}$$

Figure 4.1: Brownian ratchet and entropic barriers. A Brownian motor moving in a confined environment will be sensitive to the free energy $A(x)$ (solid) generated by the ratchet potential $V(x)$ (dotted) and the entropic potential (dashed), $-k_BTS(x)$, induced by the channel shape.

where $S(x) = \ln(2h(x))$ accounts for the entropic contribution due to confinement. One can identify an entropy barrier,

$$\Delta S = \ln\left(\frac{h_{max}}{h_{min}}\right) \tag{4.7}$$

in terms of the maximum, h_{max}, and minimum, h_{min} channel apertures. Therefore, $\partial_x A(x)$ is the driving force that contains entropic, $\partial_x S(x)$, and enthalpic, $\partial_x V(x)$, contributions. The range of validity of the Fick-Jacobs equation has been analyzed [14; 79], and it has been found that introducing the varying diffusion coefficient [78]

$$D(x) = \frac{D_0}{\left[1 + \left(\frac{\partial h}{\partial x}\right)^2\right]^\alpha} \tag{4.8}$$

with $\alpha = 1/3, 1/2$ for $3D, 2D$ respectively, with the reference diffusion $D_0 = k_BT/\gamma(R)$ and $\gamma(R) \propto R$, enhances the range of validity of the factorization assumption, Eq. (4.4). Although we will keep $D(x)$ for completeness, the results do not change qualitatively if a constant diffusion coefficient, D_0, is considered instead.

The free energy difference over a channel period, as calulate by integrating eq. 4.6 is given by

$$\Delta F = \int_0^L \partial_x A(x)dx \tag{4.9}$$

and it governs the particle current onset. Looking for the steady solution of

eq. 4.5 in a periodic system, $p_{st}(0) = p_{st}(L)$, we find that a net current, $J \neq 0$, arises only when $\Delta F \neq 0$, which can have both an enthalpic, $\int_0^L V(x)dx \neq 0$, and entropic, $k_B T \int_0^L \ln(h(x))dx \neq 0$, origin. Indeed the picture of $A(x)$ as a free energy is suggestive: a net current sets only when the difference in free energy along the period is not vanishing. Clearly, at equilibrium, periodic potentials, $V(x)$, in periodic channels, $h(x)$, do not give rise to any difference in the free energy and consequently no current. The relative performance of a ratchet in an uniform channel can be quantified in terms of the dimensionless parameter

$$\mu_0 = \frac{L\bar{v}}{\tilde{\mu}\Delta F_0} \tag{4.10}$$

defined as the ratio between the Brownian ratchet average speed, $\bar{v} = \frac{1}{L}\int_0^L J(x)dx$ with $J(x) = D\left[\beta p(x,t)\partial_x A(x) + \partial_x p(x,t)\right]$ derived from eq. 4.5, and the average speed of a particle with mobility $\tilde{\mu} \equiv \beta D_0$ under the action of a uniform effective force, $f_0 \equiv \Delta F_0/L$. In the absence of intrinsic ratchet rectification, $\Delta F_0 = 0$ and μ_0 remains 1. If the ratchet leads to an intrinsic rectification, the interplay between ratcheting and confinement can be alternatively quantified interns of the dimensionless parameter

$$\mu = \frac{L\bar{v}}{\tilde{\mu}\Delta F} \tag{4.11}$$

that accounts for the overall free energy drop ΔF. For a uniform channel, when rectification is purely enthalpic, $\mu/\mu_0 = 1$. Therefore, deviations of μ/μ_0 from 1 constitute a convenient means to address the role of entropic constraints to particle rectification; $\mu/\mu_0 > 1$ indicates that the geometrical constraints cooperate with the force associated to the Brownian ratchet to induce an efficient cooperative rectification, larger than the one obtained in an unstructured environment, while the opposite holds for $\mu/\mu_0 < 1$. The absolute value of μ gives additional information. When $\mu > 1$ the performance of the cooperative rectification beats the one obtained under a constant force $f \equiv \Delta F/L$. μ also easily identifies the non-linear rectifying regime, when $\partial_f \mu \neq 0$.

To analyze the interplay between the Brownian ratchet and confinement, we will consider that all Brownian ratchets are subject to the same underlying, driv-

ing periodic potential,

$$V_0(\mathbf{r}) = V_0 \left[\sin \frac{2\pi}{L} x + \lambda \sin \frac{4\pi}{L} x \right] \tag{4.12}$$

This is a simple potential, explored in detail previously in which rectification is controlled by a single parameter, λ [81]. We will consider a channel width that varies with the same periodicity as V_0 and with a similar functional dependence

$$h(x) = h_0 - R + h_1 \sin \left[\frac{2\pi}{L} (x + \phi_0) \right] + h_2 \sin \left[\frac{4\pi}{L} (x + \phi_0) \right] \tag{4.13}$$

where h_0 is the average channel section and h_1 and h_2 determine its modulation. In particular h_2 is responsible for the symmetry of the channel along its transverse axis. When $h_2 \neq 0$ the left-right symmetry along the channel longitudinal axis is broken while, for $h_2 = 0$, the left-right symmetry of channel along its longitudinal axis is restored. h_{max} and h_{min} depend both on h_1 and h_2 and the dephasing, ϕ_0. The latter will be useful to displace the geometrical and potential modulations, as discussed in the next Sections. The particle radius, R, affects the available transverse section and will hence contribute to the entropic barrier, Eq.(4.7).

4.3   Ratchet models

In order to characterize the impact of confinement in the rectification of a Brownian particle, we will consider three different types of complementary, well-established ratchet models that have the same periodicity that the geometric confinement.

4.3.1   Flashing ratchet

A colloidal particle subject to a periodic external potential

$$V(x) = \mathcal{V}_1 V_0(x) \tag{4.14}$$

behaves as a flashing ratchet when the random force breaks detailed balance [59]. The parameter $\mathcal{V}$ allows to modify he amplitude of the potential V keeping fixed

V_0. This can be simply achieved with a Gaussian white noise with a second moment amplitude $g(x) = \sqrt{D(x) + Q\left(\partial_x V_0(x)\right)^2}$ [80], where Q controls Brownian rectification. The Fick-Jacobs equation for such a flashing ratchet in a varying-section channel reads

$$\frac{\partial}{\partial t}p(x) = \frac{\partial}{\partial x}\left\{g(x)\frac{\partial[p(x)g(x)]}{\partial x} + D(x)p(x)\frac{\partial\beta A(x)}{\partial x}\right\}, \qquad (4.15)$$

which reduces to equilibrium diffusion for $Q = 0$. For $Q > 0$ detailed balance is broken and net fluxes arise when

$$\beta\Delta F = \int_0^L \left[\frac{D(x)\partial_x A(x)}{g(x)^2} + \frac{\partial}{\partial x}\ln g(x)\right] dx \neq 0. \qquad (4.16)$$

Since $\int_0^L \partial_x \ln g(x)dx = 0$ for a periodic channel, particle currents emerge from the interplay between both the entropic and enthalpic forces, encoded in $A(x)$ and the position-dependent noise, $g(x)$. Three dimensionless parameters governs the Brownian ratchet performance: $\beta\mathcal{V}_1$ and ΔS quantify the relevance of the enthalpic and entropic contributions, respectively, while $Q/(L^2 D_0(R))$ determines rectification.

4.3.2 Two state molecular motor

The two-state ratchet model constitutes a standard, simple framework to describe molecular motor motion. A Brownian particle jumps between two states, $i = 1, 2$, (strongly and weakly bound) that determine under which potential, $V_{i=1,2}$, it displaces [51]. A choice of the jumping rates $\omega_{12,21}$ that break detailed balance, jointly with an asymmetric potential of the bound sate, $V_1(x)$, determines the average molecular motor velocity $v_0 \neq 0$. The conformational changes of the molecular motors introduce an additional scale that will compete with rectification and geometrical confinement. Infinitely-processive molecular motors remain always attached to the filament along which they displace and are affected by the geometrical restrictions only while displacing along the filament; accordingly, we choose channel-independent binding rates $\omega_{21,p}(x) = k_{21}$. On the contrary, highly non-processive molecular motors detach frequently from the biofilament

and diffuse away; an effect we account for considering a channel-driven binding rate, $\omega_{21,np}(x) = k_{21}/h(x)$. Motors jump to the weakly bound state only in a region of width δ around the minima of $V_1(x)$, with rate $\omega_{12} = k_{12}$. Accordingly, the motor densities in the strong(weak) states, $p_{1(2)}$ along the channel follow [51]

$$
\begin{aligned}
\partial_t p_1(x) + \partial_x J_1 &= -\omega_{12}(x)p_1(x) + \omega_{21}(x)p_2(x) \\
\partial_t p_2(x) + \partial_x J_2 &= \omega_{12}(x)p_1(x) - \omega_{21}(x)p_2(x)
\end{aligned}
\tag{4.17}
$$

where $J_{1,2}(x) = -D(x)\left[\partial_x p_{1,2}(x) + p_{1,2}(x)\partial_x \beta A_{1,2}(x)\right]$ stands for the current densities in each of the two states in which motor displaces. Depending on the motor internal state, two free energies, $A_{1,2}(x) = V_{1,2}(x) - k_B T S(x)$, account for the interplay between the biofilament interaction and the channel constraints. Since molecular motors can jump between two internal states, the corresponding expression for the overall free energy drop, ΔF, must be generalized to account for these internal changes where, the overall free energy drop is identified from a two dimensional particle flux. This system is also characterized by three dimensionless parameters: $\beta \mathcal{V}_1$ and ΔS control the amplitude of the enthalpic and entropic contribution, respectively, while ω_1/ω_2 quantifies the departure from detailed balance.

4.3.3 Thermal ratchet

As a last example, we will consider a Brownian particle moving in a varying-section channel under the influence of a local temperature gradient. In the absence of entropic barriers, the transport induced by the imposed temperature gradient has been analyzed previously [15; 90]. By assuming local equilibrium along the radial directions the probability distribution function obeys [99]:

$$
P(\mathbf{r}, t) = p(x, t) \frac{e^{\frac{-W(\mathbf{r})}{K_B T(x)}}}{e^{\frac{-A(x)}{k_B T(x)}}}
\tag{4.18}
$$

and the corresponding Fick-Jacobs equation reads

$$\frac{\partial}{\partial t}p(x,t) = \frac{\partial}{\partial x}\left\{\mu(x)p(x,t)\left(T(x)\frac{\partial}{\partial x}\frac{A(x)}{T(x)} + \right.\right.$$
$$\left.\left. + V(x)\frac{\partial}{\partial x}\ln T(x)\right) + \mu(x)\frac{\partial}{\partial x}[T(x)p(x,t)]\right\}, \tag{4.19}$$

where we keep the phenomenological dependence of the diffusion on the channel width through the local mobility $\mu(x) = \beta D(x)$. The overall free energy drop can be expressed as

$$\Delta F = \int_0^L \left[\frac{\partial}{\partial x}\frac{A(x)}{T(x)} + \left(\frac{V(x)}{T(x)} + 1\right)\frac{\partial}{\partial x}\ln T(x)\right]dx. \tag{4.20}$$

which differs qualitatively from the one obtained for the flashing ratchet, eq. 4.16. For a periodic thermal ratchet under a periodic temperature gradient, the entropic contribution, $\int_0^L \frac{\partial}{\partial x}\frac{A(x)}{T(x)}dx$, vanishes and does not contribute to ΔF. Therefore, rectification in a periodic thermal ratchet, quantified by $\Delta F = \int_0^L \frac{V(x)}{T(x)}\partial_x \ln T(x)dx$, can only develop from an interplay between the enthalpic and temperature variations [15; 75]. Although both the flashing and the thermal ratchet are characterized by a multiplicative noise, their different physical origin is at the basis of this different response. For the thermal ratchet the spatial inhomogeneity affects both the amplitude of the fluctuations and the local equilibrium distribution while for the flashing ratchet the noise amplitude is regarded as an effective coarse-graining of a molecular mechanism that is decoupled from the underlying equilibrium properties of the Brownian particle. In fact, if we would (inconsistently) neglect the spatial dependence of the temperature in the equilibrium distribution of the thermal ratchet that appears in Eq. (4.18), we would derive an ΔF_T,

$$\Delta F_T = \int_0^L \frac{\partial_x A(x)}{T(x)} + \partial_x \ln T(x)dx \tag{4.21}$$

qualitatively analogous to the one obtained for the flashing ratchet, Eq. 4.16. A similar result, and hence the possibility of constrained-controlled rectification, is obtained if one assumes that the temperature becomes anisotropic. This corresponds to situations where the equilibration transverse to the channel is de-

termined by a temperature that differs from the one characterizing the particle diffusion along the channel. Such situations can develop if there is an intrinsic mechanism for energy dissipation, as has been reported. e.g. in vibrated granular gases [89].

4.4   Fully symmetric case

We will first consider the case of symmetric ratchet and entropic potentials, implemented for $h_2 = \lambda = 0$. Under these conditions, current rectification is not possible when entropic and enthalpic forces act separately. We will show in this Section that rectification may arise due to the interplay between both drivings, when they are phase shifted by an amount ϕ_0.

Flashing Ratchet   Fig. 4.2.a shows the particle current obtained by solving eq. 4.15 under the steady-state condition $\dot{p}(x) = 0$. As shown in fig. 4.2.a, a net particle current develops when the phase shift, ϕ_0, is not a multiple of π. Such a particle flux is the result of the interplay between confinement and the potential leading to particle rectification. In fact, eq. 4.16 together with eq. 4.6 clearly show that, if the channel and the ratchet are not in phase, $\phi_0 \neq 0$, the overall free energy drop, eq. 4.16, is finite and a net current develops. The Fick-Jacobs equation identifies ϕ_0 and ΔS as the relevant parameters that control rectification. ϕ_0 is responsible for the spatial symmetry breaking for any finite channel modulation, ΔS. As shown in Fig.4.2.b, ΔS, quantifies the changes in the system geometrical properties by tuning the particle radius, R, or the channel corrugation, h_1.

Particle current varies smoothly with the other dimensionless parameters, $\mathcal{V}_1$ and Q. For example, the value of ΔS providing the maximum current is only weakly affected by a drop of Q of two orders of magnitude, as shown in Fig. 4.2.b. For small values of Q, the particle velocity does not increase monotonously with $\mathcal{V}_1$. While Fig. 4.2.c indicates that there exists a finite value of $\mathcal{V}_1$ at which particle flux is optimal, Fig. 4.2.d shows that the particle current increases monotonously with Q. Since both the channel corrugation and the ratchet potential are symmetric, Fig. 4.2.a is symmetric under inversion of the velocity and dephasing

angle. Therefore, a uniform distribution of ϕ_0 will not induce any net current, but any asymmetric distribution will.

The insets of Fig. 4.2 display the changes of the dimensionless velocity, μ (Eq. (4.15)), as a function of the relevant dimensionless parameters. They show that there are regimes where confinement and the ratchet potential cooperate to induce an efficient particle rectification, $\mu > 1$, and regimes where they compete with each other, partially hindering rectification, $\mu < 1$. Both regimes depend weakly on confinement, as shown in the top panels of fig. 4.2, while μ is significantly affected by the magnitude both of the ratcheting potential, $\mathcal{V}_1$, and the noise amplitude, Q. In particular, $\mu < 1$ is typical for small values of $\mathcal{V}_1$ and Q while, upon increasing both $\mathcal{V}_1$, and Q, the $\mu > 1$ regime arises. As the magnitude of $\mathcal{V}_1$ increases, μ decreases drastically and the net current eventually vanishes.

Two state model Fig. 4.3.a shows that a net particle current develops when the ratchet and the channel corrugation are out of registry. The symmetry of the channel and rectifying potentials imply that the velocity profile is invariant if both axis of the figure are inverted; hence a uniform distribution of ϕ_0 will not induce a net current, but any asymmetric distribution will. The internal reorganization of the molecular motor as it moves along the channel allows for qualitatively new scenarios with respect to the rectification features observed for the flashing ratchet. For example, Figs. 4.3.b and 4.3.c show that the particle flux can reverse its direction as ΔS and $\mathcal{V}_1$ increase, respectively, although flux reversal is more sensitive to channel corrugation. This flux reversal can be exploited to induce particle separation according to their size (due to the implicit dependence of ΔS on particle radius, R), or the differential particle response to $\mathcal{V}_1$.

Although ΔS captures the essential features of net molecular motor motion, Fig. 4.3.b shows separate sensitivity to the rest of the geometrical channel parameters, h_0, h_1, as well as motor size R. Such sensitivity is remarkable at smaller entropic barrier magnitudes where the confining-tuned diffusion coefficient, eq.(4.8), plays a relevant role. If $h_1 \to 0$ then both the entropic barrier and the modulation of the diffusion coefficient vanish. On the contrary if R or h_0 decrease at fixed h_1, then $\Delta S \to 0$ but the modulation of the diffusion coefficient persists, allowing for rectification. As ΔS increases, the sensitivity to the sepa-
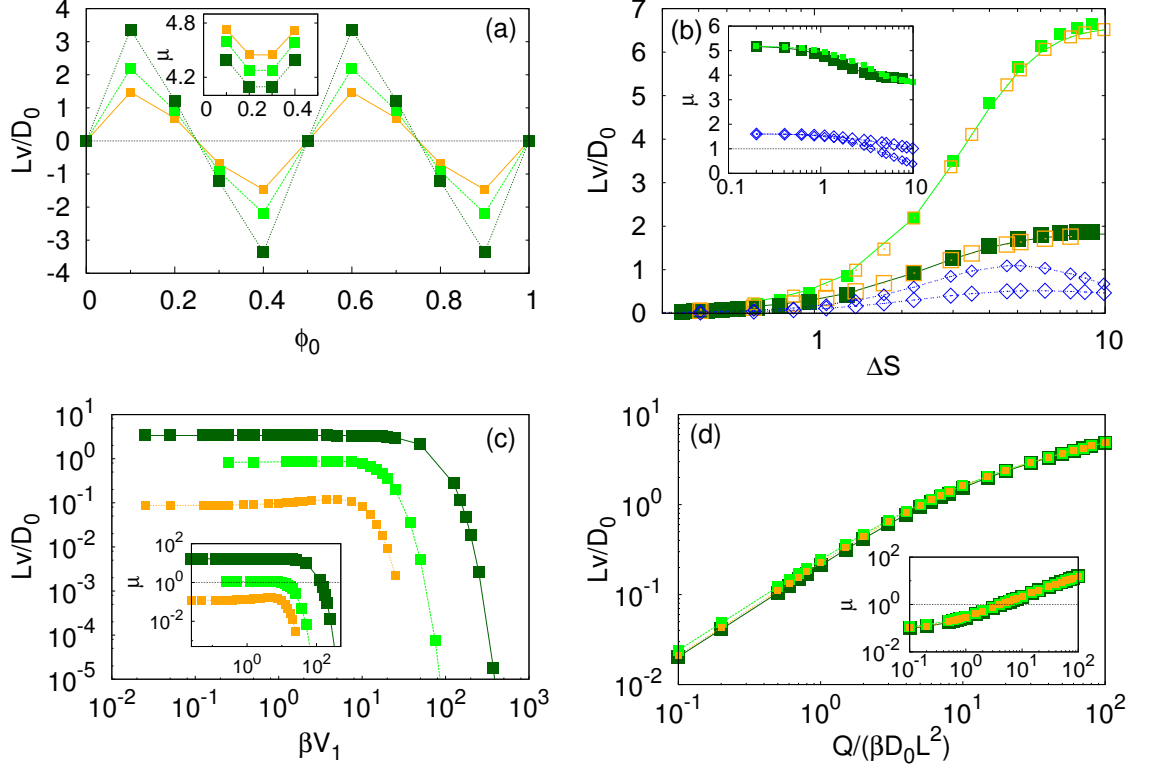
Figure 4.2: Rectification of a Brownian motor moving due to a symmetric flashing ratchet in a symmetric channel. (a): particle velocity, in units of D_0/L, being $D_0 = D_0(R = 1)$, as a function of the phase shift ϕ_0 for different values of the parameter $\Delta S = 1.73, 2.19, 2.94$ (the larger the symbol size, the larger ΔS), being $\mathcal{V}_1 = 0.2$ and $Q = 2$. Inset: μ as a function of ϕ_0 for the same parameters. (b): particle velocity as a function of ΔS upon variation of particle radius R (solid lines, with $h_0 = 1.25, h_1 = 0.2$), h_0 (solid points, with $R = 1, h_1 = 0.2$) or h_1 (open points, with $R = 1, h_0 = 1.25$) for $\phi_0 = 0.1, 0.2$ and $\mathcal{V}_1 = 0.2, Q = 2$ (the larger the symbol the larger ϕ_0). As a comparison the case with $\mathcal{V}_1 = 0.2, Q = 0.02$ and $\phi_0 = 0.1, 0.2$, (the larger the symbol the larger ϕ_0)., is shown (blue diamonds). Inset: μ as a function of ΔS for the same parameters. (c): particle velocity as a function of the ratchet potential amplitude $\mathcal{V}_1$ for $Q = 0.02, 0.2, 2$ (the larger the symbol the larger Q), while $\Delta S = 2.94, \phi_0 = 0.1$. Inset: μ as a function of ϕ_0 for the same parameters. (d): particle velocity as a function of Q for $\mathcal{V}_1 = 0.02, 0.2, 2$ and $\Delta S = 2.94, \phi_0 = 0.1$, (the larger the symbol the larger $\mathcal{V}_1$).
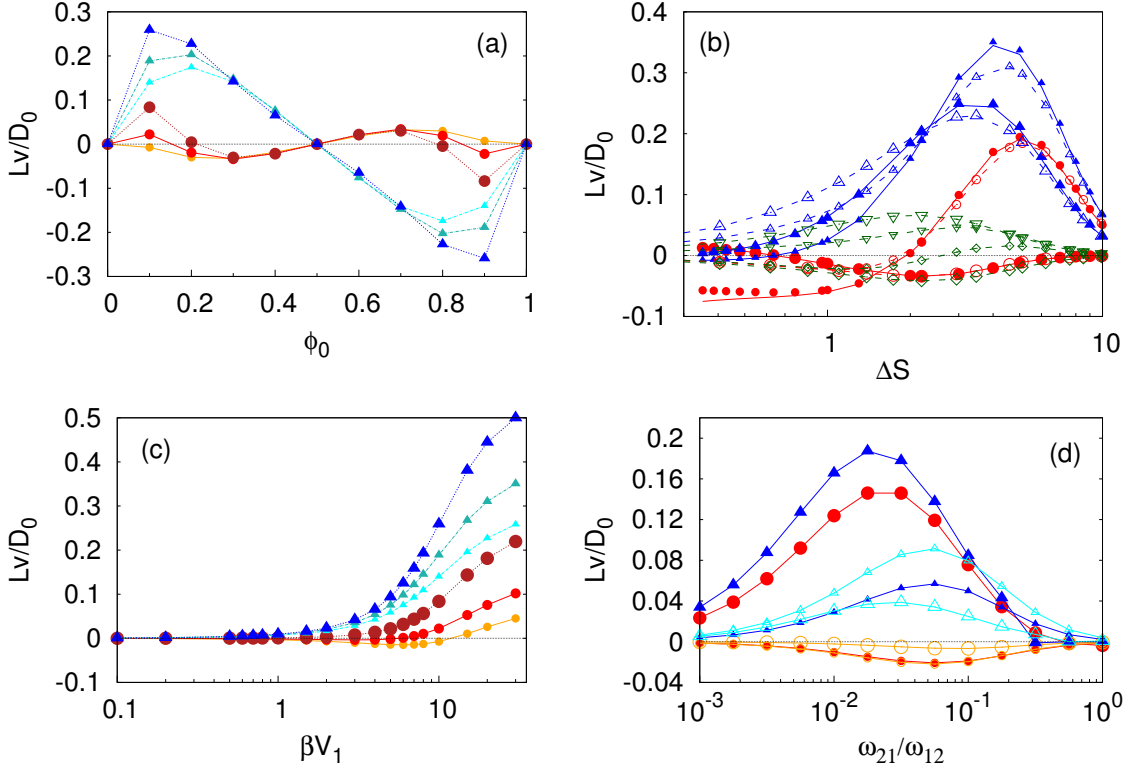
Figure 4.3: Rectification of a processive (circles), non-processive (triangles) Brownian particle moving due to the two state model in a symmetric channel. (a): particle velocity, in units of D_0/L, with $D_0 = D_0(R = 1)$, as a function of the phase shift ϕ_0 for different values of the parameter $\Delta S = 1.73, 2.19, 2.94$ (the larger the symbol size, the larger ΔS), for $\mathcal{V}_1 = 0.2$ and $\omega_{2,1}/\omega_{1,2} = 0.01$. (b): Processive (circles), non-processive (triangles) Brownian motor velocity, in units of D_0/L, as a function of ΔS upon variation of particle radius R (solid lines, for $h_0 = 1.25, h_1 = 0.2$), h_0 (solid points, for $R = 1, h_1 = 0.2$) or h_1 (open points, for $R = 1, h_0 = 1.25$) for $\phi_0 = 0.1, 0.2$(larger symbols correspond to larger ϕ_0). As a comparison, the case for $\phi_0 = 0.1, 0.2$ and $\mathcal{V}_1 = 0.2$ is shown (green diamonds) (the larger the symbol the larger ϕ_0) with $\omega_{2,1}/\omega_{1,2} = 0.01$. (The curves for $\mathcal{V}_1 = 1$ have been magnified by a factor of 5 for the sake of clarity.) (c): Processive (circles), non-processive (triangles) Brownian motor velocity as a function of the ratchet potential amplitude $\mathcal{V}_1$ for $\Delta S = 1.73, 2.19, 2.94$ (the larger the symbol the larger ΔS) with $\omega_{2,1}/\omega_{1,2} = 0.01$. (d): Processive (circles), non-processive (triangles) Brownian motor velocity, in units of D_0/L, as a function of $\omega_{1,2}/\omega_{2,1}$ for $\phi_0 = 0.1\,(0.3)$, open (solid) points and $\Delta S = 0.4, 7.6$ (the larger the symbol the larger ΔS), with $\mathcal{V}_1 = 2$.

rate variation of h_0, h_1 and R for the case of non-processive motors intensifies. These deviation from the geometrical dependence only through ΔS arise because the binding rate, $\omega_{2,1}$, depends on the probability that the motor is close to the filament, which depends indirectly on the channel section. Hence, different channel amplitudes h_0, h_1, R, even if leading to the same ΔS, give rise to different binding rates that modulate the molecular motor velocity. This sensitivity is not present for processive motors, as observed in Fig. 4.3.c.

Molecular motors show a maximum current for an optimal ΔS that depends weakly on $\mathcal{V}_1$, as displayed in Fig. 4.3.b, while Fig. 4.3.d shows that an optimum velocity, sensitive both to ϕ_0 and ΔS, can also be achieved on increasing the ratio of binding and unbinding rates, $\omega_{2,1}/\omega_{1,2}$.

4.5 Symmetric potential and asymmetric channel

The channel asymmetry wit respect to its transverse axis, $h_2 \neq 0$, breaks the left-right spatial symmetry along the channel longitudinal axis. Such an asymmetry leads to substantial changes in rectification with respect to the symmetric channel described earlier because now there exists a geometrically-induced preferential direction for particle rectification. As in the previous case, rectification here is induced by the asymmetric confinement.

Flashing ratchet   Fig. 4.4.a shows that the channel asymmetry leads to asymmetric net particle current as a function of the phase shift, ϕ_0. Non-vanishing average velocities develop even when the channel and the ratchet are in registry, $\phi_0 = 0, 1/2, 1$. Hence now a mean, non-vanishing velocity can persist for a uniform distribution of ϕ_0 as shown in the inset of Fig. 4.4.b. The average particle velocity in the case of a broader distribution of ϕ_0 is significantly reduced with respect to the values obtained for a single fixed value of ϕ_0, see fig.4.4.b. Moreover, the average velocity in the former case in not significantly affected by the channel corrugation, while the dimensionless mobility, μ, takes values comparable to those obtained in the case of a fixed ϕ_0. The channel asymmetry also enhances
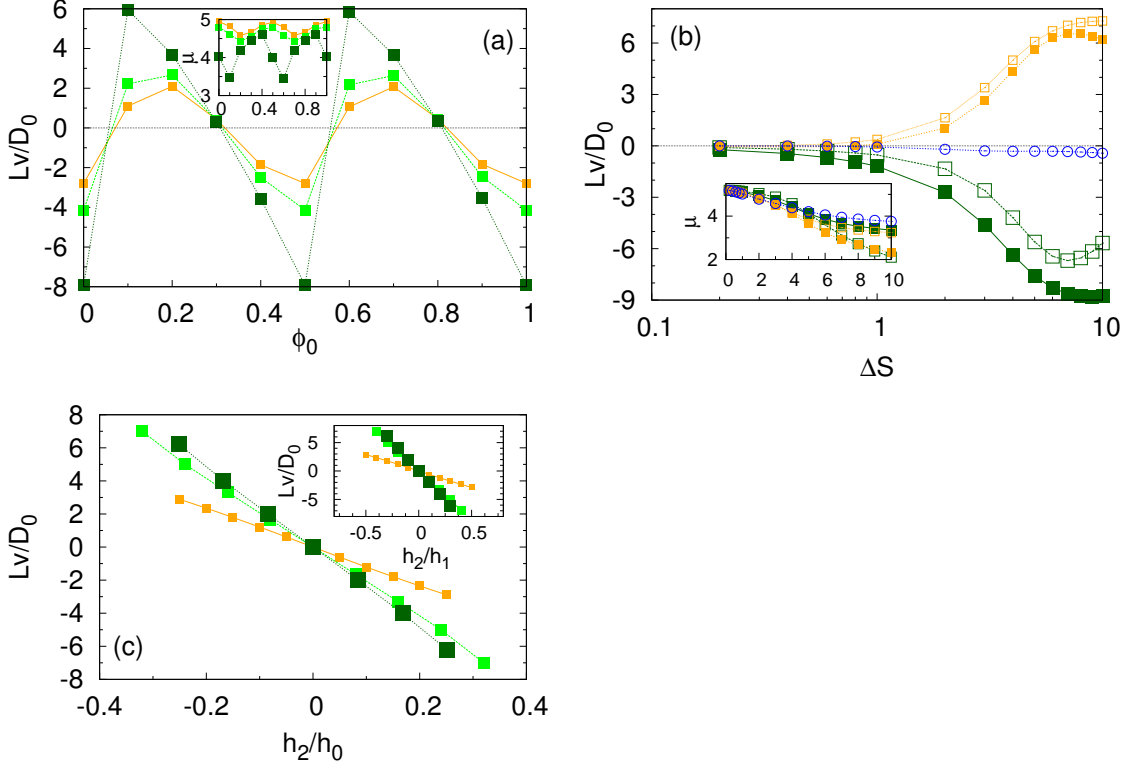
Figure 4.4: Rectification of a Brownian motor moving due to a symmetric flashing ratchet in an asymmetric channel, for $h_2/h_1 = 0.25$. (a): Particle velocity, in units of D_0/L, $D_0 = D_0(R = 1)$, as a function of the phase shift ϕ_0 for different values of the parameter $\Delta S = 0.84, 2.19, 2.94$ (the larger the symbol size, the larger ΔS), with $\mathcal{V}_1 = 0.2$ and $Q = 2$. Inset: μ as a function of ϕ_0 for the same parameters. (b): Particle velocity as a function of ΔS, varied increasing h_1 (with $R = 1, h_0 = 1.25$) at constant ratio $h_2/h_1 = 0.1$ (open points) and $h_2/h_1 = 0.25$ (solid points), for $\phi_0 = 0.1, 0.5$ and $\mathcal{V}_1 = 0.2, Q = 2$ (the larger the symbol size, the larger ϕ_0). Cyan open circles represent the average velocity obtained by a uniform distribution of ϕ_0 as a function of ΔS. Inset: μ as a function of ΔS for the same parameters. (c): Particle velocity as a function of the channel asymmetry parameter h_2, with $\phi_0 = 0$ and $\Delta S = 1.09, 2.19$ (the larger the symbol size, the larger ΔS), for $R = 1, h_0 = 1.25, \mathcal{V}_1 = 0.2, Q = 2$. Inset: μ as a function of h_2 for the same parameters.
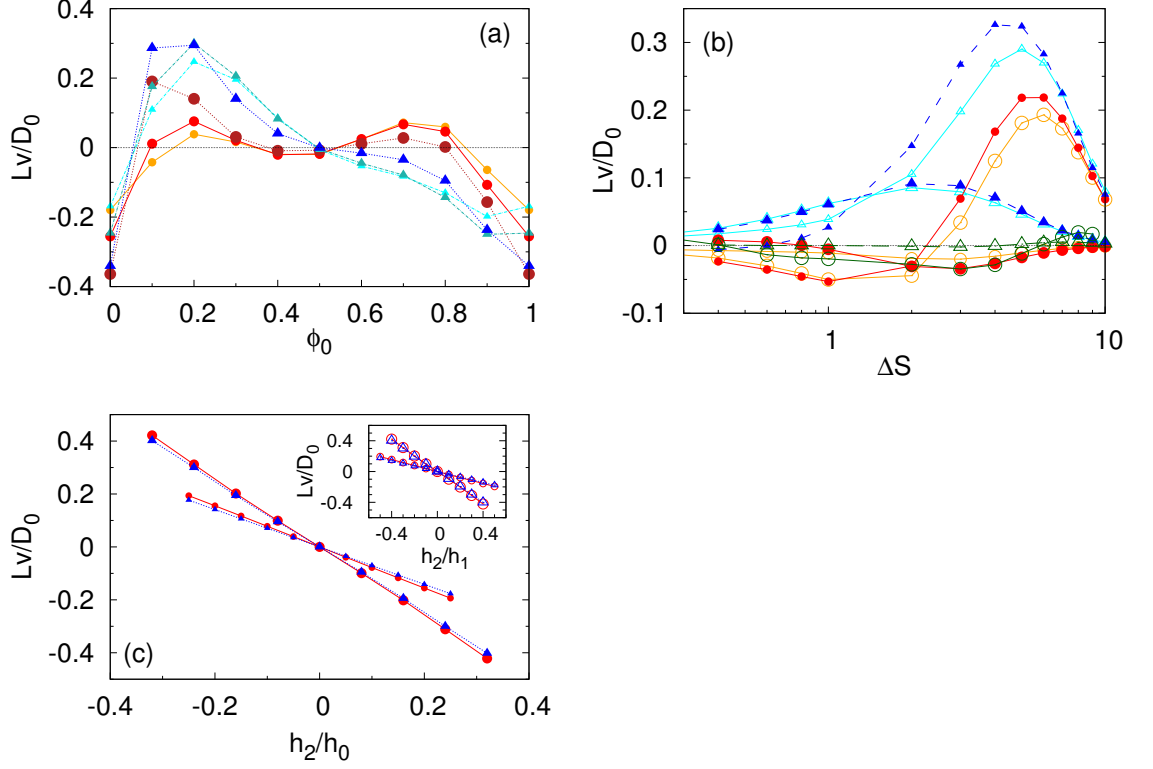
Figure 4.5: Rectification of a processive (circles), non-processive (triangles) Brownian motor moving according to the two state model in symmetric ratchet and asymmetric channel, for $h_2/h_1 = 0.25$. (a): Particle velocity, in units of D_0/L, $D_0 = D_0(R = 1)$, as a function of the phase shift ϕ_0 for different values of the parameter $\Delta S = 1.73, 2.19, 2.94$ (the larger the symbol size, the larger ΔS), with $\mathcal{V}_1 = 0.2$ and $\omega_{2,1}/\omega_{1,2} = 0.01$. (b): Processive (circles), non-processive (triangles) Brownian motor velocity, in units of D_0/L, as a function of ΔS as a function of particle radius R (solid lines, with $h_0 = 1.25, h_1 = 0.2$) or h_1 (open points, with $R = 1, h_0 = 1.25$) for $\phi_0 = 0.1, 0.4$ (the larger the symbol size, the larger ϕ_0) for $\mathcal{V}_1 = 1$ and $\omega_{2,1}/\omega_{1,2} = 0.01$. Green open circles (triangles) represent the average velocity of processive (non-processive) motors obtained by a uniform distribution of ϕ_0 as a function of ΔS. (c): processive (circles), non-processive (triangles) Brownian motor velocity as a function of h_2, being $\phi_0 = 0$, with $h_0 = 1.25, \mathcal{V}_1 = 0.2, \omega_{2,1}/\omega_{1,2} = 0.01$. The larger the symbol size, the larger the value of h_1 ($h_1 = 0.125, 0.2$).

the rectifying velocity magnitude, which is almost two fold larger than the one obtained for the symmetric channel (Fig. 4.2.a). The net velocity also shows a strong dependence on the channel asymmetry, ΔS. The insets of Fig. 4.4 show that $\mu > 1$ for all regimes considered, underlying the strong cooperative regime between the symmetric ratchet and the geometric confinement. Finally, we observe a linear dependence of the particle velocity upon increasing h_2 at fixed h_1. As also shown in fig. 4.4.b, the slope of the linear relation between h_2 and $\bar{v}$ depends on ΔS: increasing the entropic barrier leads to a steeper slope.

Two-state model   As for the flashing ratchet, the channel asymmetry leads to an asymmetric velocity profile upon variation of ϕ_0, as shown in Fig. 4.5.a. In particular, we notice that for $\phi_0 = 0$ the net velocity of processive or non-processive motors are very similar as ΔS varies (fig. 4.3.a). The asymmetric channel profile leads to an overall non vanishing flux when averaged over the, equally weighted, values of ϕ_0. Hence, as for the flashing ratchet, we expect the channel asymmetry to provide the onset of net currents even in the case of a broader distribution of phase shifts ϕ_0. The dependence of the particle velocity on ΔS, shown in fig. 4.5.b, is similar to the one obtained for the symmetric channel, fig. 4.3.b, where an optimal value of ΔS is observed for both processive and non processive motors. As in the symmetric configuration, the dependence of motors' velocity on the different geometric parameters (h_1 and R) is quite well captured by the entropic barrier ΔS, although a separate sensitivity on h_1 and R persists for both processive and non-processive motors. Particle current depends linearly on h_2, as shown in fig. 4.5.c. increasing the slope for larger values of ΔS.

4.6   Asymmetric potential and symmetric channel

An asymmetric ratchet potential, $\lambda \neq 0$, in the presence of a symmetric periodic channel, $h_2 = 0$, allows us to address the impact that an inhomogeneous environment has on an intrinsically rectifying Brownian ratchet. In particular, cooperative rectification modulates the particle velocity allowing for the emer-

gence of effective particle fluxes opposing the direction of motion of the intrinsic Brownian ratchet.

Flashing ratchet   Fig. 4.6.a shows that the intrinsic Brownian ratchet net velocity, v_0, is strongly modulated by the channel corrugation. CBR in this case can exhibit both regimes where the average velocities exceed v_0, showing strong velocity enhancements, as well as conditions where the velocity changes sign, indicating confinement-induced flow reversal. In the latter case, particles moving against the direction imposed by the ratchet can display speeds larger than v_0. As in the case of symmetric ratchet, these effects are magnified when rising the entropy barrier ΔS, as shown in Fig. 4.6.b. In the presence of flux reversal, geometrical confinement leads to a mechanism for particle separation based on their size because ΔS depends both on the channel geometry and the particle size. As shown in fig. 4.6.b, modulating particles size one can control and switch their velocities, offering new venues to manipulate particles and even trap them. The average particle current obtained in a disordered channel, i.e. with a uniform distribution of ϕ_0, is not significantly affected by the geometrical constraint.

The absolute value of particle current (not shown) is also very sensitive to $\mathcal{V}_1$ and Q , analogously to the results obtained for the symmetric channel (Fig. 4.2.c-4.2.d). Figs. 4.6.c-4.6.d display strong enhancements of the net particle velocity, up to two orders of magnitude larger than v_0. These large enhancements are observed when $\mathcal{V}_1/\Delta S \ll 1$, indicating that cooperativity relies mostly on the interplay between the geometrical confinement and the position-dependent noise amplitude rather than on the asymmetric potential $V(x)$ itself.

Since the Brownian ratchet is characterized by an intrinsic rectifying velocity, v_0, it is useful to study the ratio μ/μ_0 in order to quantify the relative variation in the mobility of a CBR due to the geometrical constraints. In Figs. 4.6.a-4.6.b $\mu_0 = 6.1$, hence the system takes advantage of the x-dependent free energy gradient induced by the intrinsic ratchet mechanism. The dependence of μ on $\mathcal{V}_1$ and Q is quite similar to the one observed in symmetric channels (Fig. 4.2): larger values of the mobility are observeed for small and moderate values of $\mathcal{V}_1$ and mild and large values of Q, while for larger values of $\mathcal{V}_1$ μ drops. On the contrary, μ/μ_0 increases monotonously with $\mathcal{V}_1$ irrespectively of Q, while the dependence
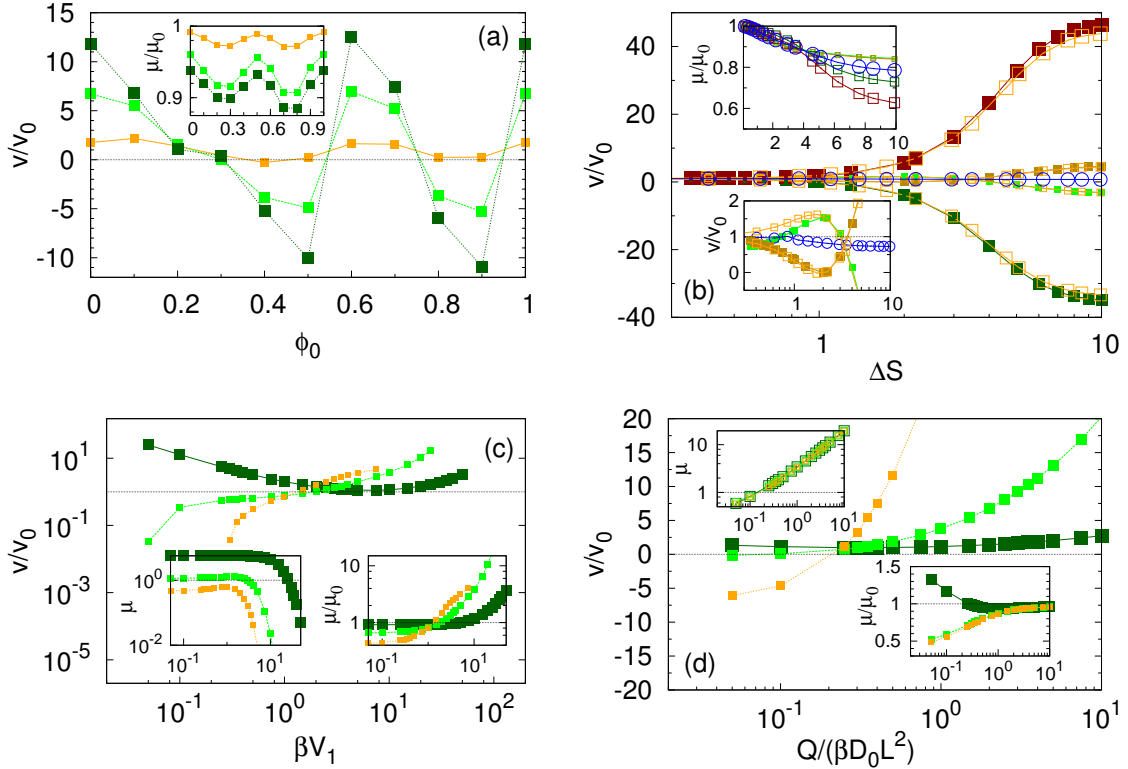
Figure 4.6: Rectification of a Brownian motor moving due to a asymmetric flashing ratchet in symmetric channel. (a): particle velocity, in units of v_0, for $\Delta S = 0$, as a function of the phase shift ϕ_0 for different values of the parameter $\Delta S = 0.84, 2.19, 2.94$ (the larger the symbol size, the larger ΔS), for $\mathcal{V}_1 = 0.2$ and $Q = 2$. Inset: μ, in units of the dimensionless mobility, μ_0, as a function of ϕ_0 for the same parameters. (b): particle velocity as a function of ΔS as a function of particle radius R (solid lines, with $h_1 = 1.25, h_2 = 0.2$), h_1 (solid points, with $R = 1, h_2 = 0.2$) or h_2 (open points, with $R = 1, h_1 = 1.25$) for $\phi_0 = 0.2, 0.3, 0.5, 0.6$ and $\mathcal{V}_1 = 0.2, Q = 2$ (the larger the symbol size, the larger ϕ_0). Cyan open circles represent the average velocity obtained by a uniform distribution of ϕ_0 as a function of ΔS. Inset: μ/μ_0 as a function of ϕ_0 for the same parameters. (c): particle velocity as a function of the ratchet potential amplitude, $\mathcal{V}_1$, for $Q = 0.02, 0.2, 2$ (the larger the symbol size, the larger Q), for $\Delta S = 2.94, \phi_0 = 0.1$. Insets: μ and μ/μ_0 as a function of ϕ_0 for the same parameters. (d): particle velocity as a function of Q. Squares for $\mathcal{V}_1 = 0.1, 1, 10$ and $\Delta S = 2.94, \phi_0 = 0.1$, (the larger the symbol size, the larger $\mathcal{V}_1$); triangles: $Q = 1, \Delta S = 1.1, \phi_0 = 0.5$ and $\mathcal{V}_1 = 1$. Insets: μ and μ/μ_0 as a function of ϕ_0 for the same parameters.
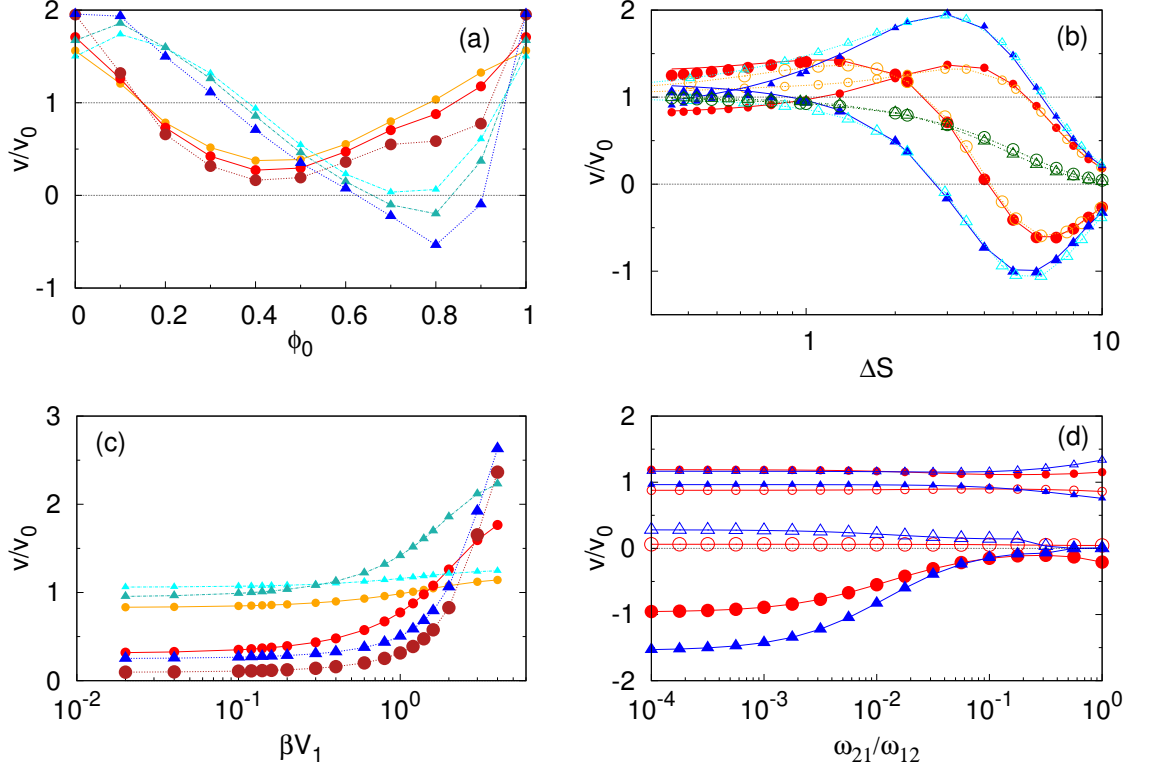
Figure 4.7: Rectification of a processive (circles), non-processive (triangles) Brownian motor moving due to the two state model in symmetric channel. (a): particle velocity, in units of v_0 as a function of the phase shift ϕ_0 for different values of the parameter $\Delta S = 1.73, 2.19, 2.94$ (the larger the symbol size, the larger ΔS), for $\Delta V_1 = 0.2$ and $\omega_{2,1}/\omega_{1,2} = 0.01$. (b): processive (circles), non-processive (triangles) Brownian motor velocity, in units of D_0/L, as a function of ΔS and particle radius R (solid lines, with $h_0 = 1.25, h_1 = 0.2$), h_0 (solid points, with $R = 1, h_1 = 0.2$) or h_1 (open points, with $R = 1, h_0 = 1.25$) for $\phi_0 = 0.1, 0.9$ (the larger the symbol size, the larger ϕ_0) for $\mathcal{V}_1 = 1$ and $\omega_{2,1}/\omega_{1,2} = 0.01$. Green open circles (triangles) represent the average velocity of processive (non-processive) motors obtained by a uniform distribution of ϕ_0 as a function of ΔS. (c): processive (circles), non-processive (triangles) Brownian motor velocity as a function of the ratchet potential amplitude $\mathcal{V}_1$ for $\Delta S = 0.4, 2, 7.6$ (the larger the symbol size, the larger ΔS) with $\omega_{2,1}/\omega_{1,2} = 0.01$. (d): processive (circles), non-processive (triangles) Brownian motor velocity as a function of $\omega_{1,2}/\omega_{2,1}$ for $\phi_0 = 0.1, 0.3$, open (solid) points and $\Delta S = 0.4, 7.6$(the larger the symbol size, the larger ΔS) for $\mathcal{V}_1 = 10$.

on Q at fixed $\mathcal{V}$ is more involved as shown in fig. 4.6.d.

Two state model   Fig. 4.7.a displays the net velocity as a function of the dephasing between the geometric confinement and the underlying ratchet potential. Cooperative rectification now shows a strong dependence on the phase shift, ϕ_0, leading to large velocity amplification and also to flux reversal, a feature that was not possible for symmetric channels. In fact, both processive and non-processive motors show velocity enhancement and reversal when varying the channel corrugation, ΔS, as shown in Fig. 4.7.b. Hence, even symmetric channels offer the possibility to control molecular motor motion according to their size, allowing for segregation and particle trapping. Interestingly, for asymmetric ratchets the entropic barrier ΔS captures even better the dynamics, as compared to the case of symmetric ratchets, and only at smaller ΔS the different behavior upon variation of h_0, h_1 and R becomes appreciable. Looking at the velocity dependence as a function of $\mathcal{V}_1$, shown in fig. 4.7.c, we find a behavior similar to the one obtained for the symmetric ratchet. On the contrary, the velocity dependence upon variation of ω_{21}/ω_{12}, shown in fig. 4.7.d, is very mild for smaller ΔS while for larger ΔS velocity inversion happens for smaller values of ω_{21}/ω_{12}.

4.7   Fully Asymmetric case

When both the ratchet as well the channel left-right symmetry are broken, $\lambda \neq 0$ and $h_2 \neq 0$, all the features we have discussed previously are now present. Rather than attempting a systematic analysis of the performance of CBR in this regime, that is very rich, we will point out the basic differences with the previous cases.

Flashing ratchet   As shown in Fig. 4.8.a, the asymmetry in both channel shape and ratchet potential leads to non-intuitive velocity variations with ϕ_0; one can identify a velocity enhancement/reduction as well as velocity inversion as a function of ϕ_0. Moreover, different values of ΔS strongly modulate the velocity dependence on ϕ_0 as shown in fig. 4.8.a. Looking at the dependence of the velocity on ΔS, fig. 4.8.b, we observe a strong non-monotonic response where the motor velocity, initially enhanced, is reduced by increasing ΔS until it is inverted for
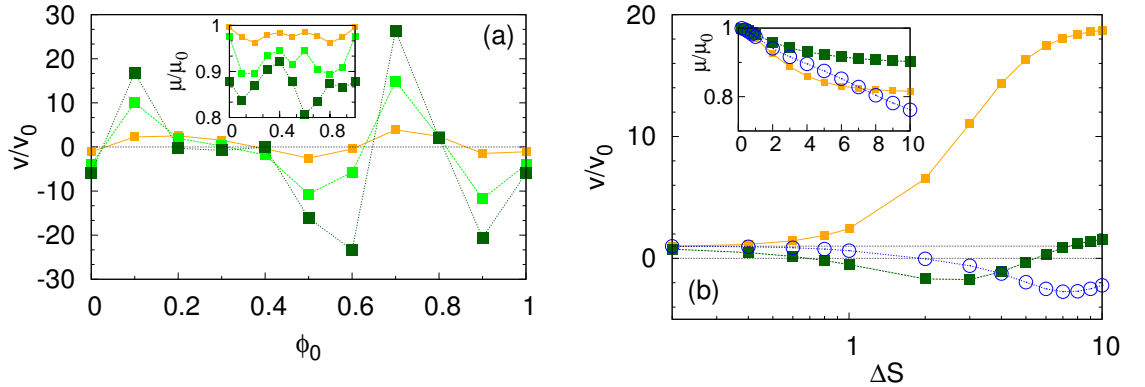
Figure 4.8: Rectification of a Brownian motor moving according to an asymmetric flashing ratchet in an asymmetric channel. (a): particle velocity, in units of the velocity,v_0, provided by the ratchet for $\Delta S = 0$, as a function of the phase shift ϕ_0 for different values of the parameter $\Delta S = 0.84, 2.19, 2.94$ (the larger the symbol size, the larger ΔS), for $\mathcal{V}_1 = 0.2$, $h_2/h_1 = 0.25$ and $Q = 2$. Inset: μ, in units of the dimensionless mobility μ_0 as a function of ϕ_0 for the same parameters. (b): particle velocity as a function of ΔS and h_1 (with $R = 1, h_0 = 0.25$) for $\phi_0 = 0.1, 0.4$, $h_2/h_1 = 0.25$ and $\mathcal{V}_1 = 0.2, Q = 2$ (the larger the symbol size, the larger ϕ_0). Cyan open circles represent the average velocity obtained by a uniform distribution of ϕ_0 as a function of ΔS. Inset: μ/μ_0 as a function of ϕ_0 for the same parameters.

larger values of ΔS. As in the previous cases, we find a wide range of values of μ as well as of μ/μ_0 underlying that the sensitivity of CBRs in this scenario as a function of the changes in the geometrical constraints and ratchet parameters.

Two state model   As for the flashing ratchet case, the presence of both channel and ratchet asymmetries leads to a non trivial velocity profile upon variation of ϕ_0. Again we find here the presence of velocity enhancement, reduction or even inversion, see fig. 4.9.a. Surprisingly, the velocity dependence on ΔS reminds the one obtained in the case of asymmetric ratchet in a symmetric channel. The entropic barrier, ΔS, captures the essential response of the confined molecular motors, even better than in the cases for which the ratchet is symmetric. Finally, also the net motors flux in a disordered channel, i.e. with equally distributed ϕ_0, has a behavior similar to the one obtained in the case of symmetric channel.
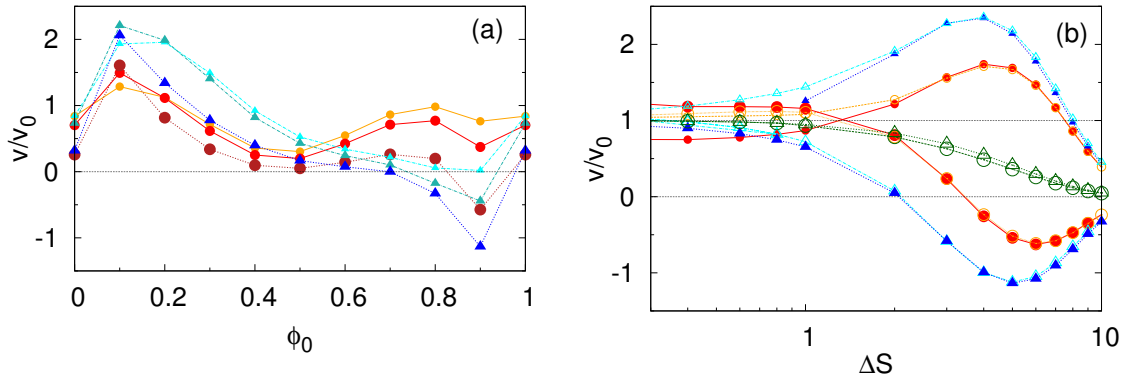
Figure 4.9: Rectification of a processive (circles), non-processive (triangles) Brownian motor moving due to the two state model in an asymmetric channel. (a): particle velocity, in units of v_0, for $\Delta S = 0$, as a function of the phase shift ϕ_0 for different values of the parameter $\Delta S = 1.73, 2.19, 2.94$ (the larger the symbol size, the larger ΔS), for $\Delta V_1 = 0.2$, $h_2/h_1 = 0.25$ and $\omega_{2,1}/\omega_{1,2} = 0.01$. (b): processive (circles), non-processive (triangles) Brownian motor velocity, in units of D_0/L, as a function of ΔS and particle radius R (solid lines, with $h_0 = 1.25, h_1 = 0.2, H_2/h_1 = 0.25$) or h_1 (open points, with $R = 1, h_1 = 1.25, h_2/h_1 = 0.25$) for $\phi_0 = 0.1, 0.9$ (the larger the symbol size, the larger ϕ_0) for $\mathcal{V}_1 = 1$ and $\omega_{2,1}/\omega_{1,2} = 0.01$. Green open circles (triangles) represent the average velocity of processive (non-processive) motors obtained by a uniform distribution of ϕ_0 as a function of ΔS.

4.8   Conclusions

We have analyzed the motion of Brownian ratchets in confined media. We have shown that the interplay between the intrinsic ratchet motion and the geometrically-induced rectification gives rise to a variety of dynamical behaviors not observed in the absence of the geometrical confinement. A novel effect, named cooperative rectification, arises as the net result of the overlap between the dynamic induced by the ratchet and the confinement and it is responsible for the onset of net currents even when neither the ratchet nor the geometrical constraint can rectify per se. The dynamics of the particles can be analyzed by means of the Fick-Jacobs equation. Such an approach has allowed to identify two parameters, namely the entropic barrier ΔS an the free energy drop ΔF, that govern the overall dynamics of CBRs. On one hand, ΔF controls the onset of the cooperative rectification when $\Delta F \neq 0$. Then, cooperative rectification leads to a net current whose sign is determined by ΔF. On the other hand, ΔS accounts for the relevance of confinement in the overall dynamics when $\Delta S \neq 0$.

We have discussed when entropic confinement affects the rectification of a Brownian ratchet by contrasting physically different ratchet mechanisms. In particular, in the analysis of Brownian rectification induced by an inhomogeneous temperature profile we have clarified the relevance of the underlying mechanism breaking detailed balance. For a flashing ratchet the second moment of the longitudinal velocity of a CBR differs from the second moment associated to its transverse velocity while such an intrinsic anisotropy is lacking for the thermal ratchet. As a result, confined thermal ratchets can rectify only if there is an interplay between the asymmetric enthalpic potential and temperature gradients.

Comparing the cases of a flashing ratchet and a two-state model of a molecular motor we conclude that the novel mechanism we describe is qualitatively robust with respect to the details of the Brownian ratchet. However, the specificity of the rectification can affect both the quantitative response of a Brownian ratchet to confinement and, in some cases, even affect the qualitative behavior observed; e.g. velocity inversion can be observed increasing ΔS for processive molecular motors in a symmetric channel while velocity inversion is never observed for non-processive motors. The Fick-Jacobs approach has provided insight to understand

these qualitative differences.

We have always assumed that the confining channel and the ratchet potential have the same period. If both components have different periodicities, or if one of them show irregularities (that can emerge, for example, from experimental defects in the channel build up), one can still account for the mismatch between the ratchet potential and the channel corrugation by considering that the phase shift ϕ_0, rather than having a well defined value, is characterized by a uniform distribution. The results reported show that, in this situation a net current persists except for the fully symmetric geometry.

For asymmetric, intrinsically rectifying ratchets, we have seen that CBRs are very sensitive to corrugation and that the geometrical constraints strongly affect their motion. Controlling the corrugation of the channel one can enhance significantly the net Brownian ratchet velocity or can induce velocity inversion for all the Brownian ratchet models considered. Therefore, confinement provides a means to control particle motion at small scales. Since particles with different sizes show a differential sensitivity to the geometrical constraints, it is possible to use channel corrugation to segregate Brownian ratchets of different sizes, or even trap particles. Therefore, CBRs offer new venues to particle control at small scales.

4. CONFINEMENT-INDUCED RECTIFICATION

5. Conclusions and perspectives

The aim of this thesis has been the characterization of the interplay between molecular motors internal dynamics and the environment motors move in. In particular we have characterized two different scenarios for which the local properties of the fluid significantly affect the overall motors dynamics.

As a first scenario we studied the case of several molecular motors walking along a common filament. While displacing, molecular motors generate local fluid fluxes that affect the local velocity of the fluid. As a result, the intrinsic dynamics of molecular motors is affected by the displacement of nearby motors leading to a hydrodynamic coupling between motors. We have characterized the hydrodynamic coupling between molecular motors in two different scenarios. On one hand we have found that the hydrodynamic coupling between motors provided by the fluid can strongly affect the overall motor velocity. Local variations in motor density, due to thermal fluctuation, might grow up and lead to the formation of clusters that, as an outcome, speed up the velocity of the motors leading to the onset of stable structures. On the other hand, when several motors are pulling on a membraine enveloped common cargo, the liquid nature of the membrane provide an alternative mean to couple motors. In this scenario we have seen that the hydrodynamic coupling between motors pulling on opposite directions can lead to symmetry breaking as well to bistability even for system sizes comparable to relevant biological situations, hence allowing for an alternative mean to control cargo dynamics.

As a second scenario we studied the dynamics of a single motor moving in an intrinsically inhomogeneous fluid where, the heterogeneity in the fluid is induced by the presence of geometrical confinements. In fact, if the local available space is modulated, additional forces of entropic nature arise. The interplay between the

5. CONCLUSIONS AND PERSPECTIVES

stepping motion of the motor and such a modulation can lead to novel dynamical regime unreachable for particles under constant forces or molecular motors displacing in an homogeneous environment.

This study points out two main results. On one hand the step-like nature of molecular motors makes them particularly suited for the onset of collective behavior. The presence of different length and time scales in their single-particle displacement give rise to novel collective behavior absent for particles pulled by constant forces. In particular we have shown that when molecular motors can switch between a strong and weakly bound state, as it has been observed for KIF1A [74], single-headed Myosin VI [47], Kinesin-8 [49], Kinesin-1 [60], cytoplasmic Dynein [5; 88; 94], microtubule cross-shifting motor Eg5 [52; 95] and non-processive Myosin XI[7], their collective behavior can be strongly affected by motor-motor interactions. As a confirmation of this statement, more processive motors, hence always strongly bound to the filament, such as conventional Kinesin or Myosin V do not display such an intriguing collective behavior, at least when they are rigidly coupled[58; 82]. In fact, motility assay experiments [82] as well gliding assay [58] have not observed velocity speed up of rigidly coupled motors. Therefore it seems that motors that, when displacing alone, are more performing, such as conventional Kinesin or Myosin V, are less suited to be tuned by collective interactions. On the contrary, less performant motors, such as KIF1A, single-headed Myosin VI and even more non-processive Myosin XI might lead to more intriguing collective behavior.

The second main result coming from this study deals with the properties of the environment. When the environment is intrinsically inhomogeneous, as is for motors displacing under geometrical constraints, or the environment state varies locally, as is the velocity profile induced in the fluid by molecular motors, the overall motor dynamics strongly deviates from that of a single motor displacing in an homogeneous environment. Therefore, the transport performance of motors in in-vivo situations can strongly be affected by the environment conditions. As we have seen in chapter 2, variations in the fluid effective viscosity due to modulation in the density of suspended particles can lead to different transport regimes along filaments. On the other hand suspended particles will modulate locally the transport coefficients hence affecting the internal mechano-chemical

dynamics of motors.

All in all the environment properties affect intracellular transport. Both hydrodynamic coupling as well intrinsic inhomogeneities, such as those induced by geometrical confinement, can open new routes to control intracellular transport. Such an additional control might be relevant for the onset of diseases caused by alteration in the intracellular trafficking such as Alzheimer or Charcot-Marie-Tooth [33; 34; 43].

In the following we will resume the conclusions chapter by chapter as we will also discuss some possible future works.

5.1   Hydrodynamically-coupled molecular motors

In the first chapter we have analyzed the collective behavior of several motors walking in the same direction along a common filament. We have observed a non linear relation between the density of the motors on the filament and the overall displacing velocity. This coupling leads to mean velocities up to two orders of magnitude larger than the mean velocity of isolated motors. Such a huge speed up relies on the stepping nature of molecular motors trajectories. In fact, particles under constant force does not undergo such a huge speed upTherefore, our results show that the stepping nature of molecular motors allow for a new route to control motors ensembles velocity.

In particular hydrodynamic coupling will lead to huge speed up for those motors switching between $1D$ diffusion along filaments and stepping as it has been observed for processive motors like KIF1A [74], single-headed Myosin VI [47], Kinesin-8 [49], Kinesin-1 [60], cytoplasmic Dynein [5; 88; 94] and microtubule cross-shifting motor Eg5 [52; 95].

Kinesins and Dyneins both walk along microtubules on opposite directions at the same time. The presence of motors displacing in opposite directions, like Kinesins and Dyneins on microtubules, can lead to different dynamical scenarios. Local clusters of Kinesins or Dyneins are likely to occur due to fluctuation in the local motor density and can be stabilized the, local, hydrodynamic coupling. In this view, it would be interesting to study how the onset of these local structures

5. CONCLUSIONS AND PERSPECTIVES

affects the overall transport along microtubules. In particular the long-range hydrodynamic coupling between motors might lead to a spatial organization of the microtubule into lanes characterized by a large density of Kinesins/Dyneins hence enhancing the overall transport along microtubules.

Other motors like Myosin V [97] or microtubule-ends depolymerizing motors MKAC [42] as well many microtubule binding proteins[24] and synthetic charged beads [68] undergo $1D$ diffusion along microtubules. The presence of passive particles weakly bound to the microtubule affects the propagation of the momentum through the fluid and so the coupling between motors. Therefore, it would be interesting to study how the presence of passive particles weakly bound to the microtubule affect the overall motor dynamics.

Molecular motors are pulling on cargoes while displacing along filaments. If we disregard the internal dynamics of motors tail linking motors active site with the cargo, we can regard our results as the overall displacement of identical cargoes each of which pulled by a single motor. In this framework it would be interesting to relax the constraint on the cargo size and study the case of a more disperse distribution of cargo sizes pulled by several motors. Such an extension will introduce heterogeneities in the system that might trigger the onset of novel dynamical regimes. For example, polydisperse cargoes will lead to an additional heterogeneity in the onset of hydrodynamic coupling between motors since larger and smaller cargoes will affect each other in different ways. The distribution of the size of cargoes transported along a common filament might affect transport properties according to their size. For example, smaller cargoes can benefit from the flux generated by larger cargoes, or, on the contrary, the larger cargoes might act as obstacles for smaller cargoes. Alternatively heterogeneities in the number of pulling motors per cargo will lead to faster and slower cargoes that can promote the onset of larger clusters as it has been observed for sliders [96]. Therefore it would be interesting to study the possibility of a size- and/or motors number-dependent control of the transport properties of cargoes of different size and/or pulled by different motors teams.

Suspended particles distribution is affected by gradients in the velocity profile [91]. Since our results show that the presence of suspended particles enhances the onset of larger velocity gradients, it would be interesting to study how a

polydisperse suspension of particles will be affected by such a velocity profile and, vice-versa, how the new distribution of suspended particles will affect motor dynamics.

Up to know we have dealt with a cylindrical geometry. However, in many plant cells the cytoplasmic streaming occurs in the thin layer of cytoplasm embedded between cell membrane and the central vacuole that occupy almost the $\sim 90\%$ of the cell volume. An ongoing project in collaboration with Prof. D. Marenduzzo and Dr. K. Wolff aims to characterize the dynamics of motors on sheets of filaments. In such a geometry we have already observed the formation of clusters that, by percolating along the transverse direction form band-like structures. It would be interesting to characterize the stability of these structures as well as the net transport of motors and suspended particles. Such a characterization can provide insight on the organization of motors and cargoes in plant cells as well it will provide a characterization for a realization of biomimetic microfluidic devices.

For more isotropic geometries, is more isotropic, as it happens in animal cells, the onset of macroscopic fluxes is hampered and only local fluxes will be induced by pulling motors. For such configuration it would be interesting to study how the local flux surrounding each filament affect the transport of suspended particles. Recent works have already characterized the dynamics of motors on a network of filaments [72; 73] In particular, when filaments intersect rearrangements in suspended particle density might occur according to the geometry of the fluxes. Therefore, centrosomes or other microtubule polymerizing organelles might experience a depletion or accumulation of suspended particles according to the arrangement of the biofilaments that possibly can affect their dynamics.

5.2 Bidirectional transport

In the second chapter we have characterized the role of the hydrodynamic coupling between oppositely displacing motors pulling on a common cargo. We have observed that spontaneous symmetry breaking can occur due to the hydrodynamic coupling for large enough system sizes. In particular, the minimum size at

5. CONCLUSIONS AND PERSPECTIVES

which symmetry breaking occurs depends on the kind of coupling: if the ratio of the cytoplasm and membrane viscosity is large enough then the coupling induced by the membrane will be dominant and symmetry breaking will occur for smaller system sizes, while larger system sizes are required if the coupling is mainly provided by the cytoplasm. Our analysis has identified the local reorganization of motors density as the most relevant ingredient in leading to those regimes, such as bistability, absent for rigidly coupled motors.

In order to perform our analysis we have done some approximations that allowed us to grasp the underlying dynamics without the need of more intense numerical efforts. Our main approximations consist in assuming the dynamics to be local, i.e. not affectd by the boundary conditions and, by exploiting this idea, to assume the hydrodynamic coupling to be equal for all motors. While we are quite confident that the underlying dynamics we have described is robust, relaxing those hypothesis can lead to novel dynamical regime we haven't explored yet.

First of all, relaxing the periodic boundary condition will allow us to study the influence of the edges of motors ensemble on the overall dynamics. If the motor density is smoothly varying on length scales larger than the period of the potential but smaller than the size of the ensemble we can perform the master equation expansion on these larger regions in order to capture, still in a coarse-grained way, the role of density inhomogeneities on length scales of the order of the system size. Since motors on the edges will experience a different collective force that those in the bulk, density reorganization can be driven by such an heterogeneous collective force leading to motor structures. In particular, we expect such structures to happen at the boundaries of motors ensembles where the collective hydrodynamics force is weaker. The onset of such structures can prevent the onset of the bistable regime and can stabilize the direction of average displacement. Again such a behavior will be typical of hydrodynamically coupled motors as compared to the rigid case. Moreover, such accumulations have already been observed experimentally due to the non homogeneous load motors experience along the cargo [12; 17; 18]. It has been shown that motors at tip of the cargo will experience a larger force than motors in the bulk leading to clustering at the edge of the cargo. In this view it would be interesting to study how the flux

generated by motors in the bulk affect the dynamics at the tip. We can extend the present framework to the case of motors extracting membrane tubes out of Giant Vesicles. Recently, it has bee claimed [84] that also non-processive motors can perform such a task. Since for non-processive motors the hydrodynamic coupling is expected to quite relevant, as we discussed in chapter 4, then it would be interesting to analyze how the flux generated by motors along the membrane affect the dynamics at the tip.

Secondly, it would be interesting to study two distinct teams of motors localized at the two ends of the cargo and pulling on opposite direction. This additional heterogeneity in the local forcing will affect the overall collective effect. In this case we will have an overlap of the heterogeneity in the collective force coming from the position of the motors with respect to cargo's edges and that provided by the localization of teams pulling on opposite directions. Moreover, since motors can unbind more probably when they are under the action of a load, the overall dynamics can be even affected by the load dependent unbinding rate.

The membrane in which cargoes are enveloped is a closed sheet of fluid. Then, mass conservation and the incompressibility of the membrane provide a strong constraint that prevent the onset of net averaged fluxes along the membrane. Therefore, the flux generated by pulling motors should be compensated by a backward propagating flux ensuring a vanishing total flux. Recently, the interaction between two dislocation on a $2D$ cylindrical lattice have been characterized showing the analogy to third sound waves and to liquid Helium transport properties [4; 71]. Therefore, it would be interesting to characterize the hydrodynamic coupling between molecular motors pulling on membranes. Due to the $2D$ nature of the coupling jointly with the constraint of vanishing average flux quite different dynamical regimes can show up.

5.3   Confinement-induced rectification

In the third chapter, we have characterized the interplay between the out of equilibrium state of a molecular motor, or more in general of a Brownian ratchet,

5. CONCLUSIONS AND PERSPECTIVES

and the geometrical confinement the motor is exposed to. In our analysis, we have shown that the interplay between the two rectifying mechanism strongly affect the overall dynamics leading to dynamical regime unapproachable by the two mechanisms separately. For example, cooperative rectification develops even for cases in which the ratchet and the geometrical confinement would not lead to any current per se. Moreover, even for rectifying Brownian ratchets, their current can be enhanced, reduced or even inverted by the presence of entropic barriers. Finally we have shown that such dynamical regimes are strongly affected by particle size opening the possibility of an alternative mechanism for particle separation at the micro- nano-scale.

In order to simplify our analysis and gain insight in the underlying dynamics we have exploited periodic boundary conditions. However, for real systems, this might not be the case. For example, the thickness of dendrites has been found to shrink as the distance from the nucleus increases [10]. On the other hand melanophores, that are responsible for the melanin control, have a radial organization of microtubules that allow for a rapid concentration/dispersion of melanin inside the cell. For those situations it would be interesting to study how the geometrical confinement affect the overall dynamics.

In particular, for dendrites, whose cylindrical overall shape reminds the study performed in the first chapter, it would be interesting to study how the varying section of the dendrite affects the onset of the collective behavior and the cytoplasmic streaming discussed in the first chapter. The shrinking of the dendrite on one hand will induced larger velocity gradients along the radial direction, hence enhancing dissipation. Suspended particles will be affected by the reduction in the section. As we have discussed in the first chapter the overall dynamics of motors on filaments can be strongly affected by the density of suspended particles. Moreover, such an effect is particularly relevant for motors that can diffuse along microtubules while in a weak-bound state as it happens for synaptic precursors transporter KIF1A that is involved in cargo transport in neurons.

In the case of melanophores, the radial distribution of microtubules strongly affects the dynamics of cargoes transported along microtubules. Recent experiments have shown that the transport properties of cargoes pulled away or towards the cell nucleus are quite different. In this case the radial geometry probably pre-

vents the onset of net fluxes as characterized in the first chapter. Therefore, in this case the increasing distances between nearby microtubules can induces entropically-driven transport properties relying on mechanisms similar to those shown in the last chapter. Moreover, the network of actin and intermediate filaments have been shown to play a relevant role in determining the overall transport properties. Since cargoes can move on both microtubules and actin filaments, then it would be interesting to study how this asymmetric network of filaments each of which characterized by different transport properties and/or polarity can affect the overall transport of cargoes covered by both Kinesins Myosins and Dyneins as it happens for real systems. The interplay between different means of transport jointly with the asymmetric network topology can give a mechanical insight into the dynamics of the system and possibly provide a reliable mechanism that can be compared to the experimental data.

In our analysis we have considered geometrical constraints as the origin of inhomogeneities in the host fluid motors move in. However, fluids properties might be local due to the presence of suspended particles or density gradients. By capturing such variations as a position-dependent diffusion coefficient we can extend our results to the case of intrinsically inhomogeneous media. Moreover, in this regime we can analyze larger deviations since we do not need to rely on the Fick-Jacobs approximation.

Up to now we have considered the channel shape as fixed. However, channel shape can vary in time either passively, due to fluctuations in the cell membrane, or actively due to the trade-milling of actin filaments. Recent studies have characterized the translocation of finite length polymers across flickering pores [22] showing non trivial dynamical regimes according to the matching of the time and length scales of the pore and the polymer. A similar situation arises for particles transported by cilia inside a channel. The metachronal waves of cilia will induce a net fluid flow inside the channel. This transport mechanism will compete with the entropic one if the channel size is comparable to the length of cilia. In fact if the length of the cilia is comparable to the channel with, their motion will affect the free space available for particle sin suspension inside the channel. When cilia beat together they generate a traveling wave, known as metachronal wave, that will act as a time dependent geometrical confinement for suspended particles. More-

5. CONCLUSIONS AND PERSPECTIVES

over, the traveling nature of the metachronal wave brakes the symmetry along the longitudinal axis inducing an additional, entropy-driven, means of transport that will compete with convection. Since the entropy-driven transport is sensitive to particle size we expect an enhanced particle separation according to their linear dimension.

6. Resumen en castellano

6.1 Introducción

Los seres vivos se caracterizan por su estado de fuera de equilibrio. Gracias a este estado los seres vivos pueden generar fuerzas locales y trabajos mecánicos que les permiten de desplazarse de manera activa así como modelar y mover sus estructuras internas. En este marco se sitúa el transporte intracelular, es decir el conjunto de fenómenos de transporte activo que ocurren en las células. Este transporte se realiza a través de unas proteínas motrices, llamadas motores moleculares. Mientras estén ligados a filamentos como actina o microtubulos, los motores moleculares pueden generar trabajo mecánico gracias a la hidroliza-cion de la ATP, que es la sorgente de energía mas común en la células. Los filamentos de actina y los microtubulos sobre los cuales se desplazan los motores moleculares tienen una estructura periódica y una polaridad local que guía a los motores, una vez enganchados al filamento, a moverse siempre e la misma di-rección. Aunque un motor molecular, una vez enganchado al filamento, puede generar trabajo mecánico por si solo, en general los motores moleculares actúan de manera colectiva. Por esta razón, la propiedades de transporte de conjuntos de motores moleculares han sido estudiadas desde distintas perspectivas. por ejemplo ha sido mostrado que conjunto de motores que se desplazan a lo largo de un filamento pueden obstaculizarse y generar "jamming"o parejas de motores rígidamente acoplados a través de un filamento de ADN se desplazan por longi-tudes mayores reduciendo su probabilidad de desengancharse desde el filamento

Hasta ahora el papel jugado por el entorno en que los motores se desplazan

no ha sido estudiado de manera sistemática. Debidamente a sus reducidas dimensiones, $a =\simeq nm$, velocidad, $v_0 \simeq \mu m/sec$ y a la presencia de partículas en suspensión que incrementan la viscosidad del citoplasma, $\eta \simeq 0.1 Pa \cdot sec$, los motores moleculares se mueven en el régimen de bajos números de Reynolds donde las interacciones hidrodinámicas generadas por el flujo desplazado por los motores pueden general interacciones de largo alcance entre los motores. De otro lado, se ha mostrado que el transporte de partículas, incluso pasivas, queda afectado si las propiedades locales del fluido en que se mueven varían en el espacio. Esta heterogeneidad genera una modulación en los coeficientes de transporte que los motores experimentan a lo lago del filamento y posiblemente afectan a la dinámica del motor.

6.2 Acoplamiento hidrodinámico entre motores moleculares

Cuando un conjunto de motores se desplaza a lo largo de un filamento, el flujo de citoplasma generado por el movimiento de los motores puede generar un acoplamiento entre los motores. En particular se ha observado en células de plantas que el movimiento de los motores puede generar flujos de citoplasma del orden de $\simeq 100\mu m/sec$, es decir dos ordenes de magnitud mas rápido que la velocidad típica de los motores, $\simeq 1\mu m/sec$. Los mecanismos subyacentes a este flujo tan rápido quedan debatidos. Posiblemente, el acoplamiento entre motores proporcionad por el citoplasma podría ser la causa de un flujo tan rápido. Para investigar la factibilidad de esta hipótesis hemos estudiado, a través de simulaciones numéricas, el movimiento de un conjunto de motores que se desplazan a lo largo de un filamento. Para realizar este estudio hemos modelizado los motores moleculares a través de un modelo a dos estados. Según este modelo, cuando los motores se encuentran enganchado al filamento se mueven según un potencial periódico y asimétrico. Cuando los motores alcanzan el mínimo del potencial saltan a un estado levemente ligado en le que pueden difundir a lo largo del filamento pero no pueden alejarse de el en la dirección radial. Con un ritmo constante

los motores vuelven a engancharse. Esta selección de los ritmos de salto rompe el balance detallado y, gracias a la asimetría del potencial, genera una corriente neta de motores.

Para estudiar las interacciones hidrodinámicas se precisa incorporar en el modelo numérico el flujo generado por el desplazamiento de los motores. Siendo que los motores se desplazan cerca de la superficie del filamento es importante incorporar en el modelo como la presencia de la pared del filamento, que impone una velocidad nula al fluido en contacto, afecta a la propagación del campo de velocidad generado por los motores. Entonces hemos utilizado un modelo de fluid a grana gruesa que de un lado nos permite capturar el papel jugado por la pared del filamento y de otro lado nos permite estudiar le sistema sobre escalas de tiempo lo bastante grandes para caracterizar el transporte colectivo. En particular hemos aprovechado del termostato de Lowen-Andersen que permite estudiar un fluido a temperatura constante (es decir en contacto con un baño térmico) en el que las interacciones locales conservan el momento. Para acoplar este fluido a grana gruesa con partículas solidas como los motores moleculares o los filamentos hemos extendido el protocolo de interacción propio del termostato de Lowe-Andersen al caso en que las partículas de fluido interactúan con partículas rígidas, de tal manera que la interacción solido-fluido conserve localmente el momento y que las partículas solidas se encuentren al equilibrio térmico también.

Antes de estudiar como el acoplamiento hidrodinámico entre los motores afecta su velocidad necesitamos entender previamente como los efectos estericos afectan a la dinámica. Este estudio nos permitirá reconocer las contribuciones de los efectos estericos y identificar las contribuciones propiamente hidrodinámicas. Para estudiar el papel de los efectos estericos, hemos solucionado las N ecuaciones de Langevin acopladas que caracterizan el desplazamiento de N motores que interactúan solamente por efectos estéricos en ausencia de interacciones hidrodinámicas. Este estudio ha mostrado que, cuando el tamaño de los motores no es conmensurable al periodo del potencial, la velocidad de un conjunto de motores depende de su densidad. Al revés, cuando el tamaño de los motores es un múltiplo entero de la periodicidad del potencial, la velocidad de un conjunto de motores que interactúan por efectos estéricos queda independiente de la densidad hasta valores muy próximos al máximo por los que la velocidad decrece. Este ultimo

caso resulta bastante útil para la caracterización del acoplamiento hidrodinámico entre los motores. A la hora de estudia las interaccione hidrodinámicas, siendo que los efectos estéricos no afecta a la velocidad de los motores, cualquier dependencia de la velocidad de los motores en la densidad de motores mismos será debida al acoplamiento entre los motores proporcionado por le fluido y no a un solapamiento entre la contribución del efecto estéricos la de la hidrodinámica.

Hemos estudiado el acoplamiento hidrodinámico entre motores moleculares, en distintas geometrías. Hemos observado que el acoplamiento hidrodinámico induce un aumento considerable en la velocidad media de los motores con respecto a la velocidad de un motor singlo. En particular hemos observado que la dinámica a saltos de los motores lleva a incrementos de velocidad mas relevantes, si comparado a los que se obtienen en el caso de partículas propulsadas por fuerzas constantes. La razón de esta diferencia queda en la dinámica a saltos de los motores: cunado los motores están levemente ligados al filamento pueden ser empujado por el flujo de fluido generado por los demás motores, reduciendo de manera relevante el tiempo de espera entre dos saltos. Esta dinámica es ausente en el caso de partículas propulsadas por fuerzas constantes las cuales benefician solamente de la reducción de fricción debida al flujo de fluido. En particular hemos observado que el desplazamiento de los motores genera un flujo de fluido que puede alcanzar velocidades comparables a las de los motores mismos, y que este flujo se mantiene incluso en el caso en que el fluido quede confinado por paredes cilíndricas que imponen una condición de velocidad nula en sus superficies. El flujo generado por los motores moleculares puede ser utilizado para trasportar partículas en suspensión. Hemos observado que la presencia de partículas en suspensión afecta, ligeramente, la dinámica de los motores mientras que, afectando la viscosidad efectiva del fluid, altera de manera mas significativa el perfil de velocidad del fluido, incrementando el caudal.

6.3 Transporte bidireccional

En este capitulo nos enfocamos en la caracterización del movimiento bidireccional observado en el caso de cargas arrastradas por parte de motores que se desplazan

en direcciones opuestas. En este marco las interacciones hidrodinámicas entre los motores moleculares pueden tener una doble naturaleza. De un lado los motores interactúan a través del flujo de fluido que generan al desplazarse. De otro lado, si la carga es una vesícula o mas bien esta cubierta de una membrana bilipidica, esta actúa como una capa fina de liquido. Entonces, en estos casos, el desplazamiento de los motores induce un flujo no solamente en el citoplasma sino también en la membrana que recubre la carga o que compone la vesícula sobre la cual actúa la fuerza generada por los motores.

Estudios anteriores han mostrado que un conjunto de motores moleculares que se displazan en direcciones opuestas puede romper la simetría y generar corrientes cunado están rígidamente acoplados. En particular, cuando la constante de acoplamiento entre los motores excede una cantidad umbral, el acoplamiento entre los motores lleva a una rotura espontánea de la simetría que proporciona a la carga una velocidad neta.

Para caracterizar esta dinámica en el caso en que los motores están acoplados a través de interacciones hidrodinámicas hemos utilizado un aproche mas analítico que nos permite entender la origen física de las dinámicas subyacentes. Asumiendo que la dinámica de los motores que están lejos de las fronteras no tenga una dependencia fuerte en la dinámica de los motores que se encuentran a los extremos de la carga, podemos limitarnos a estudiar un singlo periodo del potencial de interacción entre los motores y el filamento. En este marco la dinámica de los motores queda determinada solamente por sus posiciones relativas al potencial. De esta manera podemos definir una densidad de motores cuya dinámica queda gobernada por una ecuación de Smoluchowski. En particular hemos estudiado dos distintas configuraciones. En la primera imponemos que la densidad local de motores sea constante. Este vinculo de un lado nos permite un tratamiento analitico mas ágil, de otro lado de comparar nuestros resultados con los de motores rígidamente acoplados. En un segundo momento hemos relajado el vinculo sobre la densidad y hemos permitido que la densidad local de motores se ajustara debidamente a la dinámica de los motores mismos.

En el caso de densidad constante de motores hemos caracterizado la ruptura de la simetría y la insurgencia de un movimiento neto debidamente a interaccione hidrodinámicas. En particular hemos observado que las interacciones

hidrodinámicas generan una ruptura de la simetría que lleva el sistema a desplazarse con una velocidad neta. En particular hemos observado que el tamaño de la carga es relevante en la ruptura de la simetría. Comparando nuestros resultados con los recién publicados podemos caracterizar la distinta origen física de la ruptura de la simetría. En particular hemos observado que, en el caso de interacciones hidrodinámicas se puede identificar unos ritmos de saltos entre los dos estados por los cuales se consigue minimizar el tamaño mínimo de la carga necesario para la ruptura de la simetría.

Cuando la densidad puede ajustarse según la dinámica de los motores nuevos regímenes dinámicos aparecen. En este marco el caso de motores rígidamente acoplados no había sido estudiado previamente así que, para mejor entender el papel de las interacciones hidrodinámicas, hemos previamente estudiado el caso de motores rígidamente acoplados. Debidamente al fuerte acoplamiento que lleva todos los motores a moverse en la misma dirección, los perfiles de densidad no evolucionan en el tiempo y quedan congelados como un "quenched disorder". Entonces la amplitud de las modulaciones en la densidad es una constante del moto y determina la naturaleza de la dinámica. Por pequeñas modulaciones en la densidad observamos un comportamiento parecido al que hemos observado en el caso de densidad constante. Cuando las desviaciones son mas relevantes observamos que en lugar de una ruptura de la simetría que lleva a una velocidad neta, observamos que la velocidad del sistema oscilla la rededor de un valor nulo. Este diferente comportamiento desaparece por cargas mas largas.

En el caso de interaccione hidrodinámicas las modulaciones en el perfil de densidad pueden ajustarse según la dinámica y no hay un fenómeno de "quenched disorder". Este diferencia conlleva diferencias mas profundas a la hora de estudiar la dinámica del sistema. En particular cuando los motores están hidrodinámicamente acoplados observamos distintos regímenes a segunda del tamaño de la carga. Por carga de longitud por debajo de una longitud umbral el único estado estacionario estable el que el sistema no se mueve. Cuando el tamaño de la carga es mayor del valor umbral, la velocidad del sistema oscilla al rededor de un valor medio no nulo. Incrementando el tamaño de la carga observamos un segundo umbral pasado el cual el sistema se vuelve biestable, es decir que la velocidad invierte su signo y el sistema se desplaza en las dos direcciones. Este régimen es muy

parecido al que ha sido observado experimentalmente.

6.4   Rectification inducida por el confinamiento

En el citoplasma hay muchas moléculas, proteínas vesículas y orgánulos en suspensión. La presencia de estas partículas afecta al desplazamiento del los motores moleculares. En particular puede afectar localmente a la viscosidad efectivas del citoplasma así como a escala mas grande, la presencia de vesículas o orgánulos puede obstaculizar o hasta impedir el desplazamiento de los motores. En este capitulo nos enfocamos en la caracterización de la dinámica de motores moleculares en le caso en que se desplazan en un canal cuya amplitud varia de manera periódica. Este sistema es una representación simplificada de un medio poroso.

Cuando la amplitud del canal en que se desplazan los motores varia de manera suave es posible aproximar la dinámica del motor a una dinámica monodimensional en la que la variación de amplitud del canal entra como un potencial entropico. Esta aproximación, conocida como aproximación de Fick-Jacobs, ha sido largamente explotada en el estudio de la dinámicas de partículas bajo confinamiento. Como en los casos anteriores modelizamos lo motores a través del modelo a dos estados. Para entender la dependencia de nuestro resultados en el modelo elegido, hemos estudiado otro modelo de motor molecular en el que el motor molecular se modela como una partícula que se mueve en un potencial periódico, igual al que usamos para el caso ligado del modelo a dos estados, y donde la amplitud de las fluctuaciones depende de la posición (ruido multiplicativo).

Hemos estudiado ambos modelos para el motor molecular en le caso en que la amplitud del canal varíe de manera periódica con periodicidad igual a la del potencial. La dinámica del sistema, por ambos modelos, varia sensiblemente a segunda que tanto el canal como el potencial sean simétrico o asimétricos. En el caso de potencial y canal ambos simétrico no hay ruptura de la simetría por parte de ninguno de los dos por separado. Todavía, si el canal y el potencial no están en fase, interacción entre el confinamiento proporcionado por el canal y el potencial generan un potencial efectivo no simétrico que da lugar a velocidades

netas que rompen la simetría. En el caso del modelo a dos estados, la presencia de distintas longitudes y tiempos característicos intrínsecos en el modelo genera una dinámica mas rica en la que el signo de la velocidad puede variar a segunda de la processividad de los motores. En particular, siendo que no hay una ruptura intrínseca de la simetría, al variar el desfase encontramos un perfil de velocidad que es también simétrico, es decir que la velocidad media integrada sobre el desfase es nula. En el caso en que la amplitud del canal varíe de manera no simétrica, el sistema adquiere una ruptura global de la simetría y, aunque la variar el desfase entre el potencial y el canal el signo de la velocidad varia, en promedio lo motores tienen una dirección preferente.

Cuando el potencial no es simétrico los motores tienen una velocidad no nula incluso por un canal llano. Igualmente la amplitud variable del canal afecta de manera significativa la dinámica de los motores y puede amplificar así como invertir la velocidad neta de los motores. En particular hemos observado que el signo de la velocidad de los motores depende del tamaño de la carga arrastrada así que, en principio, se puede explotar este mecanismo para separar partículas. Cuando ambos el canal y el potencial son asimétricos la dinámica se hace mas rica y todos los regímenes que hemos encontrado en los anteriores caso se pueden reproducir.

6.5 Conclusiones

El objetivo de esta tesis ha sido la caracterizacin de la interaccin entre la dinmica interna de los motores moleculares y el entorno en que los motores se mueven. En particular, hemos caracterizado dos escenarios diferentes para los cuales las propiedades locales del fluido afectan significativamente a la dinmica general de los motores.

En un primer caso hemos estudiado la dinamica de varios motores moleculares que se deplazan a lo largo de un filamento comn. Mientras se desplazan, los motores moleculares generan flujos citoplasmticos locales que afectan el estado local del fluido. Por lo tanto la dinmica interna de los motores moleculares se ve afectada por el acoplamiento hidrodinmico entre los motores. Hemos caracterizado el

acoplamiento hidrodinmico entre motore moleculares en dos escenarios diferentes. Por un lado hemos encontrado que el acoplamiento hidrodinmico entre motores proporcionadas por el citoplasma puede afectar fuertemente a la velocidad global de los motores. Las variaciones locales en la densidad de motores pueden crecer y llevar a la formacin de clusters que aceleran la velocidad de los motores y que conducen a la aparicin de estructuras estables. Por otro lado, cuando varios motores estn empujando una carga comn, la naturaleza fluida de la membrana que envolve la carga proporciona un acoplamiento hidrodinamico adicional entre los motores. En este escenario, hemos observado que el acoplamiento hidrodinmico entre los motores que tiran en direcciones opuestas, puede conducir a la ruptura de la simetra as como a biestabilidad incluso para tamaos de sistemas comparables con situaciones biolgicas relevantes. Por lo tanto, las interacciones hidrodiamicas repesentan una alternativa para el control de la dinmica de la carga.

Como segundo caso hemos estudiado la dinmica de un motor molecular singlo en movimiento en un fluido intrnsecamente inhomogneo en el cual, la inhomogeneidad del lquido se induce por la presencia de confinamientos geomtricos. Si el espacio local disponible varia, surgen fuerzas adicionales de la naturaleza entrpica. La interaccin entre el movimiento a saltos del motor y la modulacin en el confinamiento puede conducir a nuevos rgimenes dinmicos, distintos de los que ocurren en el caso de partculas bajo fuerzas constantes o motores moleculares desplazando en un entorno homogneo.

Este estudio seala dos resultados principales. Por una parte la trayectoria a saltos de los motores moleculares los hace particularmente adecuados para la formacion de comportamientos colectivos. La presencia de diferentes longitudes y escalas de tiempo en la dinamica intrinseca de los motores moleculares da lugar a nuevos comportamientos colectivos ausente por partculas arrastradas por fuerzas constantes.

De otro lado, hemos mostrado que, cuando el entorno en que se desplazan los motores es intrnsecamente inhomogneo, como es para motores desplazando bajo restricciones geomtricas, o anisotropo, la dinmica general de los motores se desva considerablemente de la de un singlo motor en medio homogneo. Por lo tanto, la dinamica de los motores en situaciones in vivo puede ser fuertemente afectada por las condiciones del citoplasma en que se desplazan.

6. RESUMEN EN CASTELLANO

References

[1] Y. Aghababaie, G. I. Menon, and M. Plischke. *Phys. Rev. E*, **59**:2578, 1999. 63, 70

[2] M. Y. Ali, G. G. Kennedy, D. Safer, K. M. Trybus, H. L. Sweeney, and D. M. Warshaw. *Proc. Natl. Acad. Sci U S A*, **108**[34], 2011. 31, 53, 70

[3] E. Altintas, E. Sarajlic, F. K. Bohringerb, and H. Fujita. Numerical and experimental characterization of 3-phase rectification of nanobead dielectrophoretic transport exploiting brownian motion. *Sensors and Actuators A*, **154**:123–131, 2009. 73

[4] A. Amir, J. Paulose, and D. R. Nelson. Theory of interacting dislocations on cylinders. *Phys. Rev. E*, **87**:042314, Apr 2013. 105

[5] V. Ananthanarayanan, M. Schattat, S. K. Vogel, A. Krull, and N. Pavin. Dynein motion switches from diffusive to directed upon cortical anchoring. *Cell*, **153**:1526, 2013. 30, 100, 101

[6] R. D. Astumian. Thermodynamics and Kinetics of a Brownian Motor. *Science*, **917**[1997], 2010. 74

[7] J.-y. Awata, T. Kashiyama, K. Ito, and K. Yamamoto. Some Motile Properties of Fast Characean Myosin. **2836**[02]:659, 2003. 100

[8] M. Badual, J. Jülicher, and J. Prost. Bidirectional cooperative motion of molecular motors . *Proc. Natl. Acad. Sci U S A*, **99**:6696, 2002. 2, 5

REFERENCES

[9] R. M. Barrer. *Zeolites and Clay Minerals as Sorbents and Molecular Sieves.* Academic, New York, 1978. 73

[10] P. Bartlett, A. Banker, and S. Easton. AN ELECTRON AXONS AND CULTURE I . Cells Which MICROSCOPIC DENDRITES Develop STUDY OF THE DEVELOPMENT NEURONS Intercellular Contacts OF Without. *Journal of Neuroscience*, **4**:1944, 1984. 106

[11] M. J. Bloemink and M. A. Geeves. Seminars in Cell & Developmental Biology Shaking the myosin family tree : Biochemical kinetics defines four types of myosin motor. *Seminars in Cell and Developmental Biology*, **22**[9]:961, 2011. 30

[12] J. Brugues and J. Casademunt. Self-Organization and Cooperativity of Weakly Coupled Molecular Motors under Unequal Loading. *Phys. Rev. Lett.*, **102**:118104, 2009. 13, 104

[13] P. S. Burada, Y. Lib, W. Rieflerb, and G. Schmid. Entropic transport in energetic potentials. *Chem. Phys.*, **375**:514, 2010. 73

[14] P. S. Burada, G. Schmid, D. Reguera, J. M. Rubi, and P. Hänggi. Biased diffusion in confined media: Test of the fick-jacobs approximation and validity criteria. *Phys. Rev. E*, **75**:051111, 2007. 76

[15] M. Büttiker. Transport as a consequence of state-dependent diffusion. *Z. Phys. B*, **68**:161, 1987. 80, 81

[16] C. Calero, J. Faraudo, and M. Aguilella-Arzo. First-passage-time analysis of atomic-resolution simulations of the ionic transport in a bacterial porin. *Phys. Rev. E*, **83**:021908, 2011. 73

[17] O. Campas, C. Leduc, P. Bassereau, J. Casademunt, J.-F. Joanny, and J. Prost. Coordination of kinesin motors pulling on fluid membranes. *Biophysical J.*, **94**:5009, 2008. 2, 5, 68, 104

[18] O. Campas, K. B. Zeldovich, P. Jolimaitre, L. Bourel-Bonnet, P. Bassereau, J. Prost, and B. Goud. Cooperative extraction of

membrane nanotubes by molecular motors. *Proc. Natl. Acad. Sci. USA*, **101**:17096, 2004. 104

[19] Y. Chebli, J. Kroeger, and A. Geitmann. Transport Logistics in Pollen Tubes. *Molecular Plant*, **6**[4]:1037, 2013. 23

[20] T. Chou, K. Mallick, and R. K. P. Zia. Non-equilibrium statistical mechanics: from a paradigmatic model to biological transport. *Rep. Prog. Phys.* 13

[21] P. Cicuta, S. L. Keller, and S. L. Veatch. *J. Phys. Chem. B*, **111**:3328, 2007. 68

[22] J. A. Cohen, A. Chaudhuri, and R. Golestanian. Active Polymer Translocation through Flickering Pores. *Phys. Rev. Lett.*, **107**[December]:238102, 2011. 107

[23] L. Conway, D. Wood, E. Tüzel, and J. L. Ross. Motor transport of self-assembled cargos in crowded environments. *Proc. Natl. Acad. Sci U S A*, **109**[51]:1–6, 2012. 2, 7

[24] J. R. Cooper and L. Wordeman. The diffusive interaction of microtubule binding proteins. *Curr. Opin. Cell Biol.*, **21**:68, 2009. 29, 30, 102

[25] L. Dagdug, A. M. Berezhkovskii, Y. A. Makhnovskii, V. Y. Zitsereman, and S. Bezrukov. *J. Chem. Phys.*, **134**:101102, 2011. 73

[26] R. Di Leonardo, S. Keen, F. Ianni, J. Leach, M. J. Padgett, and G. Ruocco. *Phys. rev. E*, **78**:031406, 2008. 67

[27] R. J. Ellis. Macromolecular crowding: obvious but underappreciated. *TRENDS in Biochem. Sci.*, **26**:597, 2001. 5, 8

[28] S. A. Endow and H. Higuchi. *Nature*, **406**:913, 2000. 32

[29] P. Fayant, O. Girlanda, Y. Chebli, C.-. Aubin, I. Villemure, and A. Geitmann. Finite element model of polar growth in pollen tubes. *The PLant Cell*, **22**:2579, 2010. 23

REFERENCES

[30] R. P. Feynman. *The Feynman Lectures on Physics, Vol. 1.* Addison-Wesley, Boston, 1963. 74

[31] M.-m. Fu and E. L. F. Holzbaur. JIP1 regulates the directionality of APP axonal transport by coordinating kinesin and dynein motors. *Cell*, **202**[3]:495–508, 2013. 31

[32] Y. E. Goldman and E. L. F. Holzbaur. *Current Opinion in Cell Biology*, **22**:4, 2010. 2, 7, 31

[33] L. S. B. Goldstein. Kinesin molecular motors : Transport pathways , receptors , and human disease. *Proc. Natl. Acad. Sci U S A*, **98**[13]:6999, 2001. 101

[34] L. S. B. Goldstein. Do Disorders of Movement Cause Movement Disorders and Dementia ? *Neuron*, **40**[40]:415, 2003. 101

[35] R. E. Goldstein, I. Tuval, V. D. Meent, and J. W. Microfluidics of cytoplasmic streaming and its implications for intracellular transport. *Proc. Natl. Acad. Sci. USA*, **105**:3663–3667, 2008. 30

[36] P. Greulich, A. Garai, K. Nishinari, A. Schadschneider, and D. Chowdhury. Intracellular transport by single-headed kinesin KIF1A : Effects of single-motor mechanochemistry and steric interactions. *Phys. Rev. E*, pages 1–15, 2007. 30

[37] A. Grimm and H. Stark. Hydrodynamic interactions enhance the performance of brownian ratchets. *Soft Matter*, **7**:3219, 2011. 13

[38] T. Guérin, J. Prost, and J.-F. Joanny. *Phys. Rev. Lett.*, **106**:068101, 2011. 5, 31, 44, 48, 51, 53, 66

[39] T. Guérin, J. Prost, and J.-F. Joanny. *Phys. Rev. E*, **87**:032601, 2011. 35

[40] T. Guérin, J. Prost, P. Martin, and J.-F. Joanny. Coordination and collective properties of molecular motors : theory. *Curr. Op. Cell Biol.*, **22**:14–20, 2010. 2, 7, 31, 65

[41] P. HÄNGGI AND F. MARCHESONI. Artificial Brownian motors : Controlling transport on the nanoscale. *Rev. Mod. Phys.*, **81**[March]:387–442, 2009. 74

[42] J. HELENIUS, G. BROUHARD, Y. KALAIDZIDIS, S. DIEZ, AND J. HOWARD. The depolymerizing kinesin MCAK uses lattice diffusion to rapidly target microtubule ends. *Nature*, **441**[May]:115–119, 2006. 29, 102

[43] N. HIROKAWA AND R. TAKEMURA. Biochemical and molecular characterization of diseases linked to motor proteins. *Trends in biochemical sciences*, **28**[10]:558, 2003. 101

[44] D. HOUTMAN, I. PAGONABARRAGA, C. P. LOWE, A. M. C. EMONS, AND E. EISER. Hydrodynamic flow caused by active transport along cytoskeletal elements. *EPL*, **78**[April]:10, 2007. 5, 13

[45] J. HOWARD. Molecular motors: structural adaptations to cellular functions. *Nature*, **389**:561, 1997. 29

[46] J. HOWARD. *Mechanics of Motor Proteins and the Cytoskeleton*. Sinauer, Sunderland, 2001. 2, 3, 7, 30

[47] M. IWAKI, H. TANAKA, H. IWANE, E. KATAYAMA, AND M. IKEBE. Cargo-Binding Makes a Wild-Type Single-Headed Myosin-VI Move Processively. *Biophysical Journal*, **90**[10]:3643, 2006. 30, 100, 101

[48] H. JACOBS, M. *Diffusion Processes*. Springer-Verlag, New York, 1967. 73, 75

[49] A. JANNASCH, V. BORMUTH, M. STORCH, J. HOWARD, AND E. SCHA. Kinesin-8 Is a Low-Force Motor Protein with a Weakly Bound Slip State. *Biophysical Journal*, **104**[June]:2456, 2013. 30, 100, 101

[50] F. JULICHER, A. AJDARI, AND J. PROST. *Rev. Mod. Phys.*, **69**:1269, 1997. 4, 8, 9, 10, 31, 32, 53

[51] F. JÜLICHER, A. AJDARI, AND J. PROST. Modeling molecular motors. *Rev. Mod. Phys.*, **69**:1269, 1997. 79, 80

REFERENCES

[52] L. C. KAPITEIN, B. H. KWOK, J. S. WEINGER, C. F. SCHMIDT, T. M. KAPOOR, AND E. J. G. PETERMAN. Microtubule cross-linking triggers the directional motility of kinesin-5. *Cell*, **182**[3]:421, 2008. 30, 100, 101

[53] D. R. KLOPFENSTEIN, M. TOMISHIGE, N. STUURMAN, R. D. VALE, AND S. FRANCISCO. Role of Phosphatidylinositol(4,5) bisphosphate Organization in Membrane Transport by the Unc104 Kinesin Motor. *Transport*, **109**:347, 2002. 30

[54] S. KLUMPP AND R. LIPOWSKY. Cooperative cargo transport by several molecular motors. *Proc. Natl. Acc. Sci. U S A*, **102**:17284, 2005. 31

[55] A. KUNWAR, S. K. TRIPATHY, J. XU, M. K. MATTSON, P. ANAND, AND R. SIGUA. *Proc. Natl. Acad. Sci U S A*, **108**:18960, 2011. 31

[56] C. KURAL, H. KIM, S. SYED, G. GOSHIMA, V. I. GELFAND, AND P. R. SELVIN. *Science*, **308**:1469, 2005. 31, 53, 70

[57] C. LEDUC, K. PADBERG-GEHLE, V. VARGA, D. HELBING, S. DIEZ, AND J. HOWARD. Molecular crowding creates traffic jams of kinesin motors on microtubules. *Proc. Natl. Acad. Sci U S A*, **109**:6100, 2012. 2, 7

[58] C. LEDUC, F. RUHNOW, J. HOWARD, AND S. DIEZ. Detection of fractional steps in cargo movement by the collective operation of kinesin-1 motors. *Proc. Natl. Acad. Sci U S A*, **104**[26]:10847, 2007. 4, 7, 31, 100

[59] S.-H. LEE, K. LADAVAC, M. POLIN, AND D. GRIER. Observation of flux reversal in a symmetric optical thermal ratchet. *Phys. Rev. Lett.*, **94**:110601, 2005. 78

[60] H. LU, M. Y. ALI, AND K. M. TRYBUS. Diffusive movement of processive kinesin-1 on microtubules. *Traffic*, **10**:1429–1438, 2009. 30, 100, 101

[61] C. LUTZ, M. REICHERT, H. STARK, AND C. BECHINGER. Surmounting barriers : The benefit of hydrodynamic interactions. *Europhysics Letters*, **74**[May]:719–725, 2006. 16

[62] P. Malgaretti, I. Pagonabarraga, and D. Frenkel. *Phys. Rev. Lett.*, **109**:168101, 2012. 63

[63] P. Malgaretti, I. Pagonabarraga, and J. M. Rubi. Cooperative rectification in confined brownian ratchets. *Phys. Rev. E*, **85**:010105(R), 2012. 74

[64] P. Malgaretti, I. Pagonabarraga, and J. M. Rubi. Confined brownian ratchets. *J. Chem. Phys*, **138**:194906, 2013. 74

[65] C. Margraves, K. Kihm, S. Y. Yoon, S. Choi, C. K. Lee, J. Liggett, and S. J. Baek. *Biotechnology and Bioengineering*, **108**:2504, 2011. 68

[66] S. Martens, G. Schmidt, L. Schimansky-Geier, and P. Hänggi. Entropic particle transport: Higher-order corrections to the fick-jacobs diffusion equation. *Phys. Rev. E*, **83**:051135, 2011. 73

[67] K. Matsumoto, S. Takagi, and T. Nakagaki. Locomotive Mechanism of Physarum Plasmodia Based on Spatiotemporal Analysis of Protoplasmic Streaming. *Biophysical Journal*, **94**:2492, 2008. 5

[68] I. Minoura, E. Katayama, K. Sekimoto, and E. Muto. One-Dimensional Brownian Motion of Charged Nanoparticles along Microtubules : A Model System for Weak Binding Interactions. *Biophysj*, **98**[8]:1589, 2010. 29, 102

[69] M. J. I. Müller, S. Klumpp, and R. Lipowsky. Bidirectional transport by molecular motors: Enhanced processivity and response to external forces. *Biophysical Journal*, **98**:2610, 2010. 31

[70] A. Nebenfürer, L. A. Gallagher, T. G. Dunahay, J. A. Frohlick, A. M. Mazurkiewicz, J. B. Meehl, and L. A. Staehelin. *Society*, **121**:1127, 1999. 53, 70

[71] D. R. Nelson and A. Amir. Defects on cylinders: Bacterial cell walls and superfluid helium films. *arXiv*, page arXiv:1303.5896, 2012. 105

REFERENCES

[72] I. Neri, N. Kern, and A. Parmeggiani. Totally asymmetric simple exclusion process on networks. *Phys. Rev. Lett.*, **107**:068702, Aug 2011. 103

[73] I. Neri, N. Kern, and A. Parmeggiani. Modeling cytoskeletal traffic: An interplay between passive diffusion and active transport. *Phys. Rev. Lett.*, **110**:098102, Feb 2013. 103

[74] Y. Okada, H. Higuchi, and N. Hirokawa. Processivity of the single-headed kinesin KIF1A through biased binding to tubulin. *Nature*, **424**[May]:574, 2003. 13, 30, 100, 101

[75] A. Perez-Madrid, J. Rubi, and P. Mazur. Brownian motion in the presence of a temperature gradient. *Physica A*, **212**:231, 1994. 81

[76] M. Pons and P. Bernado. Macromolecular crowding in biological systems : hydrodynamics and NMR methods. *Journal of Molecular Recognition*, [1]:397, 2004. 5

[77] W. H. Press, S. A. Teukolsky, W. T. Vetterling, and B. P. Flannery. *Numerical Recipes, third edition.* Cambridge University Press, Cambridge, 2007. 50, 60

[78] D. Reguera and J. M. Rubi. Kinetic equations for diffusion in the presence of entropic barriers. *Phys. Rev. E*, **64**:061106, 2001. 75, 76

[79] D. Reguera, G. Schmid, P. S. Burada, J. M. Rubi, P. Reimann, and P. Hänggi. Entropic transport: Kinetics, scaling, and control mechanisms. *Phys. Rev. Lett.*, **96**:130603, 2006. 73, 76

[80] P. Reimann. Brownian motors: Noisy transport far from equilibrium. *Phys. Rep.*, **361**:57–265, 2002. 79

[81] P. Reimann and P. Hänggi. Introduction to the physics of brownian motors. *Appl. Phys. A*, **75**:169, 2002. 78

[82] A. R. Rogers, J. W. Driver, P. E. Constantinou, D. Kenneth, and M. R. Diehl. Negative interference dominates collective transport of

kinesin motors in the absence of load. *Phys. Chem. Chem. Phys.*, **11**:4882, 2009. 4, 7, 31, 100

[83] J. M. Rubi and D. Reguera. Thermodynamics and stochastic dynamics of transport in confined media. *Chem. Phys.*, **375**:518, 2010. 73

[84] P. M. Shaklee, T. Idema, G. Koster, C. Storm, T. Schmidt, and M. Dogterom. Bidirectional membrane tube dynamics driven by nonprocessive motors. *Proc. Natl. Acad. Sci. U S A*, **105**:7993, 2007. 105

[85] T. Shimmen. The sliding theory of cytoplasmic streaming : fifty years of progress. *Journal of Plant Research*, **120**:31, 2007. 4, 5

[86] M. Smoluchovski. Experimentell nachweisbare, der ublichen thermodynamik widersprechende molekularphenomene. *Phys. Zeitshur.*, **13**:1069, 1912. 74

[87] S. H. Strogaz. *Nonlinear Dynamics and Chaos*. WestView Press, Colorado, 1994. 63, 65

[88] R. D. Vale, D. R. Soll, and I. R. Gibbons. One-dimensional diffusion of microtubules bound to flagellar dynein. **59**:915, 1989. 30, 100, 101

[89] D. van der Meer and P. Reimann. Temperature anisotropy in a driven granular gas. *Europhys. Lett.*, **74**:384, 2006. 82

[90] N. G. van Kampen. Explicit calculation of a model for diffusion in nonconstant temperature. *J. Math. Phys.*, **29**:1220, 1988. 80

[91] J. Vermant and M. J. Solomon. Flow-induced structure in colloidal suspensions. *J. Phys.: Condens. Matter*, **17**:187, 2005. 102

[92] L. Vidali, G. M. Burkart, R. C. Augustine, E. Kerdavid, E. Tu, and M. Bezanilla. Myosin XI Is Essential for Tip Growth in Physcomitrella patens. *Society*, **22**[June]:1868, 2010. 23

[93] J. F. Wambaugh, C. Reichhardt, C. J. Olson, F. Marchesoni, and F. Nori. Superconducting fluxon pumps and lenses. *Phys. Rev. Lett.*, **83**:5106, 1999. 73

REFERENCES

[94] Z. Wang and M. P. Sheetz. One-dimensional diffusion on microtubules of particles coated with cytoplasmic dynein and immunoglobulins. *Cell structure and function*, **24**:373, 1999. 30, 100, 101

[95] A. D. Wessel, S. Kramer, C. F. Schmidt, C. Thiede, and S. Laka. A Chimeric Kinesin-1 Head / Kinesin-5 Tail Motor Switches between Diffusive and Processive Motility. *Biophysical Journal*, **104**[January]:432, 2013. 4, 30, 100, 101

[96] K. Wolff and D. Marenduzzo. *in preparation.* 102

[97] D. Zimmermann, B. A. Motaal, L. V. V. Voithenberg, and M. Schliwa. Diffusion of Myosin V on Microtubules : A Fine-Tuned Interaction for Which E-Hooks Are Dispensable. *Design*, **6**[9], 2011. 29, 102

[98] L. Zonia and T. Munnik. Uncovering hidden treasures in pollen tube growth mechanics. *Trends in Plant Science*, **14**[May]:318, 2009. 23

[99] R. Zwanzig. Diffusion past an entropy barrier. *J. Phys. Chem.*, **96**:3926, 1992. 73, 75, 80